Image Processing and Computing in Structural Biology

PROEFSCHRIFT

ter verkrijging van

de graad van Doctor aan de Universiteit Leiden,

op gezag van Rector Magnificus prof. mr. P. F. van der Heijden,

volgens besluit van het College voor Promoties,

te verdedigen op donderdag 12 November 2009

klokke 15.00 uur

door

Linhua Jiang

Geboren te Yongzhou, China
in 1977

Promotiecommissie

Promotor:	Prof. dr. J.P. Abrahams
Overige leden:	Prof. dr. H.W. Zandbergen (TUD, Delft)
	Prof. dr. M. van Heel (Imperial College, London)
	Prof. dr. M.H.M. Noteborn
	Prof. dr. N. Ban (ETH, Zurich)
	Dr. F.J. Verbeek
	Dr. J.R. Plaisier (ELETTRA, Trieste)
	Dr. M.E. Kuil
	Dr. R.A.G. de Graaff

Cover: The ribosomal large subunit 50S and cryo-electron microscopy

ISBN: 978-90-8570-293-1

Copyright © by Linhua Jiang 2009
All rights reserved. No part of this publication may be reproduced, stored in a retrieval system, or transmitted in any form or by any means without the prior written permission of the copyright owner.

Printed by Wöhrmann Print Service, The Netherlands.

Contents

Chapter 1 Introduction 5

Chapter 2 Automated carbon masking and particle picking in data preparation of single particles 21

Chapter 3 A novel approximation method of CTF amplitude correction for 3D single particle reconstruction 41

Chapter 4 Reconstruction of the complexes of the ribosomal large subunit 50S with Hsp15 and t-RNA reveals the rescue mechanism of the stalled 50S 67

Chapter 5 Unit-cell determination from randomly oriented electron diffraction patterns 91

Chapter 6 User manual of EDiff: A unit-cell determination and indexing software 109

Chapter 7 Conclusion and Perspectives 139

Summary 141

Samenvatting 144

Curriculum Vitae 146

A Special Word of Thanks 147

Chapter 1 Introduction

1.1 Structural biology, cryo-EM and image processing

Structural biology is a branch of life science which focuses on the structures of biological macromolecules, investigating what the structure looks like and how alterations in the structure affect the biological functions.

This subject is of great interest to biologists because macromolecules carry out most of the cellular functions, which exclusively depend on their specific three-dimensional (3D) structure. This 3D structure (or tertiary structure) of molecules depends on their basic sequence (or primary structure). However, the 3D structure cannot be calculated directly from the sequence. In order to understand the complicated biological processes at the cellular level, it is therefore essential to determine the 3D structure of molecules.

The research of structural biology is intimately relevant to human health. A healthy body requires the coordinated action of billions of indispensable proteins. Each protein has a unique molecular shape that exactly fits its particular function. Determining the 3D structures of key proteins and viruses at the atomic level is an important and often vital strategic step to find the reasons behind many human diseases. This step can help us clarifying the role of the shape of proteins and their complexes (including viruses) in health and disease. Structure determination of viruses is thus a persistent hot topic of research. Figure 1 shows an example of the structure of cytoplasmic polyhedrosis virus (CPV).

Biomolecules, even the so called macromolecules, normally have a tiny size measured in tens of nanometers or less. Such molecules are too small to see with the light microscope. The techniques that can reach atomic resolution mainly include X-ray crystallography, nuclear magnetic resonance (NMR) spectroscopy, and electron cryo-microscopy (cryo-EM). X-ray crystallography has been able to tackle large complexes, but is limited to complexes that can form crystals and NMR is only suitable for smaller macromolecules and complexes. This leaves a large number of

challenging structures that cannot be resolved using the X-ray and NMR techniques. Especially for large complexes that resist crystallogenesis, electron cryo-microscopy (cryo-EM, or cryo-electron microscopy) is a viable alternative. This technique is a combination of transmission electron microscopy (TEM) and cryo-equipment.

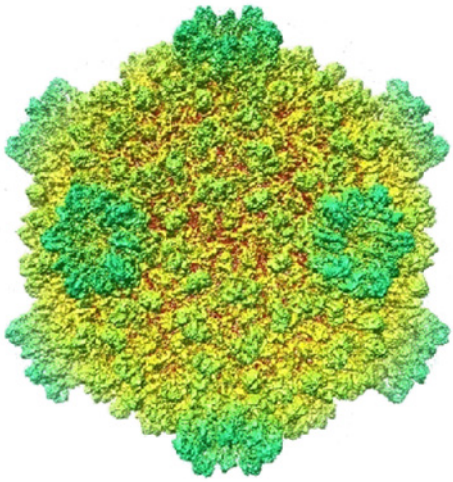

Figure 1. *Structure of cytoplasmic polyhedrosis virus (CPV) with a resolution of 3.88Å, obtained by using cryo-EM single particle reconstruction (EMDataBank id: EMD-1508, Yu et al., 2008), the highest resolution achieved so far by using cryo-EM. CPV belongs to the virus family of Reoviridae. Reoviridae can affect the gastrointestinal system (e.g. Rotavirus) and respiratory tract. Reovirus infects humans often; it is easy to find Reovirus in clinical specimens.*

TEM is suitable for looking into the molecules in atomic detail. The cryo-EM technique provides a way to observe the real "native state" structure as it exists in solution by freezing the samples extremely fast in a layer of vitreous ice. Freezing reduces electron damage, allowing a higher dose of electron exposure to gain better signal-to-noise ratio (SNR) images. Cryo-EM is thus the obvious choice to study large biomolecular complexes. The enormous potential of cryo-EM in biological structure determination has already been realized since the early 1990's (for a review, see R. Henderson, 2004).

Transmission electron microscopy has two modes available: image mode and diffraction mode (Figure 2). The 3D structure of a molecule cannot be obtained directly by TEM, but must be reconstructed using computational methods. In structural biology, two new methods using TEM are still developing: three-dimensional cryo-electron microscopy (3DEM, also known as single particle reconstruction) and electron diffraction (or electron crystallography). 3DEM uses the image mode of TEM, and electron crystallography uses the diffraction mode.

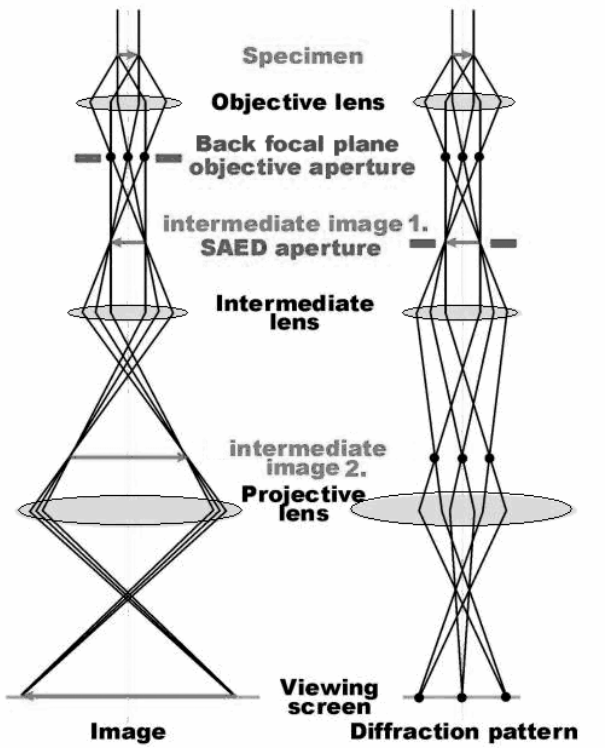

Figure 2. *Image and diffraction modes of transmission electron microscopy (Williams & Carter, 1996). SAED: Selected Area Electron Diffraction. The objective lens forms a diffraction pattern in the back focal plane and generates an image in the image plane (intermediate image 1.). Diffraction pattern and image are both present in TEM. The intermediate lens decides which of them appears in the plane of the second intermediate image (intermediate image 2.) and is projected on the viewing screen. It is easy to switch between image and diffraction modes by adjusting the intermediate lens.*

3DEM requires the reconstruction of a macromolecular 3D model from large amount of noisy 2D projection images (e.g. Figure 3A) of a specimen. Electron crystallography is a method to gain and analyze diffraction patterns (images in Fourier space, e.g. Figure 3B) of crystals (1D, 2D or 3D crystals) for the reconstruction of 3D structure in Fourier space, similar as the technique used in X-ray crystallography. To see the true 3D structure underlying the recorded data, sophisticated image processing and computing are indispensable for either method.

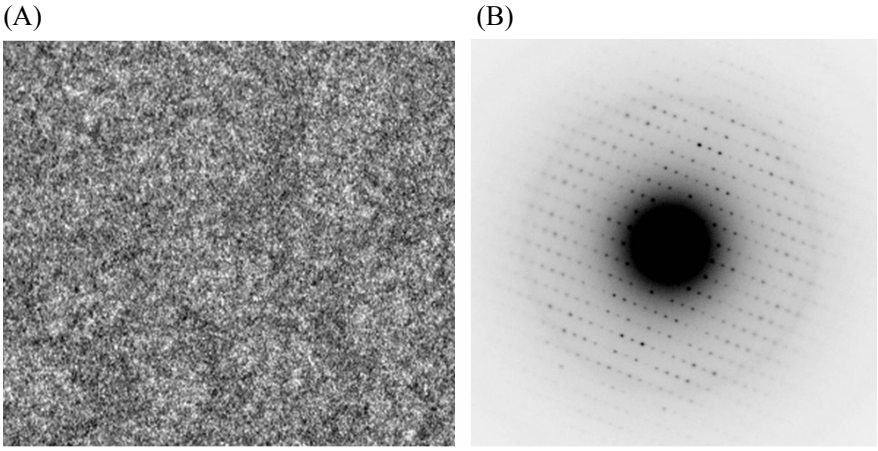

Figure 3. *Examples of a micrograph of single particles (A) and of a electron diffraction pattern of frozen nano-crystal of a protein (lysozyme) (B).*

Image processing and computing methods are essential for solving structures of macromolecules. Both X-ray crystallography and the NMR require the power of computing. Images from electron microscopy (Figure 3) also need image processing to reconstruct the 3D structure. For EM images, computing methods for 3DEM single particle reconstruction is still developing rapidly. They utilize many computer image processing techniques.

In image mode, TEM is affected by the instrumental aberration problem and the image is distorted by the contrast transfer function (CTF). Aberration correction of the CTF is one of the major tasks of image processing in 3DEM. In diffraction mode, diffraction patterns from electron microscopy actually represent a Fourier lattice. Analysing this

data also needs complicated procedures of image processing and computing.

Electron crystallography of 3D crystals is not new in inorganic chemistry and material science, but it is a new in biochemistry. There is no existing way to obtain a 3D structure from the diffraction images of 3D protein crystals (though there are a few successful cases with 2D and 1D crystals). But in theory, a set of random diffraction images from one species of 3D protein crystals may include sufficient information to reconstruct their atomic structure. No matter which methods are to be used, complicated image processing procedures and time consuming computing are indispensable to calculate a 3D structure from the EM micrographs.

This thesis mainly focuses on the image processing techniques of 3DEM and electron crystallography, and solves biological problems based on the 3D structures I determined.

1.2 Nano-techniques in structural biology, X-ray, NMR, electron diffraction and 3DEM

X-ray diffraction, NMR spectroscopy, and 2D/1D electron crystallography involve measurements of vast numbers of identical molecules at the same time. Most of the solved atomic structures use micro-crystals and X-ray diffraction. In a crystal, all molecules are in the same conformation and binding state. Their uniform orientation and ordered arrangement enable the X-ray diffraction.

The wavelength of the electron beam generated in a TEM is much shorter than that of the radiation which is usually used in X-ray crystallography. E.g. for 300KeV TEM, the wavelength is ~0.019Å; for 200KeV, ~0.025Å. X-rays used for atomic structure determination have wavelengths between 2 Å and 0.5 Å. Theoretically, electrons diffraction therefore has a higher resolution limit than X-ray diffraction.

But electron diffraction suffers from the dynamic diffraction problem, caused by the strong interactions between electrons and the matter. Only single layer crystals (2D

crystal) or helical arrays (1D crystals) have been investigated successfully with electron diffraction. In this thesis, nano-crystals (3D protein crystals with nano-scale size) and the new technique of precession of the electron beam were used to reduce dynamic scatter to acquire the electron diffraction patterns (e.g. Figure 3B).

In the current practice in electron diffraction a single nano-crystal must be selected in image TEM mode and then the microscope must be switched to diffraction mode. This is not possible in X-ray diffraction, limiting this technique to the study of the micro-crystals or powders of nanocrystals. Another apparent advantage of using nano-crystals is: it is much easier to grow nano-crystals than to obtain micro-crystals with micrometer-scale size (Georgieva et al., 2007).

In high-resolution 3D EM single particle reconstruction, crystals are not necessary. Particles embedded in vitreous ice can have random orientations and arrangements. Very small amounts of sample are required for a 3D reconstruction, compared to the amount required for growing a crystal. Besides, in 3DEM, structural homogeneity or integrity is more important than purity, as opposed to X-ray crystallography and NMR, in which sample purity is essential (Zhou, 2008).

Generally speaking, both different experimental and computational methods have their advantages and disadvantages:

Advantages of X-ray crystallography method:

- Well-established techniques and software
- Highest atomic resolution structure achieved

Disadvantages of X-ray crystallography method:

- Difficult to grow crystals
- Single conformation or binding state, as a result of the crystal constraints
- Difficult to solve in presence of disorder

Advantages of 3DEM:

- No need to crystallize
- No phase problem

- Small amount of materials needed
- Easy for large molecules, up to 2000 Å
- All "native" functional states in solution can be captured in principle

Disadvantages of 3DEM:

- large computational cost
- limited resolution, highest resolution thus far ~4 Å (Yu et al., 2008)
- less developed for different conformational states

Advantages of electron diffraction:

- Can handle nano-size crystals
- Growing nano-crystals is relative easier
- Small amount of materials needed
- Strong diffraction with matter at an atomic resolution
- Share lots of common knowledge with well-developed X-ray diffraction techniques

Disadvantages of electron diffraction:

- Dynamic scattering
- Electron beam damage
- Manual data acquisition is less automated

Other technologies such as powder diffraction and tomography are also relevant for structure determination, but only have limited applications due to the low resolution that can be achieved.

1.3 Basics of 3DEM single particle reconstruction

3DEM single particle reconstruction is the reconstruction of a macromolecular 3D structure from a set of cryo-EM projection images. In a micrograph (e.g. Figure 3A), the molecules exist in the form of single isolated particles, randomly distributing in a layer of vitreous ice. Thousands to hundreds of thousands of noisy images of individual molecules are needed to calculate the 3D structure.

Biomolecules are highly susceptible to radiation damage when exposed to the electron beam. In order to decrease the damage, images are obtained with a low dose of exposure and by using electron cryo-microscopy. Nevertheless, the technique results in extremely noisy images. Averaging method is needed to calculate a high signal-to-noise ratio (SNR) structure from these noisy images. All the molecules must have the same inner conformation to within the resolution limit of the reconstruction, otherwise the averaging is meaningless.

To start a single particle reconstruction, all we need is cryo-EM micrographs of randomly distributed particles and reconstruction software (e.g. IMAGIC, SPIDER, EMAN). A typical reconstruction process shows as Figure 4.

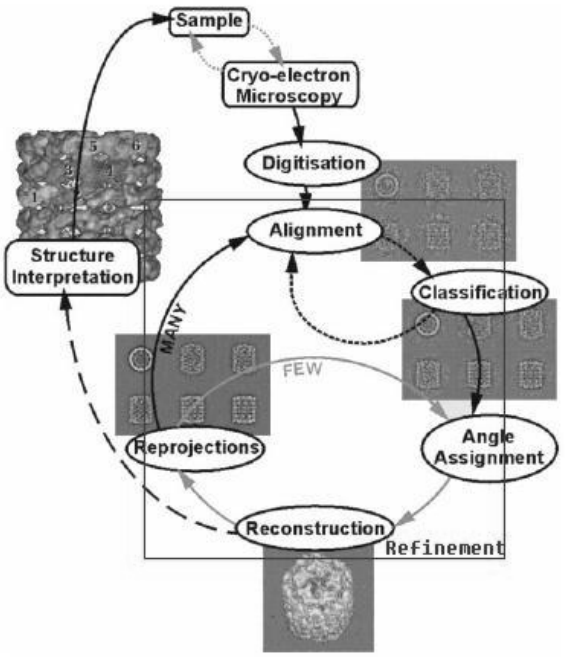

Figure 4. *The diagram of single particle reconstruction process of IMAGIC (van Heel et al., 2000)*

Generally speaking, image processing of 3DEM includes several steps:
(1). Single particle selection

Normally, only about 500 particles can be selected from a single EM micrograph, but a typical 3DEM reconstruction needs more than tens of thousand of particles. The micrographs are very noisy images due to the low dose exposure of cryo-EM. It is too difficult for a person to select large amount of particles required for 3DEM manually.
Automated or semi-automated software was created in need to accelerate this task. The software, Cyclops, designed in our group (Plaisier et al., 2007) includes an automated function to select single particles. Different methods are available in the software to locate the potential particles, such as the methods of local average, local variance and cross-correlation. In this thesis, I describe my contribution to this program in chapter 2.

(2). Filtering & centering
An optional pre-processing step is to filter the particle images with a low pass filter, erasing the high frequency noise (as well as a little information detail).
Mislocated intensities caused by the contrast transfer function (CTF) of the electron microscope have to be phase corrected at this step. That is so called CTF phase correction. Further amplitude correction will be needed in a later step for full CTF correction. In chapter 3 of this my thesis I discuss a novel approach to these corrections.
Particles are centered in several alignment cycles, in which the cross correlation between each individual image and the overall average image (of a given data set) is calculated.

(3). Classifying & averaging
A classification step is required to assign particles to different classes, in which the projections are assumed to be taken from the same view/angle. One of the classification methods is Multivariate Statistical Analysis (MSA) (van Heel et al., 2000). In this method, Principal Components Analysis (PCA) is applied to solve the problem caused by high noise in the images, after a time consuming procedure named multi-reference alignment (or reference supervised alignment). Another classification method is reference supervised classification if coarse starting model is available. A particle image is compared with all the reference images and is then assigned to the class corresponding to the most similar reference image.
Subsequently, an average image is calculated for each class to get high signal-to-noise ratio image. CTF amplitude correction is normally performed in this stage.

(4). 3D reconstruction

According to the common-line projection theorem, two different 2D projections of the same 3D object must have a 1D line projection in common. Relative Euler angles can be assigned for each average image in an angular reconstruction.

Once the Euler angles are assigned, average images are back projected to get a 3D model. This procedure is normally done in Fourier space, because every projection image is a section of 3D model in Fourier transform Back projection can be conveniently implemented by inserting the image in Fourier space and then transferring back to get the real space model.

(5). Refinement

The reconstructed 3D model resulting from the first iteration usually has a sub-optimal resolution. An iterative refinement aiming at higher resolution is then necessary. The rough model is re-projected in many directions, providing a set of reference images. Chapter 2 of my thesis describes an optimal sampling of rotational space to generate a minimal set of reference images with a maximal covering of potential orientations. The set of reference images is used in the subsequent iterative alignment and classification steps.

Refinement is the most time consuming step in 3DEM. For instance, on Pentium 4/1.6G/Linux PC,

1500 particles need ~5 hours per iteration; 2500 particles need ~11 hours per iteration. So how about 100,000 particles? And more particles if an even higher resolution is required? It may need days, weeks, or even longer. So, most state-of-art reconstructions are carried out on a parallel computing facility such as a supercomputer or a computer cluster.

Although there is a reasonably wide choice in software for 3D reconstruction (such as EMAN, SPIDER, IMAGIC, etc.), the method of 3DEM is still developing rapidly, since the cryo-EM technique started booming in the most recent 10 years. The main difficulties of this method are: low resolution, high noise, time consuming calculations and semi-automated software, still leave enough space for improvement.

1.4 Basics of electron diffraction and structural reconstruction

When the electron beam in a TEM passes through a thin (e.g. <100 nm) crystalline layer, the electrons scatter and interfere with each other and (if the microscope is set to the proper mode)a diffraction pattern can be observed on a fluorescent screen or be recorded on film, image plate (e.g. Figure 3B) or a CCD camera.
The constructive interference of the electrons observed as spots in the diffraction pattern can be expressed by the Bragg's law (Bragg, 1913):

$n\lambda=2d\cdot\sin\theta$,

Here, n is a given integer. λ is the wavelength of electrons. d is the spacing between the planes in the atomic lattice. θ is the angle between the incident beam and the scattering planes. Figure 5 explain both the constructive and destructive interferences.

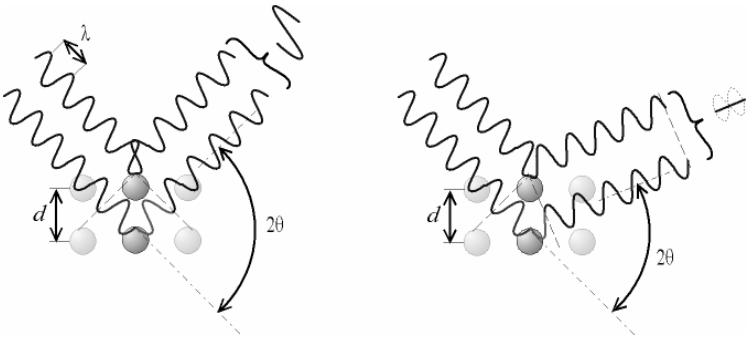

Figure 5. *According to the 2θ deviation, the phase shift causes constructive (left figure) or destructive (right figure) interferences. The interference is constructive when the phase shift is a multiple of 2π. (From Wikipedia)*

Theoretically, diffraction patterns are Fourier transformations of their projection images on the Ewald sphere. If the phases of the diffraction patterns from a crystal are known, these patterns are mathematically equivalent to the projection images, hence they can be used to reconstruct the atomic structure.

Electron diffraction is widely used in material science for analyzing the structure of metals and alloys. In structural biology, the application is still limited to, for instance, structure analysis of 2D and 1D crystals. Up to now, there is no existing way to obtain a 3D structure from the diffraction images of a 3D protein crystal. The difficulties mainly lie in:

(i) The mathematical equivalence between (phased) electron diffraction patterns and their corresponding projection structures are compromised by the multiple scattering of electrons (dynamic diffraction). Even when the thickness of the sample is less than 100 nm, dynamic diffraction still affects the data.

(ii) Protein crystals are susceptible to radiation damage caused by the electron beam. Some researchers are trying to solve the structure of 3D nano-crystals by using tilt series, which is similar to the technique of tomography in diffraction mode as is prevalent in X-ray crystallography. Unfortunately, this is not (yet) suitable for the beam-sensitive protein crystals with current electron detection methods.

(iii) Electron diffraction in TEM still needs lots of manual intervention. For example, locating the crystals in image mode and tilting the sample manually are time-consuming operations. Compared to highly automated X-ray diffraction experiments, electron diffraction is still extremely tedious.

In the research described in chapter 5, nano-crystals and the new technique of precession of the electron beam were used to reduce the dynamic diffraction problem. Clear electron diffraction patterns could be acquired for structure determination. To solve the atomic structure from the electron diffraction patterns of protein nano-crystals, following steps are required:

(i) Background removal and spot location

Firstly, center the diffraction images and remove the strong background caused by the undiffracted electron beam. A Patterson map can be used for centering. If a beam stop exists, its shadow should be taken into account. Then one needs to locate diffraction spots, extract their coordinates and calculate the intensities of the spots in the pattern.

(ii) Unit cell determination
Finding the unit cell parameters from randomly oriented diffraction patterns is essential for structure determination. Existing algorithms from X-ray crystallography and tilt series are not usable, as only single shots of crystals can be recorded, hence a new algorithm had to be created to deal with the multiple patterns with unknown orientation from multiple crystals.

(iii) Indexing
The randomly distributed orientation angles need to be determined, using the found unit cell in step two. The reflections of every electron diffraction image are thus indexed.

(iv) Intensity integration and subsequent steps in structure determination and refinement
When the indices and their corresponding locations on the diffraction pattern are known, methods from X-ray crystallography can be used to reconstruct the 3D spot lattices in reciprocal space. Phase recovery and iterative refinement are essential for determining the atomic structure.

1.5 Outline of this thesis

Chapter 2 to chapter 4 focus on single particle analysis, which includes both the methods employed in the single particle reconstruction and the practical 3DEM reconstruction of the macromolecular model of a 50S ribosomal complex. In **chapter 2**, new modules in cryo-EM, automated carbon masking and quaternion based rotation space sampling, are presented. The new modules were implemented and tested in Cyclops software. In **chapter 3**, a novel approximation method of CTF amplitude correction for 3D single particle reconstruction is described. This new method yields higher resolution models compared with to traditional CTF correction methods and shows better convergence in practice. **Chapter 4**, reports 3DEM reconstructions (with a highest resolution of 10Å) of macromolecular ribosomal complexes of stalled 50S ribosomal particles. They sow how Hsp15 rescues heat-shocked, prematurely dissociated 50S ribosomal particles. This 3DEM reconstruction project (the first

project in my Ph.D research period) required reconstructing multiple asymmetric macromolecules. Until now, it is still very challenging work to determine EM models of asymmetric complexes at such resolutions.

In chapter 5 and 6, I describe progress in analysing the random electron diffraction images of 3D protein crystals. In **chapter 5**, the second main topic of my Ph D research, discusses a brand new approach to structure determination compared to the traditional X-ray and NMR technologies. A new algorithm to determine unit cells from a set of randomly oriented diffraction patterns is presented here. Unit cell determination is the first step to solve a structure in crystallography. **Chapter 6** describes the implementation of these algorithms and includes a user manual of the EDiff software, which is used for searching unit cell parameters and indexing well-oriented patterns.

Finally, **chapter 7** gives a summary and concludes with future perspectives of my research.

References

Bragg, W.L. (1913). "The Diffraction of Short Electromagnetic Waves by a Crystal", *Proceedings of the Cambridge Philosophical Society*, 17, 43–57.

Georgieva, D.G., Kuil, M.E., Oosterkamp, T.H., Zandbergen, H.W., Abrahams, J.P. (2007). Heterogeneous crystallization of protein nano-crystals. *Acta Crystallogr. D* 63, 564-570.

Henderson R. (2004). Realizing the potential of electron cryo-microcopy. *Q. Rev. Biophys*. **37**, 3-13.

Plaisier J.R., Jiang L., Abrahams J.P., (2007). Cyclops: New modular software suite for cryo-EM. *J. Struct. Biol.* 157, 19-27.

van Heel, M., Gowen, B., Matadeen, R., Orlova, E.V., Finn, R., Pape, T., Cohen, D., Stark, H., Schmidt, R., Schatz, M., Patwardhan, A., (2000). Single-particle electron cryo-microscopy: towards atomic resolution. *Q Rev Biophys* 33, 307-69.

Williams, D.B., Carter, C.B. (1996). Transmission electron microscopy: a textbook for materials science. New York: Plenum Press. ISBN 030645324X.

Yu, X., Jin, L., Zhou, Z.H., (2008). 3.88 A structure of cytoplasmic polyhedrosis virus by cryo-electron microscopy. *NATURE* 453, 415-419.

Zhou, Z.H., (2008). Towards atomic resolution structural determination by single particle cryo-electron microscopy. *Curr. Opin. Struc. Biol.* 18, 218-228

Chapter 2

Automated carbon masking and particle picking in data preparation for single particles

Adapted from: Plaisier, J.R., Jiang, L., Abrahams, J.P., 2007. Cyclops: New modular software suite for cryo-EM. J. Struct. Biol. 157, 19-27.

Abstract

Two new algorithms, automated carbon masking and quaternion based rotation space sampling for automated particle picking, are presented here. They are implemented as plug-ins in the Cyclops software suite and are intended for data preparation for 3D single particle reconstruction. Cyclops is a new computer program designed as a graphical front-end that allows easy control and interaction with tasks and programs for 3D reconstruction.

Automating a particle search needs an algorithm that finds out where in the image the search has to be done. Normally only the particles in the holes (circular or irregular) of the carbon layer are of use. Currently no other automatic carbon masking algorithm for EM image processing exists. Traditional edge detection and segmentation algorithms do not work due to the extremely high noise in cryo-EM images. The new masking algorithm is based on the relatively high variance within carbon regions and gives good results.

A quaternion is a 4D number that can be used to represent and manipulate rotations in 3D space. The uniform sampling of rotations in 2D space is straightforward, but for rotations in 3D space, uniform sampling is more problematic. With the help of quaternion theory, we implemented an algorithm for uniform sampling in 3D rotation space that is based on subdivision of the regular polytopes in 4 dimensions. The algorithm can be used in single particle picking and alignment using a set of projection

classes from a known or inferred low resolution 3D model.

2.1 Introduction

In recent years the resolution obtained in three-dimensional reconstruction of biological complexes using cryo-EM has been considerably improved both through better instrumentation and new software tools. Simultaneously, more effort has been put into automation of the data collection and processing steps. As a result of these developments a large amount of software for cryo-EM is now available. At the same time there is still considerable potential for improvement in terms of resolution, automation and ease of use.

In cryo-EM single particle reconstruction, the vast majority of particle projections are picked when the low resolution 3D structure of the complex is (or could be) known. This additional information should be used, as it allows cross-correlation searches, which are more objective than hand-picking projections, and have a better yield than automatic procedures based on local density or variance. However, such cross-correlation searches are expensive in terms of computer resources, as every distinctive view and orientation of the low resolution 3D structure requires a separate search.

There are several ways of speeding up such model-inspired particle picking. Most importantly use is made of the correlation theorem, which states that the product of the Fourier transform of one function with the complex conjugate of the Fourier transform of another, is the Fourier transform of their correlation. Proper local and resolution dependent scaling are essential to avoid false positives, but in general this is fairly straightforward. As discrete Fourier transforms are calculated using FFT routines, numerically efficient algorithms result. However, additional optimizations are still required, including two optimizations we designed and implemented in Cyclops.

First, when dealing with samples deposited on holey carbon, it often is important to select only those particles that are suspended in the film of vitreous ice and exclude particles that have attached themselves to the carbon. In order to automate recognition

of the carbon region, so that it can be excluded from computerized particle searches, we developed a new algorithm that is discussed below.

Second, efficiency can be increased if the list of 3D projections of the low resolution model used for automated correlation searches is sampled as sparsely as possible, implying uniform sampling. As uniform Eulerian or polar angle sampling produces a non-uniform set of orientations, in which certain orientations occur far more often than others, we developed an algorithm that generates such a uniform set of orientations using unit quaternions. We also discuss this new algorithm below.

2.2 Methods

The new methods of automated carbon masking and uniform sampling of rotational space for a model based particle selection have now been implemented as plug-ins in Cyclops software.

2.2.1 Automated carbon masker

Fully automated particle picking requires a masking procedure that identifies the areas of the micrograph that contain the useful data. Usually the microscopist is only interested in particles within the holes of the carbon layer. One way of finding the proper regions is to use a carbon layer with a regular grid of circular holes. These layers, however, are not (yet) being used routinely and most of the times the holes are irregular in both size and spacing.

Currently no other automatic carbon masking algorithm for EM image processing exists. Traditional edge detection and segmentation algorithms do not work due to the extreme high noise in this type of cryo-EM image. Here we present a new masking algorithm which is based on the relatively high variance within carbon regions. Since this is also a property of regions containing aggregates, these are also masked by the method. The method consists of a series of image processing steps, which try to keep the edge information of EM images as much as possible while dealing with the high

noise levels.

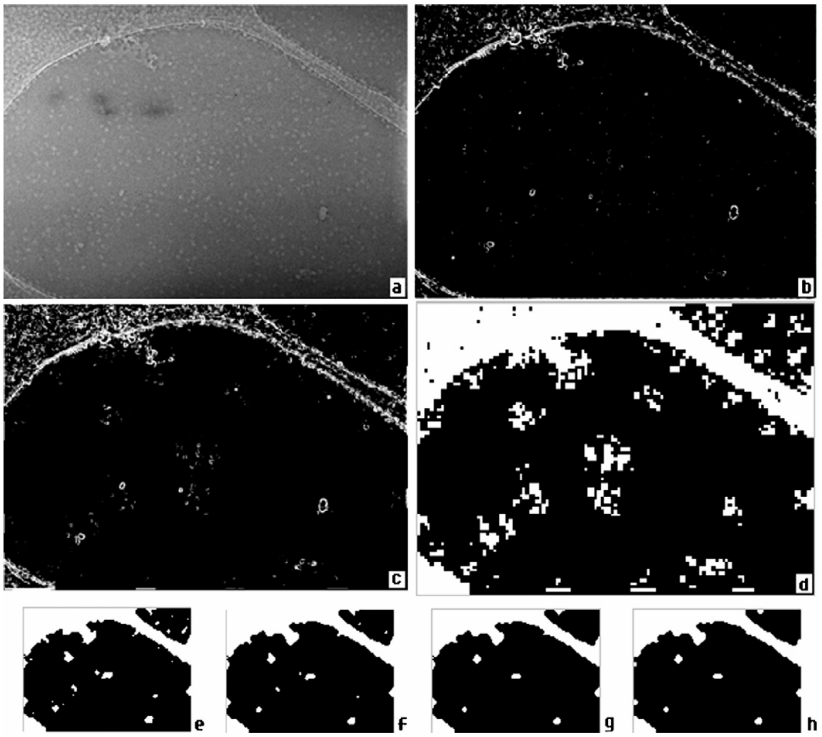

Figure 1. *Intermediate results of the carbon masking algorithm on a micrographs of 50S ribosomal subunits showing: (a) original image, (b) result of edge detection, (c) removal of sparse points and growth of masked regions, (d) initial mask, (e–h) iterative closing of the (scaled down) initial mask.*

The algorithm for automated masking of the carbon comprises the following steps: First, the image is scaled down to a smaller size by binning $n \times n$ pixels, where n is an integer number, thus speeding up processing and suppressing the noise level by averaging (Fig. 1a). Second, edge detection with a large size Prewitt operator (Prewitt, 1970) is applied, and the result is converted to a binary map using a self-adaptive threshold based on the statistics of the gray scale distribution of the image (Chang et al., 1995) (Fig. 1b). Next, sparse points, usually located outside the carbon layer, are removed from the binary map. The amount of pixels with value 1 within a given distance of the pixel examined must exceed a threshold, otherwise the pixel is set to

zero. This leaves most of the points in a carbon region, whereas the sparse points in regions with just vitreous ice are erased.

Subsequently, the regions near every none-zero pixel are searched in the map resulting from the edge detection result of the second step using a lower threshold in order to construct a new binary map. This allows the regions already masked to grow and holes in the mask to be filled leading to better segmentation (Fig. 1c). Next, an initial mask image is created by binning the binary map by a large factor (10 × 10 pixels) (Fig. 1d).

In the last step, a closing process for the mask image is performed. In the primary mask image some holes are present in carbon regions, and some false positive points in non-carbon regions. A new algorithm is used to close and smooth the image (Fig. 1e-h). The basic idea is that the edge of the carbon region is continuous and smooth and doesn't have sharp turns. A masked point on the edge of a carbon region should have at least four masked neighbors or the mask at this pixel will be removed. A similar rule for unmasked points is applied. After several, normally 5–6, of these iterative closing operations, the mask map will converge to a nice map with smooth edges. By default five iterations are performed, but this value may be changed by the user.

The plug-in produces mask images for carbon regions of the EM micrographs, but large ice aggregates and over-crowded blocks are masked out as well.

In our experience, the module works well for most EM images, producing adequate masks in ~95% of cases.

2.2.2 Even sampling of 3D rotation space

We define the *angular distance* to be the angle about a common rotation axis that maps one object onto another. The centres of mass of both objects are superimposed, and the rotation axis goes through this joint centre of mass. Orientation space is sampled by a discrete set of 3D orientations with a precision of Δ if the angular distance between any orientation from the continuum of possibilities *and* at least one orientation from the sampled set, is smaller than Δ.

There are many ways to sample orientations with a given angular distance. One example is Eulerian sampling, where each of the Euler angles is sampled by Δ and all possible combinations of (α,β,γ) are generated. There are many definitions of the Eulerian rotation angles, and here we use the convention of a rotation by α about the Z-axis, then a rotation of β about the new Y axis and finally a rotation of γ about the new Z-axis. Clearly, when β=0, only the sum of α and γ is defined, a property also known as a gimbal lock. At even sampling of Euler angles, rotations with a final rotation axis close to the Z-axis are therefore overrepresented, resulting in a non-uniform distribution of orientations in 3D rotation space.

Polar angle sampling suffers from similar problems. Here the orientation is defined by the angles (ϕ, ψ, κ), where κ is the right handed rotation about an axis with polar coordinates ϕ and ψ. Uniform sampling of the polar angles is also inefficient, as at (κ=0), ϕ and ψ are undefined, and at (ψ=π/2), ϕ is undefined. Therefore, in uniform polar angle sampling, orientations around (κ=0) and (ψ=π/2) are overrepresented, again resulting in a non-uniform distribution of orientations in 3D rotation space. Sampling of ϕ and ψ does not have to be linear, but is also possible to use platonic solids like the dodecahedron and the icosahedron. Here, the vertices of the polyhedron can be used as sampling points covering the sphere uniformly. The sampling density of ϕ and ψ may be increased by subsampling the triangular or pentagonal faces of the polyhedron (Yershova and LaValle, 2004). This sampling, however, only describes a rotation with 2 degrees of freedom (2D). The in-plane rotation j still needs to be sampled in a separate step and the same objections remain: orientations crowd around (κ = 0).

Orientations can also be defined by quaternions, which do allow uniform sampling of rotational space. Quaternions are 4D complex numbers of the form:

$$\mathbf{q} = a + x\mathbf{i} + y\mathbf{j} + z\mathbf{k}$$

where: $\mathbf{i}^2 = \mathbf{j}^2 = \mathbf{k}^2 = -1$

$\mathbf{jk} = -\mathbf{kj} = \mathbf{i}$

$\mathbf{ki} = -\mathbf{ik} = \mathbf{j}$

$$\mathbf{ij} = -\mathbf{ji} = \mathbf{k}$$

Rather than a real axis and a *single* imaginary axis as in ordinary, 2D complex numbers, quaternions have a real axis and *three* orthogonal imaginary axes. The orthogonal directions of these axes are defined by the unit quaternions **i**, **j** and **k**. Arithmetic with quaternions is straightforward, but multiplication does not commute, e.g. $\mathbf{jk} = -\mathbf{kj}$. In analogy to complex numbers, the following properties of a quaternion are defined:

- Conjugation: $\mathbf{q}^* = a - x\mathbf{i} - y\mathbf{j} - z\mathbf{k}$
- Sum: $(\mathbf{q}_1 + \mathbf{q}_2)^* = \mathbf{q}_1^* + \mathbf{q}_2^*$
- Product: $(\mathbf{q}_1\mathbf{q}_2)^* = \mathbf{q}_2^*\mathbf{q}_1^*$
- Magnitude: $|\mathbf{q}| = \sqrt{(\mathbf{q}\mathbf{q}^*)}$
- Real part: $\mathbf{q} + \mathbf{q}^* = 2a$

Quaternions are attractive for describing orientations. If:

$\mathbf{q}\mathbf{q}^* = 1$ (**q** is a unit length quaternion)
$\mathbf{p} + \mathbf{p}^* = 0$ (the real part of **p** is zero)
$\mathbf{p'} = \mathbf{q}\mathbf{p}\mathbf{q}^*$

then **p'** is related to **p** by a 3D rotation in imaginary quaternion space. The axis about which **p** is rotated to generate **p**' is $(x\mathbf{i} + y\mathbf{j} + z\mathbf{k})$ and the angle of rotation is (2acos(a)). Another useful notation of a unit length quaternion therefore is:

$$\mathbf{q} = \cos(\kappa/2) + x\mathbf{i} + y\mathbf{j} + z\mathbf{k},$$

where κ is the angle of rotation and (x,y,z) is the positive direction of the rotation axis.

Suppose $\mathbf{q}_1$ and $\mathbf{q}_2$ are unit quaternions, then both define a 3D rotation of a volume V, generating two copies V_1 and V_2, respectively. This being the case, the operation that rotates V_1 onto V_2 is defined by the quaternion product $\mathbf{q}_2(\mathbf{q}_1^*)$. The angular distance ($\Delta_{1,2}$) between the two objects is given by the real part of the quaternion $\mathbf{q}_2(\mathbf{q}_1^*)$ according to:

$$\cos(\Delta_{1,2} / 2) = (\mathbf{q}_2\mathbf{q}_1^* + (\mathbf{q}_2\mathbf{q}_1^*)^*)/2$$

$$= (\mathbf{q}_2\mathbf{q}_1^* + \mathbf{q}_1\mathbf{q}_2^*)/2 \qquad (1)$$

The orthogonal distance between $\mathbf{q}_1$ and $\mathbf{q}_2$ is given by:

$$\begin{aligned} |\mathbf{q}_1-\mathbf{q}_2|^2 &= (\mathbf{q}_1-\mathbf{q}_2)(\mathbf{q}_1-\mathbf{q}_2)^* \\ &= (\mathbf{q}_1-\mathbf{q}_2)(\mathbf{q}_1^*-\mathbf{q}_2^*) \\ &= \mathbf{q}_1\mathbf{q}_1^* - \mathbf{q}_1\mathbf{q}_2^* - \mathbf{q}_2\mathbf{q}_1^* + \mathbf{q}_2\mathbf{q}_2^* \\ &= 1 - \mathbf{q}_1\mathbf{q}_2^* - \mathbf{q}_2\mathbf{q}_1^* + 1 \qquad (2) \end{aligned}$$

Substitution of Eq. (1) in Eq. (2) shows that the orthogonal distance between two unit quaternions $\mathbf{q}_1$ and $\mathbf{q}_2$ is strictly related to the angular distance ($\Delta_{1,2}$) between the two new objects that are generated by rotating an object using either **q1** or with **q2**, respectively:

$$\cos(\Delta_{1,2} / 2) = 1 - |\mathbf{q}_1-\mathbf{q}_2|^2 / 2 \qquad (3)$$

Hence the problem of uniformly sampling 3D rotations is reduced to the more straightforward task of uniformly sampling the 4D hypersphere of unit quaternions. In other words, we need to uniformly distribute the quaternions over the hypersurface. When done uniformly, the nearest neighbor distance can substitute $|\mathbf{q}_1-\mathbf{q}_2|$ in Eq. (3), establishing its association with Δ, the precision of sampling.

Platonic solids also exist in 4D space, where beasts like the hexacosichoron live, which has 1200 triangular faces and 120 legs (vertices). Similar to sub-sampling 3D platonic solids (which can generate better spherical approximations like the soccer ball), 4D platonic solids can also be sub-sampled if a higher precision is required (Yershova and LaValle, 2004). Fig. 2 shows a polar representation of 5880 rotations generated by subsampling the hexacosichoron. The angular distance between the rotations is about 7.59° . For comparison, naive Euler sampling of rotational space with a similar angular distance yields 53,088 rotations.

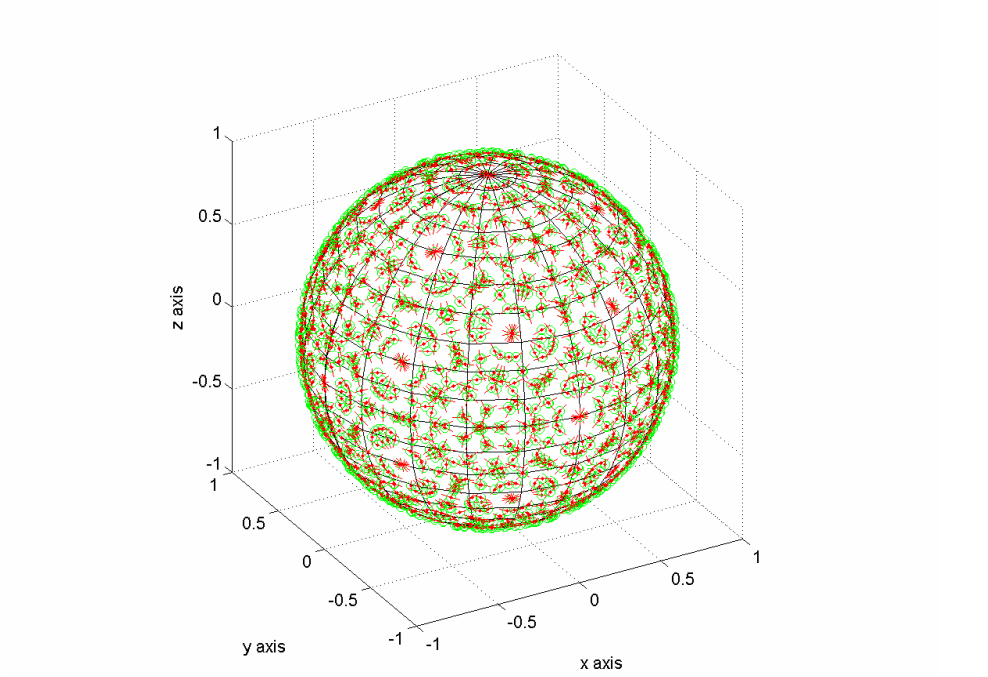

Figure 2. *Polar representation of 5880 sampled rotation quaternions using subsampling of the 4D hexacosichoron. Green points represent the viewing directions, whereas the red bars indicate the in plane rotations. The angular distance is about 7.59°.*

As a plug-in Cyclops, we implemented rotational sampling using all 4D platonic solids and their sub-sampled approximations. The user has the choice of generating sets of between 5 and 5880 orientations, corresponding to an angular precision of sampling that ranges between 2 π /5 and 2 π /30.

In the current application, the generated projections are used by a plug-in for particle picking using template matching. Fig. 6 shows a typical example of the result of template matching when picking 50S particles using 16 projections. Clearly, the plug-in detects the particles, but at these low-sampling densities the advantages versus Euler sampling for projection generation are fairly small. More significant improvement is achieved in, for instance, projection matching for orientation assignment.

2.3 Implementation

In the methods section, the principles and general methods have been described. Here we will focus on some technique details for implementation.

2.3.1 Implementation of automated carbon masking

To mask the carbon region, block ice and over-crowded particles, special image processing methods are needed for the micrographs with extremely high noise. Not all the known image processing operators are suitable to deal with high noise, though they may work very well in most other cases. We have to select and customize the operators to make them be really functional with lower signal-to-noise ratio (SNR) images.

Firstly, edge detection with a large Prewitt operator.

There are lots of known edge detectors, such as, the Roberts operator, Sobel operator, Laplacian or Gaussian, etc. Here 9*9 size Prewitt operator (see below, Prewitt H1 & H2) was selected, because it can also suppress noise by averaging. For instance, if every pixel is 12.7Å, a 9*9 size Prewitt operator covers 114.3Å (=9*12.7) width/height in real space, which is comparable to single particle size of 200-250 Å.

Edge detector Prewitt H1

-1	-1	-1	-1	0	1	1	1	1
-1	-1	-1	-1	0	1	1	1	1
-1	-1	-1	-1	0	1	1	1	1
-1	-1	-1	-1	0	1	1	1	1
-1	-1	-1	-1	0	1	1	1	1
-1	-1	-1	-1	0	1	1	1	1
-1	-1	-1	-1	0	1	1	1	1
-1	-1	-1	-1	0	1	1	1	1
-1	-1	-1	-1	0	1	1	1	1

Edge detector Prewitt H2

-1	-1	-1	-1	-1	-1	-1	-1	-1
-1	-1	-1	-1	-1	-1	-1	-1	-1
-1	-1	-1	-1	-1	-1	-1	-1	-1
-1	-1	-1	-1	-1	-1	-1	-1	-1
0	0	0	0	0	0	0	0	0
1	1	1	1	1	1	1	1	1
1	1	1	1	1	1	1	1	1
1	1	1	1	1	1	1	1	1
1	1	1	1	1	1	1	1	1

The filtering result (Fig. 1b) clearly shows the edge of carbon region, block ice and 50S particles.

Secondly, binarize image with selft-adaptive threshold.

When transferring grayscale images to binary images (only white and black colors), we can hardly find a fixed threshold which works well for all of the images. To solve this problem, an adaptive threshold needed to be implemented, which was realized here according to the statistic attributes of each of the images.

We chose $Threshold=\beta*Average$ (*Average* is the averaged grayscale value of all pixels). Clearly , the threshold is adaptive, it changes for every different image that has different total mean grayscale value. The parameter β can be changed by the user. The default value by experience is 2.3, which is stable for most of EM images. For EM photos taken in different facilities, it may need to be slightly adjusted.

The other techniques, generating a primary mask image and iterative closing of the final mask, have already been presented in the methods section.

In conclusion, the abundant variance information is well used in the algorithm of automated carbon masking. It relies on the fact that the carbon region and white ice region always have higher variance than the vitreous ice region. In a few cases, when the variance of the carbon region is very low for example, insufficient exposure of the

carbon region may cause wrongly classifying carbon regions as vitreous ice. In these cases, the failed data normally have lower quality and should be excluded in later processing.

2.3.2 Implementation of even sampling of 3D rotation space

Regular polytopes of 4D quaternion

Regular polytopes (also called platonic solids) are convex solids where all the building blocks (vertices, edges, faces, hyperfaces) have the same characteristics. That is, vertices have the same number of neighbours, edges are all the same length, polygons are all the same shape and area, and hyperfaces have the same volume (Bourke, 1993).

In 2 dimensions, the type of regular polytopes is infinite. E.g. regular triangle (3 edges), square (4 edges), right pentagon (5 edges), right hexagon (6 edges) etc.

In 3 dimensions, there are 5 regular polytopes (regular 3-polytopes) (Fig. 3): Tetrahedron (4 faces), Cube (6 faces), Octahedron (8 faces), Dodecahedron (12 faces), Icosahedron (20 faces).

In 4 dimensions, there are just 6 regular polytopes (regular 4-polytopes) (Fig. 4): Simplex (5 tetrahedral cells), Hypercube (8 cubic cells), Cross-polytope (16 tetrahedral cells), 24 cell (24 octahedral cells), 120 cell (120 dodecahedral cells), 600 cell (600 tetrahedral cells).

In geometry, a four-dimensional polytope is sometimes called a polychoron (plural: polychora).

Figure 3. *Five plantonic solids. (From wikipedia)*

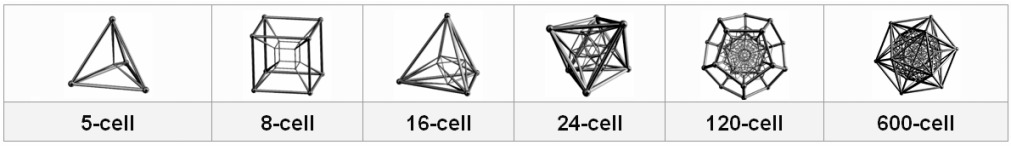

Figure 4. *Wireframe perspective projections of six convex regular 4-polytopes. (From wikipedia)*

The coordinates/quaternions of the vertices of these regular 4-polytopes are are known and can be found in numerous tables. E.g. the coordinates/quaternions of the vertices of unit 4-simplex are:

0	0	0	1
-0.559017	0.559017	0.559017	-0.25
0.559017	-0.559017	0.559017	-0.25
0.559017	0.559017	-0.559017	-0.25
-0.559017	-0.559017	-0.559017	-0.25

Evenly sampling rotation space by subdivision of regular polytopes of 4D quaternion and its application in 3DEM

As discussed above, the problem of uniformly sampling 3D rotations can be reduced to the more straightforward task of uniformly sampling the 4D hypersphere of unit quaternions. To uniformly sample the 4D quaternions, a subdivision procedure is performed:

(i) Select one of the regular 4-polytopes as the base of sampling, e.g. the simplex.

(ii) Then, construct a stack in the program and push the known quaternions of the 4-polytope onto the stack, e.g. the 5 vertices of Simplex are pushed onto the stack..

(iii) Calculate the geometric mean of each two quaternions/vertices in the stack, until all the combinations are used; then push the medians to the stack[1].

[1] Not all combinations of quaternions are allowed: only those combinations which result in a new quaternion with a length that is close to 1 are included. In the algorithm this is optimized by a specific selection process, but it goes too far to describe it here in great detail.

(iv) This subdivision step can be done iteratively, until the precision of sampling (the angular distance ($\Delta_{1,2}$) between two neighbor vertices) reaches the user requirement.

Subdivision into edges, faces, and cells of certain regular polytopes may result in a series of discrete number of quaternions in the stack: 5, 8, 15, 16, 24, 32, …, 5880, 6120, 26520 30360, … as showing in Table 1.

Basic platonic	Simplex	Cross-polytope	Hypercube	24 Cell	600 Cell	120 Cell
Basic vertices no.	5	8	16	24	120	600
Subdivision 1 iter.	15	32	40	120	840	1320
Subdivision 2 iter.	65	176	168	600	5880	6120
Subdivision 3 iter.	285	848	712	2712	30360	26520

Table 1. *Numbers of uniform quaternions generated by iterative subdivision of regular 4-polytopes.*

It means that we can not randomly select any number of quaternions for uniformly sampling 3D rotation space, but we can certainly select a sampling with the precision that is higher than what we need. To use the quaternions, we need to convert the 4D quaternions to Euler angles triples, which are accepted by most other programs to represent rotations.

An equivalent problem in 3D space can be solved by sampling the unit sphere using platonic solids like the dodecahedron and the icosahedron. The subdivision procedure was degraded to sampling 3-dimensional regular polytopes (regular 3-polytopes), generating uniform distributions on the 3D unit sphere. It is worth mentioning that although this distribution evenly samples rotation axes (e.g. Fig. 5), it does not evenly sample rotation space, as no in-plane rotation is included. Nevertheless, also this result is still very useful in current popular 3DEM reconstruction software packages.

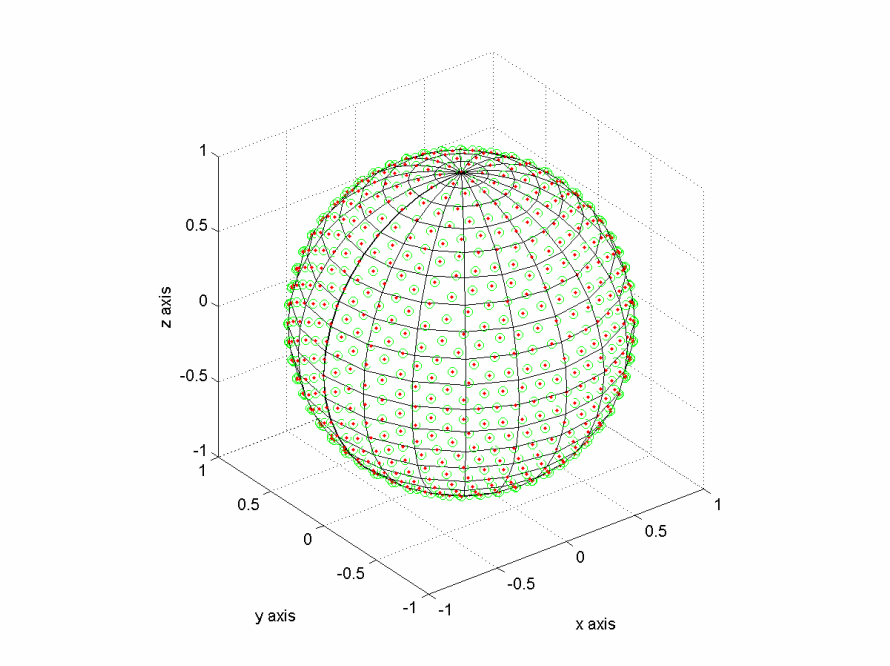

Figure 5. *Uniform sampling on the surface of 3D unit sphere based on subdivision of icosahedron, 1002 sampling points with ~6 ° angular distance. There is no in-plane rotation included (no red bar indicates the in-plane rotation compared with Figure 2).*

The new algorithm can be applied in model-based particle searching, in which the projections generated from a starting model and a set of Euler angles are used as references. For this searching, the in-plane rotation is not necessary, because the in-plane rotation is already included in the procedure.

2.3.3 Implementation as plug-ins in Cyclops

As mentioned above, new methods for automated carbon masking and uniform sampling of rotational space have been implemented as plug-ins in the Cyclops software (Fig. 6). Other methods currently implemented as Cyclops plug-ins cover a wide range of common image processing techniques, such as compression, low-, high- and band-pass filtering and edge detection. Methods previously implemented in the Tyson program (Plaisier, 2004) for automated selection of particles have now been

re-written as Cyclops plug-ins. The sorting of particles, a prominent feature of Tyson, is an intrinsic part of the Cyclops program.

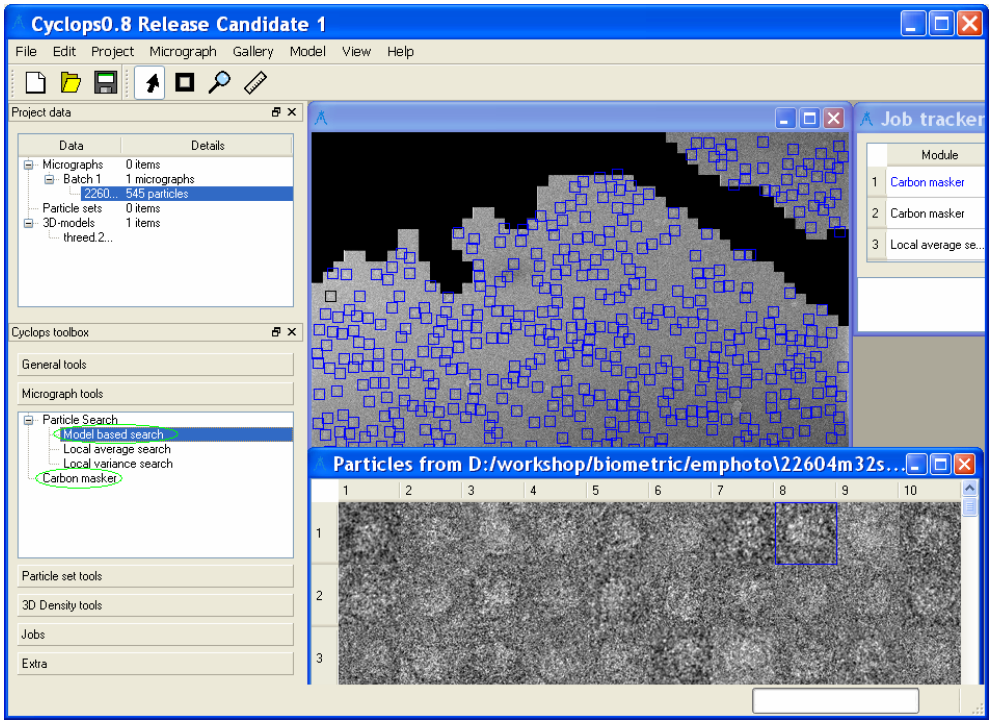

Figure 6. *Cyclops has a friendly graphic user interface (GUI) and plug-in architecture. The new algorithms for carbon masking and uniform sampling of rotation space (applied in model based particle searching) are marked by green ellipses. In the sub-window of micrograph, the black area is the result of automated carbon masking, blue boxes indicate selected particles, which are segmented and shown in the sub-window of particles gallery below.*

The new algorithms were written in C++/Python. They communicate with Cyclops through XML files. The XML file describes the input and the type of output it produces (e.g. a new particle set).
An XML file example of automated carbon masker:

```
<CyclopsPlugin>
    <module>Carbon masker</module>
```

```
    <category>Micrograph</category>
    <program>TMmicromasker.exe</program>
    <input>
        <label>Inputfile</label>
        <type>micrograph</type>
        <nr>multiple</nr>
    </input>
    <output>
        <type>mask</type>
        <nr>mutliple</nr>
    </output>
</CyclopsPlugin>
```

The information of the XML file is used to construct an input dialog window (shown in Fig. 7). A simple wrapper of Cyclops will pass the input parameters to the program.

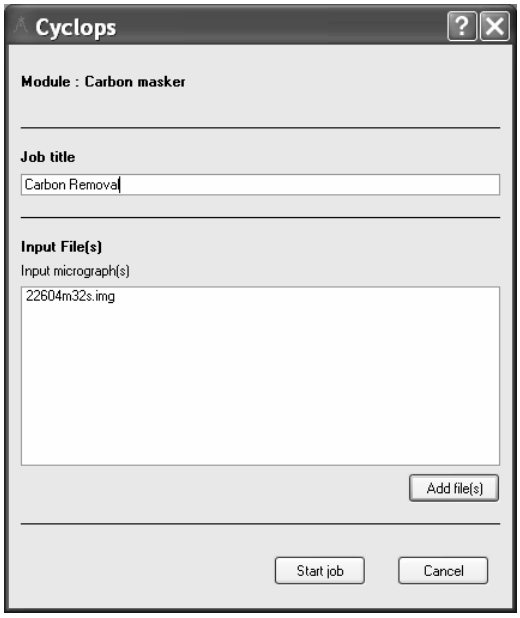

Figure 7. *Dialog window for entering the input parameters for the module of automated carbon masker.*

These applications are now routinely used through the Cyclops interface. Due to the

modular structure of Cyclops software, the plug-in applications can be easily extended and updated.

2.4 Conclusions

Two new algorithms dealing with the automation of particle selection are presented. The automated carbon masking routine allows automated removal of carbon region and only searching particles in the vitreous ice region of micrographs. The algorithm of even sampling of 3D rotation space can be used to generate uniform projections from a starting model and a set of rotational-equal-distance vectors. These projections are further used in a template matching procedure for particle picking. Both algorithms boost the automation and efficiency of particle selection in the step of data preparation. These algorithms greatly assisted in the structure determination of the stalled 50S ribosomal complexes described in chapter 4.

Acknowledgements

Thanks to Jasper R. Plaisier for his great help in embedding the new algorithms in Cyclops software suite. Cyclops is available under a GPL license and can be downloaded from http://www.bfsc.leidenuniv.nl/software/Cyclops.

References

Bourke, P., 1997. http://local.wasp.uwa.edu.au/~pbourke/geometry/platonic4d/

Chang, M., Kang, S., Rho, W., Kim, H., Kim, D., 1995. Improved binarization algorithm for document image by histogram and edge detection. Third International Conference on Document Analysis and Recognition (ICDAR'95), vol. 2, 636–643.

Plaisier, J.R., Koning, R.I., Koerten, H.K., van Heel, M., Abrahams, J.P., 2004. TYSON: robust searching, sorting and selecting of single particles in electron micrographs. J. Struct Biol. 145, 76–83.

Prewitt, J.M.S., 1970. Object enhancement and extraction. In: Lipkin, B.S., Rosenfield, A. (Eds.), In Picture Processing and Psychopictorics. Academic Press, New York, pp. 5–149.

Yershova, A., LaValle, S.M., 2004. Deterministic sampling methods for spheres and SO(3). In Proceedings of the IEEE International Conference on Robotics and Automation (ICRA).

Chapter 3

A Novel Approximation Method of CTF Amplitude Correction for 3D Single Particle Reconstruction

Submitted as: Jiang, L., Liu, Z., Georgieva, D., Maxim, K., Abrahams, J.P., 2009. A novel approximation method of CTF amplitude correction for 3D single particle reconstruction. Ultramicroscopy

Abstract

The typical resolution of three-dimensional reconstruction by cryo-EM single particle analysis is now being pushed up to and beyond the nanometer scale. Correction of the contrast transfer function (CTF) of electron microscopic images is essential for achieving such a high resolution. Various correction methods exist and are employed in popular reconstruction software packages. Here, we present a novel approximation method that corrects the amplitude modulation introduced by the contrast transfer function by convoluting the images with a piecewise continuous function. Our new approach can easily be implemented and incorporated into other packages. The implemented method yielded higher resolution reconstructions with data sets from both highly symmetric and asymmetric structures. It is an efficient alternative correction method that allows quick convergence of the 3D reconstruction and has a high tolerance for noisy images, thus easing a bottleneck in practical reconstruction of macromolecules.

3.1 Introduction

The last decade saw a substantial increase in the number of 3D structures determined by single particle cryo-EM reconstruction and the resolution of these reconstructions (~4-10 Å) is starting to approach a level that allows atomic interpretation of the structures (see reviews by Zhou 2008; Chiu et al., 2005). Essential was the development of procedures for accurate CTF estimation and correction of the measured image data. The instrumental aberration problem that affects electron microscopy images was recognized early (Thon 1966; Erickson and Klug 1970) and must be corrected for to allow the resolution to be extended beyond the first zero of the oscillating contrast transfer function (CTF). Multiple reconstruction software packages were adapted in this fashion to allow constructing high resolution 3D models e.g. IMAGIC (van Heel, 1979 & 1996), SPIDER (Frank et al., 1981 & 1996), XMIPP (Marabini et al., 1996; Sorzano et al., 2004a), EMAN (Ludtke et al., 1999), IMIRS (Liang et al., 2002) and others. About seven parameters (depending on the CTF model used) need to be determined in the CTF estimation for an accurate approximation. These parameters are subsequently used in the CTF correction procedure. The quality of the final 3DEM model relies on accurate CTF estimation and correction. This makes CTF estimation and correction one of the most delicate problems in 3D single particle reconstruction.

For CTF estimation, a number of semi-automatic tools are available (e.g. Zhou et al., 1996; van Heel et al., 2000; Huang et al., 2003; Fernández et al., 2006). There are also fully automatic CTF estimation tools, based on different methods, e.g. ARMA models of Xmipp (Velázquez-Muriel et al., 2003); ACE: Automated CTF Estimation (Mallick et al., 2005); Automatic CTF estimation based on multivariate statistical analysis (Sander et al., 2003). Here we describe a new method for correcting images optimally when (initial) estimates of the CTF parameters are available.

According to the theory (Erickson and Klug 1970; Thon 1971; Hanszen 1971), the image measured in TEM normally can be described in Fourier space as a function of the spatial frequency vector s by:

$$M(s) = CTF(s)F(s) + N(s) \quad (1)$$

M(s) is the Fourier transform of the measured image. *CTF(s)* is the contrast transfer function, which we assume here to be radially symmetrical. *CTF(s)* can be further described as consisting of two parts: *C(s)* and *E(s)*, that is, $CTF(s)=C(s)E(s)$. *E(s)* is the envelope function (essentially the Fourier transform of the image of the extended source in the back focal plane of the imaging system), the phase variable part *C(s)* is sometimes confusingly also called contrast transfer function. The CTF essentially is a dampened oscillating real function that passes through zero many times.

F(s) is the structure factor assuming the kinematic approximation (Frank 1996) and *N(s)* is Fourier transform of the detector readout and quantum noise. Strictly speaking, *F(s)* has a random component too, caused by disordered (solvent) density. This term is usually ignored, as it is subject to the same corrections as the structure factors corresponding to ordered density. Estimation procedures determine the parameters of the functions *CTF(s)* and *N(s)* to optimally fit the observed power spectral curve of rotation average of *M(s)*.

Different researchers may use different denotations for the frequency variable *s*, for example *f*, *k,* etc. Here we use *s* uniformly. The detailed formulation of the functions may also differ slightly in the different software packages.

Once estimates of the CTF and noise parameters are available, estimates of the functions of CTF and noise will be known. There are several solutions to use these in correcting the measured image data in 3D reconstruction software packages:

1. Filtering at the first zero of the CTF by truncating the high-resolution part after the first zero. No actual CTF correction is applied in this case. Usually it is suggested to use this procedure only for making the first prototype model and in other early stages of the structure determination.

2. Applying phase correction only – as it is, for instance, done in IMAGIC (van Heel et al., 2000). This is achieved by flipping phases of structure factors at spacings where the CTF dips below zero, whilst keeping the amplitudes intact. The

rationale of flipping the phases is that the phase plays a much more important role in the structure determination than the amplitude (Ramachandran & Srinivasan, 1970). The rationale for not correcting the amplitudes is that boosting low level amplitudes close to the CTF zeroes will deteriorate the overall signal-to-noise ratio in rings in Fourier space. Hence, only applying phase correction without bothering about the amplitudes, also has practical advantages.

3. Do both phase and amplitude correction. Complete CTF correction (or full CTF correction) is normally performed in two separate steps, first flipping the phase, and then applying amplitude correction. Due to it being theoretically optimal, the problem of full CTF correction is frequently addressed in the community of 3DEM methods research (e.g. Frank & Penczek, 1995; Zhu et al., 1997; Ludtke et al., 1999; Zubelli et al., 2003; Wan et al., 2004; Sorzano et al., 2004b; Grigorieff 2007).

A general approach to do full CTF correction is to find a deconvolution filter function *G(s)* so that we can estimate *F(s)* as follows:

$$\hat{F}(s) = G(s)M(s) \qquad (2)$$

To recover the amplitude of the object *F(s)*, a simple attempt is:

$$\hat{F}(s) = (1/CTF(s))M(s) \qquad (3)$$

Here $G(s) = 1/CTF(s)$. However, this attempt is not feasible in practice due to the problems of random noise and zeros of the CTF. The random noise cannot be removed directly[2]. It is expected to be reduced by averaging multiple images in one class[3]. The

[2] We do not discuss approaches that reduce noise by improved detectors or other experimental aspects of data collection (Medipix: a photon counting pixel detector; Plaisier et al., 2003), as these approaches are fully compatible with the improvements in data analysis discussed here.

[3] With class we mean the result of references/projections supervised classification or an automatic classification. In a class, images are assumed to be the projections from the same view of a 3D model and they are used to calculate a class average image.

CTF has many zeros with the changing of phase, it is relatively small at low frequencies and tends to zero at the high frequency end due to the shape of the envelope function. The restored image will be corrupted by noise, which will be enhanced upon division by the CTF in regions where the CTF is small (Penczek et al., 1997). All these features of CTF render the straightforward division by the CTF sub-optimal.

In full CTF correction, after the phase is flipped, several methods may be employed in amplitude correction to avoid dividing by zero and to prevent amplifying the noise while deconvoluting the contrast transfer function:

A. Wiener deconvolution

The Wiener filter is used widely in imaging processing (Gonzalez et al., 2003). An application of the Wiener filter (Schiske 1973) is used for amplitude correction (e.g. in SPIDER, EMAN). The Wiener deconvolution filter can be formulated in the frequency domain as follows:

$$G(s) = \frac{1}{H(s)}\left[\frac{|H(s)|^2}{|H(s)|^2 + 1/SNR(s)}\right] \qquad (4)$$

Here *H(s)* is the frequency transfer function, 1/*H(s)* is the inverse of the original system, corresponding to 1/ *CTF(s)* in the CTF correction. *SNR(s)*=S(s)/N(s) is the signal-to-noise ratio (SNR), S(s) is the signal intensity (=$CTF(s)^2F(s)^2$) and N(s) is the noise intensity (=$N(s)^2$).

In order to use the Wiener filter, one has to estimate or determine the SNR. Consequently, solution structure factors (the rotationally averaged curve of *F(s)*) need to be estimated independently, e.g. by a small angle X-ray scattering (SAX) experiment.

When there is low noise (SNR is very large), the term in the square brackets tends to 1, and the Wiener filter equals approximately the inverse of *H(s)*. However, when the noise is strong (SNR is very small), the term in the square brackets will decrease, thus suppressing the intensity of the noise – note that in this case also the signal is

suppressed strongly. The term within the square brackets is therefore a kind of amplitude optimization, fine-tuning the amplitude of the restored signal to minimize the mean square error between the original and the estimated signal.

The Wiener filter cannot recover missing information in the zero regions, and an adapted Wiener filter is needed to mediate the information of different defocus images at the same frequency and generate an integrated image. In 3D reconstruction, a set of images assigned to the same class is used in calculating such an integrated image (or class average image). Application of a Wiener filter in 3D reconstruction was described by Penczek et al., 1997. To describe the filter of the *n*'th data set in a formula (the notation is adapted here for convenience):

$$G(s) = \frac{SNR_n CTF_n^*(s)}{\sum_{n=1}^{N} SNR_n \left|CTF_n(s)\right|^2 + 1} \tag{5}$$

Where $CTF_n^*(s) = \frac{1}{CTF_n(s)}\left|CTF_n(s)\right|^2$. Collecting a defocus series data set covering the whole range of frequencies from zero to some limit of frequency of sampling, the adapted filter combines the data sets and performs CTF correction in Fourier space.

The application of the Wiener filter in 3D reconstruction needs an estimate of the spectral SNR, e.g. an X-ray scattering curve (solution structure factor) is necessary for this purpose. However, this is unavailable in many cases.

Moreover, the assumption that we have a sufficient number of different defocus images and the CTFs can jointly cover the whole Fourier space without a gap is not always true. For instance, in the reconstruction with a small angular sampling step for projections (e.g. 3 degrees), more than one thousand projections/classes can be used (especially for a model of C1 Symmetry); lots of classes contain a few particles only (e.g. less than 10) as a basis for generating a class average image. The Wiener filter method is not optimal in this case due to the large probability of superposition of multiple zeros. An accurate estimate of the CTF parameters is essential, otherwise the

merging of information pertaining to different particle images at the same frequency will lead to a breakdown of the continuity of the image in Fourier space.

B. Spatial frequency weighted averaging

Performing a weighted average of the images, where the weights vary with spatial frequency. (EMAN, Ludtke et al., 1999 & 2001) uses weight factors to avoid dividing by zero in amplitude correction. The weight factors in averaging the images in one class ($K_n\ (s)$) are given by:

$$K_n(s) = \frac{1}{C_n(s)E_n(s)} \frac{R_n(s)}{\sum_m R_m(s)} = \frac{C_n(s)E_n(s)}{\sum_m C_m(s)^2 E_m(s)^2} \qquad (6)$$

Where the subscript '*n*' denotes particle number and '*m*' denotes the total amount of particles in the class. The term $1/(C(s)E(s))$ is the inverse of CTF (the same function as the term $1/H(s)$ of the Wiener filter). $R_n(s)=C_n(s)^2E_n(s)^2/N_n(s)^2$ is used as the relative signal-to-noise ratio (SNR) for each particle. $N_n(s)^2$ is left out, assuming it to be approximately equal in different micrographs. If an estimate of the solution structure factor curve is known, the absolute SNR can be calculated and used instead of the relative SNR. In this case, this method actually acts as a Wiener filter. An additional Wiener filter or a low-pass Gaussian filter may still be applied to smooth the final model.

If there are only a few defocused images, this procedure may run into trouble of coincident zeros and in practice EMAN calculates the direct average.

C. Other methods.

Other ways of doing a full CTF correction have been tried as well, such as the iterative method given by Penczek (Penczek et al., 1997), the Iterative Data Refinement (IDR) technique (Sorzano et al., 2004b), and Chahine's method (Zubelli et al., 2003). Differing in important details,, these methods all attempt finding an approximation of the original image by iterative refinement or minimization of a residual function. Their

penalty is that they increase the time consumed by the 3D reconstruction.

CTF correction is a vital prerequisite for effective 3D reconstruction using 2D images obtained by electron microscopy. This explains why so many researchers are continuously, trying to improve existing methods and developing new ones. Here, we introduce a novel approximation filter for CTF correction. It is easily implemented and shows good convergence properties in iterative reconstruction refinement. Application of the filter proposed clearly improves the resolution and it is robust in tests with noisy, close-to-focus data sets.

3.2 Method

We propose a novel approach: we constructed continuous and differentiable function, which allows direct application of an inverse CTF filter in 3D reconstruction. The function contains no singularities in its approximation to the CTF. Since the simple attempt of *G(s)* = 1/ *CTF(s)* fails because of *CTF(s)* having zeros and other small values, the CTF curve is partially modified, avoiding zeros and preventing divisions by small values at high spatial frequencies. The modified curve must be continuous to avoid edge effects in Fourier filtering.

The reasons for trying this new approach are:

- There is no need to separately estimate the true structure factor (without the noise), so it can even be applied to a single image.
- If the CTF is not known very accurately, the method includes integration over the uncertainties of the CTF.
- Continuous, differentiable functions in general produce fewer artifacts in filtering and allow more robust refinement.

The proposed inverse filter can be described as:

$$G(s) = \begin{cases} 1/(C(s)\,\hat{E}(s)) & C(s) >= 0.5 \\ 1/((1-\sqrt{0.5-C(s)^2})\,\hat{E}(s)) & C(s) < 0.5 \end{cases} \qquad (7)$$

$$\hat{E}(s) = E(s)Sig(s - s_0) + N(s) \cdot \alpha \cdot (1 - Sig(s - s_0)) \quad (8)$$

Here, $\hat{E}(s)$ is an estimation of *E(s)*, $Sig(s - s_0)$ is a sigmoid function ($Sig(x)=1/(1+e^{-x})$) as is shown in Figure 1. The idea is to create a continuous and differentiable function (also continuous for derivatives of higher order) to 'glue' together the functions of *E(s)* at low frequency region and *N(s)* at the high frequency region, where the noise dominates the density measured. The scale factor α scales *N(s)* to the same level of *E(s)* at joint point S_0. The user selected value S_0 defines the frequency joint point of *N(s)* and *E(s)*. The sensible choice is $S_0=1/\sqrt{B}$, where *B* is the envelope B-factor of the CTF estimate. At this point, the SNR value diminishes quickly.

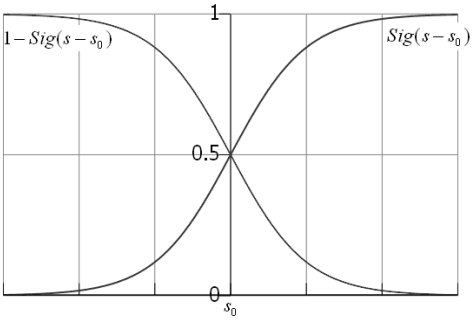

Figure 1 *The functions* $Sig(s - s_0)$ *and* $1 - Sig(s - s_0)$

The modified *G(s)* is a piecewise continuous function, which is continuous also in its first derivative. At the region near zeros (where $C(s) < 0.5$), the *C(s)* is modified to a piece of continuous arc $(1 - \sqrt{0.5 - C(s)^2})$, which has a minimum value of

approximately 0.2929 at the original zeros. The inverse of 0.2929 is a small number (~3.4). This simple modification makes the inverse deconvolution method feasible (figure 2 shows the curve of the approximation to the CTF, the numerator of *G(s)*). At the high frequency region, the numerator of *G(s)* still tends to zero, however, the estimation of *E(s)* ($\hat{E}(s)$) tends to be of the same order as *N(s)*. After filtering by *G(s)*, the intensity of the signal and the noise at high frequencies are only multiplied by a small number.

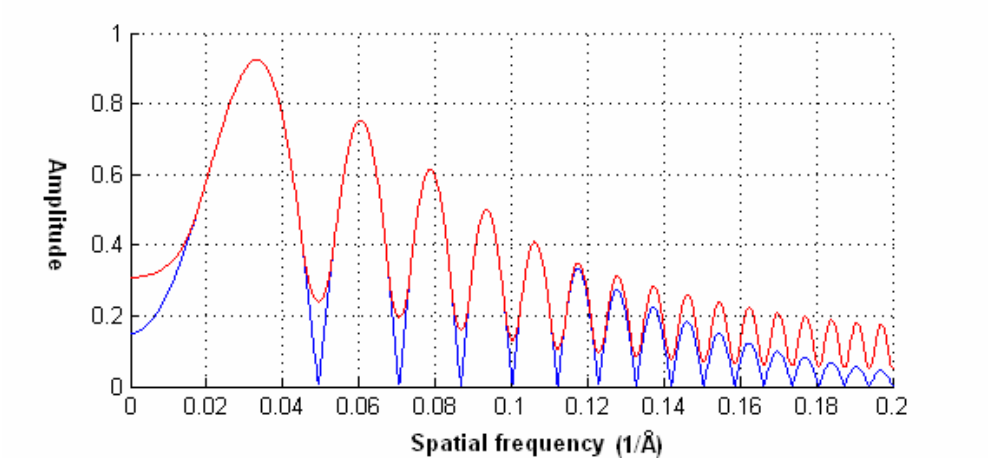

Figure 2. *Blue: Theoretical CTF curves after phase flipping. Red: The approximation of the CTF (=1/G(s)) used in the inverse filter (after phase flipping)*

The proposed function of *G(s)* is an approximation assuming noise and small uncertainties in the CTF parameters. In the absence of noise and full knowledge of the CTF, a better function can be formulated.

In the 3D reconstruction, noise is decreased in two stages of averaging: first in generating each of the class average images, then in 3D reconstruction, when thousands of class average images are combined to form a 3D model. By applying the new inverse filter the noise is amplified somewhat for a single particle image, but by a limited factor only (a maximum around 3.4 times at zeros in low frequency region).

Despite the new filter increasing both the signal and noise near zeros of the CTF, we show the averaging procedure to reduce the noise efficiently: the noise is still under control and the algorithm is stable.

Two new algorithms that apply the proposed function of *G(s)* have been implemented for calculating a class average image:

Algorithm of "direct CTF deconvolution": A class average image can be calculated by aligning and straightforward averaging of all the *G(s)* filtered images within a class. To distinguish our method from other conventional methods, we refer to it as "direct CTF deconvolution", as its filter *G(s)* can be used for calculating the class average image without a Wiener filter, which in a formula is $\hat{F}_c(s) = \frac{1}{N}\sum_{1}^{N} G(s)M(s)$. A wide low-pass Gaussian filter can still be used to erase the limited noise at high resolution. A Wiener filter or other filter can be an optional choice for the later processing stages, but by omitting it at this early stage, we can also circumvent some of its more problematic aspects (see above).

Algorithm of "filtered CTF correction": The proposed function of *G(s)* can also be used in combination with other full CTF correction methods, since most of them have an inverse term in the algorithm. For example, in the weighted average method (which is used by the 'ctfc' or 'ctfcw' options of EMAN software), the new function of *G(s)* can be used instead of the first term 1/(*C(s)E(s)*) of the weight factors in averaging the images. In this case, the implemented algorithm works like a selective filter, suppressing the noise only at regions near zeros and the high resolution end, in a manner adapted to each image.

These two new algorithms were implemented and tested in EMAN 1.6, and it also works for the newer version of EMAN 1.8. The algorithm of "filtered CTF correction" is implemented as a combination of the new function with the weighted average method of the EMAN refinement program, which also applies a Wiener filter.

We have tested and compared the new algorithms using a data set from a highly symmetric structure and one obtained from a structure with no internal symmetry.

3.3 Results

Two sample data were used to test the algorithms. First, we demonstrate the feasibility of the two new algorithms. Then, by comparing the results from conventional full CTF correction to the new algorithms, we show the new algorithms both have the advantage of better convergence, while both are stable in the reconstruction process of asymmetric macromolecules.

3.3.1. Highly symmetrical particles: a test with GroEL

The high resolution EM data of native free GroEL that we used, were kindly provided by Ludtke and Chiu for testing the algorithms. The data were first made available course material for the participants of the workshop on Single Particle Reconstruction and Visualization 2007 in Houston, USA. Sample preparation and data acquisition were described elsewhere (Ludtke et al., 2004). GroEL is a homotetradecameric protein consisting of two back-to-back stacked rings, each of them containing seven identical subunits. The rings have an outer diameter of 13.7 nm and inner diameter of 4.5 nm; each monomer has a molecular weight of 58 kDa (Braig et al., 1994; Hartl, 1996). GroEL is one of the typical test-beds for methods research in the field of 3DEM reconstruction (Ludtke et al., 2008; Stagg et al., 2008). A total 4169 particles (128 by 128 pixels in size, 2.08 Å/pixel) were selected from 12 micrographs with defocus ranging from 1.9-2.3 μm. D7 symmetry (14 fold symmetry) is imposed in the reconstruction, thus 58366 asymmetric subunits are used.

The algorithms were all tested using the same particle data set and starting model. The same set of projections was used as class references. The classification required for making the averaged images was imported from one single reference-supervised-classification procedure. Only the algorithms for making the average image (including full CTF correction, Figure 3) were different. The three models shown in Figure 4, were reconstructed from the same reference model and classification.

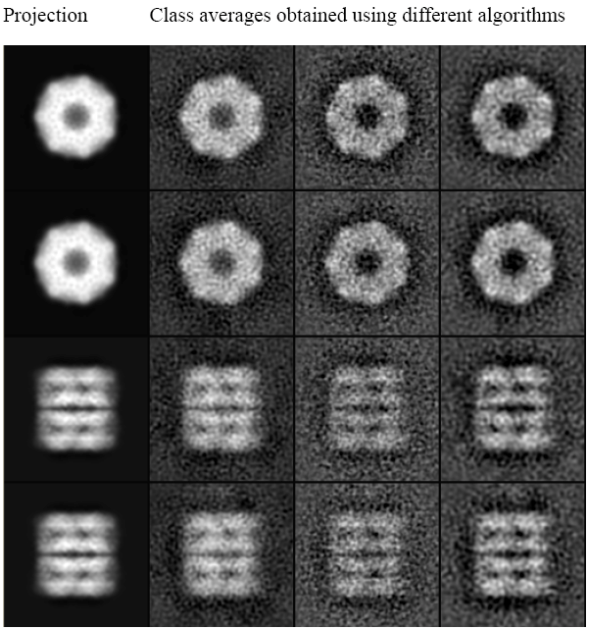

Figure 3. *Representative class averages of GroEL generated by different CTF correction algorithms. The second column is generated by the conventional full CTF correction algorithm. The third column is generated by the new direct CTF deconvolution algorithm. The last column is generated by the new filtered CTF correction algorithm, which combines the approximated inverse filter and the weighted average method.*

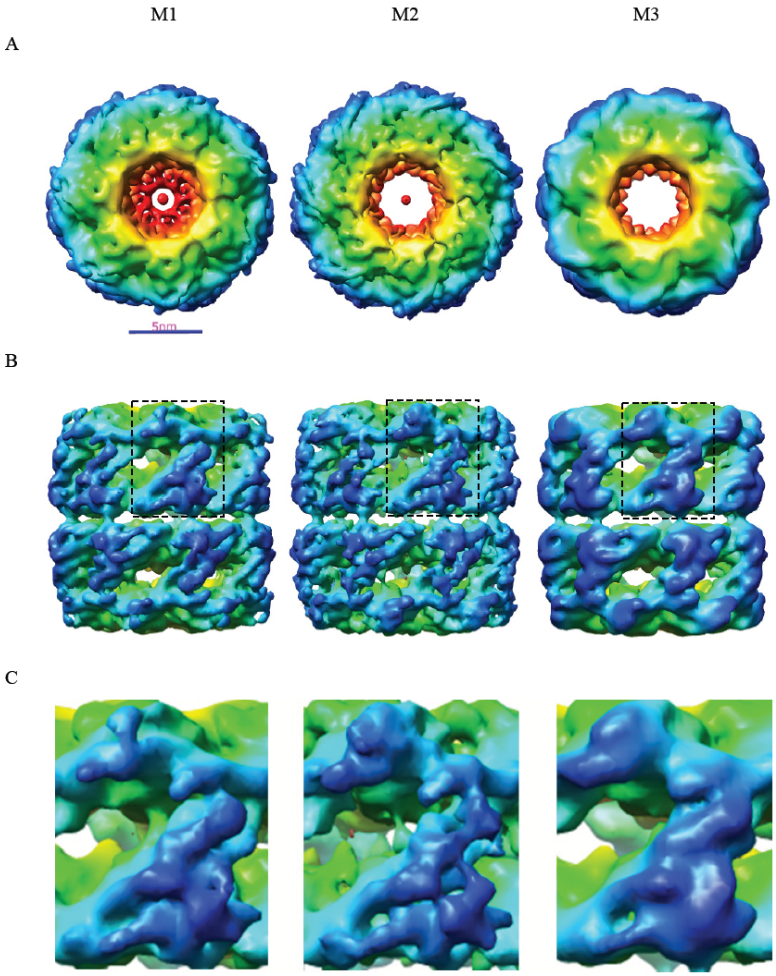

Figure 4. *Reconstructed models of GroEL generated with different CTF correction algorithms. M1(Column Left): The model obtained by conventional full CTF correction, resolution 7.9Å; M2(Middle): The model obtained by the "direct CTF deconvolution" algorithm, 7.0Å; M3(Right): The result of the "filtered CTF correction" algorithm, 8.6Å. A) Top views of three different models. B) Side views corresponding to A. The black dash line boxes indicate subunits for visually comparison. C) Views zoomed in for the indicated subunits in B.*

In Figure 4, the result of "the direct CTF deconvolution" algorithm (Middle model, M2) shows more detail than the conventional CTF correction algorithm (Left model, M1). The result of "the filtered CTF correction" algorithm (Right model, M3) looks like a low-pass-filtered model of the normal CTF correction. When the approximation deconvolution filter is combined with the normal CTF correction, it works more like a selective filter, suppressing the noise strongly.

The result of "the direct CTF deconvolution" algorithm – M2 has the best resolution based on an even-odd test and Fourier Shell Correlation (FSC) (Van Heel et al., 1986) with a threshold of 0.5 (Beckmann et al., 1997): 7.0 Å (Table I). It should be realized that such a test does not give an absolute resolution, but is a reflection of the internal consistency between model and data. This can be clouded by bias introduced by specific choices of envelopes, samplings, symmetries and starting models (Van Heel, 2005), and we were careful to ensure that these were identical for the various algorithms we tested. The resolution of M2 is around 1 Å better than that of M1, while M3 is a little bit over-filtered and lost some high resolution detail.

Table I. *Fourier Shell Correlation (FSC, 0.5 criterion) of different models of GroEL (M1: conventional CTF correction, M2: direct CTF convolution, M3: filtered CTF correction). The table indicates that for highly symmetrical particles the direct CTF convolution algorithm converges to a more self-consistent model that suffers less from model bias.*

Table I. Comparison of resolutions and inter-models similarity

Model	M1	M2	M3
Resolution (FSC* at 0.5)	7.9 Å	7.0 Å	8.6 Å
Similarity with Starting Model (FSC at 0.5)	5.3 Å	6.7 Å	8.3 Å

*FSC, Fourier Shell Correlation

One will also notice that the densities in the inner channels of these three modes are apparently different. It seems that M2 & M3 have less resolved structure in the channel, but actually there is almost no density in the inner channel (within 4.5nm diameter) of the X-ray structure of unliganded GroEL (PDBid: 1OEL, Braig et al., 1995). A recent

published higher resolution (~4Å) result of GroEL using cryo-EM reconstruction (Ludtke et al., 2008) also excludes the possible existence of additional ordered density in the inner channel of "live" GroEL in solution. All this confirms the validity of the new CTF correction algorithms. We will further address the "correctness" of the EM models in the discussion.

In order to compare the convergence of different algorithms, we also calculated the Fourier Shell Correlation (using the 0.5 criterion) between the results and the starting model for a rough comparison of the inter-models differences (Table I). Here the FSC value between models can be considered as a measure of inter-model similarity. From the comparison, we can see that M2 is 6.7Å similar to the starting model, while M1 is at 5.3Å. It shows that the "direct CTF deconvolution" method has better convergence properties: less model bias (it is more different from the starting model), smaller internal divergence (better resolution, more consistency between the models of even and odd numbered particles).

The test shows the two new algorithms to be feasible alternatives for other CTF correction algorithms, and suggests they have better convergence properties than the normal full CTF correction.

3.3.2. Asymmetrical particles: the stalled ribosomal 50S complex

The complex of a large ribosome subunit 50S with tRNA and heat shock protein 15 was used to test the new algorithms. The complex has a diameter of ~20 nm and weight of ~1,600 kDa. We used a set of 33,900 images containing 128 x 128 pixels recorded with a defocus ranging from 0.6 to 1.8 μm, (See Jiang et al., 2008). We collected close-to-focus micrographs with a low-dose exposure ($<10e^-/Å^2$), and therefore collected relatively noisy images. Single particles were selected and maintained by using the Cyclops software (Plaisier et al., 2007). For the 981 projections/classes used in the reconstruction, the average number of images per projection is around 34.

A model that had nearly converged to the final model (Jiang et al., 2008), was used as a common starting model for all the algorithms tested. After four iterations of refinement using the same data set and starting model, but using different CTF correction

algorithms, we compared the class average images and 3D reconstruction results in Figure 5 & 6. If we ran more rounds of iterative refinement, the method of normal CTF correction blew up because of the high level of noise in the test data.

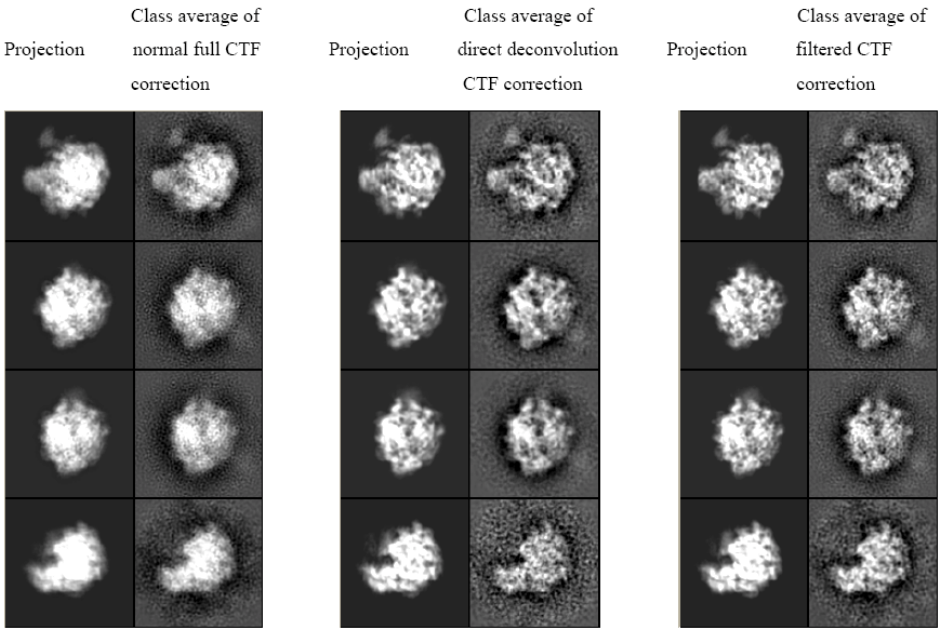

Figure 5. *Representative class average images of the complex of ribosomal 50S particle with nascent chain tRNA and Hsp15. The projections and average images are selected from the fourth round of iterative refinement (well before the conventional CTF correction algorithm blew up). Average images in the left panel are generated with the conventional full CTF correction. Average images in the middle panel are generated with "direct CTF deconvolution" algorithm. Average images in the right panel are generated with "filtered CTF correction" algorithm.*

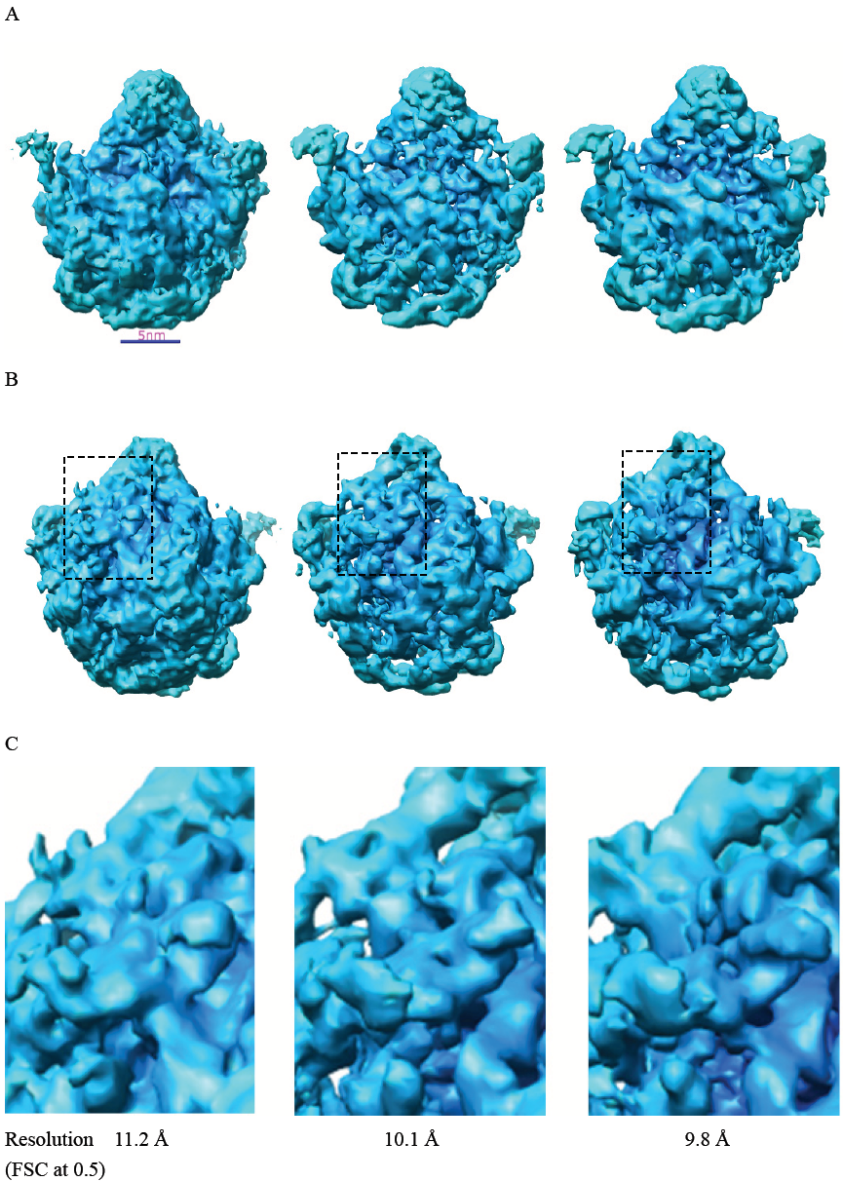

Figure 6. *3D models reconstructed with different CTF correction algorithms. Column Left, the result of conventional full CTF correction as implemented in most used reconstruction software after four iterations of refinement from a starting model. Middle & Right, the results of "direct CTF deconvolution" and "filtered CTF*

correction" algorithms after four iterations of refinement using the same starting model and the same data set as used for the left model. A) Front view of ribosomal 50S complex. B) Back view of ribosomal 50S complex. The black dash line boxes indicate representative regions. C) Views zoomed in for the indicated regions in B.

Figure 5 shows some selected, representative average images from classes having relative many particles. Comparison of the projections and class average images with the results obtained from the GroEL samples in Figure 3, show the ribosome projections to be more blurred and have less contrast. The reasons are mainly:

- The GroEL data set of 4,169 particles contains the highest contrast particles selected from the original 39,085 particles. Next they were used to reconstruct a 6 Å structure (Ludtke et al., 2004). In contrast, the data of the ribosome complex were collected with a relatively smaller defocus (near 1μm), resulting in a lower contrast and more noisy images. Better contrast of the original images used in reconstruction usually results in better contrast in the average images

- The effective number of particles used in reconstruction for the GroEL is much larger than the number used for the ribosomal subunit due to the high symmetry of GroEL, causing the SNR to be higher in the average images of GroEL.

- The asymmetric ribosome structure is more irregular, thus the projections looks less like stripes and more like blobs.

In Figure 5, the averaged images of the new algorithms (images in the middle & right columns) look better with more detail than the conventional results (images in left column). The substantial improvement in the quality of the class average images directly results in better 3D models being reconstructed, as is shown in Figure 6.

In Figure 6, the results of "filtered CTF correction" (Right model) and "direct CTF deconvolution" (Middle model) show similar fine detail. Many high resolution structural features of rRNA's double helices can be observed including, for instance,

the turns and major and minor grooves. Even the general shapes and densities of helices of the ribosomal proteins can be recognized, while the result of normal full CTF correction (left model) is generally over-corrected.

Using even-odd tests and FSC with 0.5 criterion, we calculated the resolution of each model respectively. The model obtained using the "direct CTF deconvolution" has a resolution of 10.1 Å. The model of "filtered CTF correction" has an even slight better resolution of 9.8 Å. In both cases, the resolution improved by more than 1Å compared to the conventional full CTF correction, using the same data and starting model. The differences between the results on the ribosome compared to the results of GroEL suggest it is better to use the "filtered CTF correction" algorithm when the experimental data are very noisy (e.g. images with a defocus of less than 1μm). Although the data are noisy, the algorithm stably suppresses the noise. The "filtered CTF correction" algorithm suppresses the noise more strongly, but doesn't prohibit the 3D reconstruction. On the contrary. Using only four iterative cycles, the new algorithms are capable of producing a 3D structure with a better resolution, while converging to the optimal resolution more quickly.

3.4 Discussion

The "direct CTF deconvolution" algorithm provides a novel approach to full CTF correction without using a Wiener filter. Although it is an approximation approach, in our tests it gave better results in practice than current methods. Especially when we have enough particle projections or the particles are highly symmetric, the new algorithms are probably very useful.

Our method slightly over-filters at high resolution (see Figure 2, the red curve is higher than the blue curve at high resolution, resulting in a dampening of these frequencies upon correction). One should be careful with procedures that boost high spatial frequencies, as they may lead to over-fitting.

In order to push the resolution of the final model in 3DEM reconstruction to beyond 1 nm, the user normally needs to do many iterations until the refinement has converged. This refinement step is important and represents the most time consuming step in the

reconstruction procedure. Since refinement does not always converge, the new algorithms may provide at least part of the answer to this problem.

One reason for failure of the iterative refinement is distance in conformational space between the starting reference model and the final model. The starting model normally has a resolution lower than 2 nm, the expected final model has a resolution higher than 1 nm. It would be very helpful and important to get stable intermediate-resolution (between 1 nm to 2 nm) models in the reconstruction, filling the gap between the starting model and the final high resolution model, leading the iterative reconstruction to converge to the correct density map. For these stable intermediate-resolution models, it is more important to be "correct" rather than having lots of uncertain detail, in order to avoid model bias when we are trying to push the final model towards atomic resolution.

The new filter is efficient in getting a stable intermediate-resolution model, in combination with the existing full CTF correction method (implemented and tested as the "filtered CTF correction" algorithm). In this combination, the algorithm also operates as an extra filter suppressing the noise more strongly. Although the result may have a little bit less resolution, the enhancement of the signal-to-noise ratio improves the stability of the model. For instance, in the first test of GroEL, this combined method didn't generate the highest resolution model, but it did produce a stable intermediate-resolution model: the observation of less (spurious) density in the inner channel of M3 is in line with the X-ray structure of GroEL and the higher resolution EM model, as presented in the results section. It proves that such stable model is also a "correct" model.

How much of the improvement in the model resolution is due to better alignment, and how much is due to the new CTF correction method? We cannot answer this issue unequivocally. The alignment and the CTF correction are so closely linked (a better CTF correction allows a better alignment) that we cannot separate the two. Only the first iteration, before alignment, therefore could settle this issue. The differences are so small in this case that we assume the major improvement of our method causes from improved alignment due to the alternative CTF correction.

3.5 Conclusion

A new approximation method of CTF correction has been implemented that was implemented in the EMAN package and can straightforwardly be incorporated into other 3D reconstruction software packages. It provides an alternative CTF correction method in generating class average images. The method shows better convergence and a better resolution of the final 3D structure, even in the presence of relatively high noise levels. The applied filter is continuously differentiable and does not introduce Fourier artifacts. It effectively avoids instability in regions where the CTF has zeros. The CTF correction is thus less sensitive to the zeros of CTF. When the zeros of CTF are not or cannot be estimated accurately, e.g. due to the low contrast, slightly drift or astigmatism of the micrographs, the new algorithm is expected to have higher tolerance.

The approximation inverse filter is only partially modified the inverse function. When calculating the class average image, images with different defocus will compensate each other at the zeros of the CTF in the Fourier space. It must converge to the complete CTF correction when the number of differently focused images that make up the average images increases.

Acknowledgements

We thank Wah Chiu and Steven Ludtke for the permission of using the GroEL images data. We are grateful to Dr. RAG de Graaff for revising the manuscript. The figures for showing 3D models were made by using UCSF's Chimera (Pattersen et al., 2004). This work was financially supported by the Cyttron Foundation (http://www.cyttron.org/).

References

Beckmann, R., Bubeck, D., Grassucci, R., Penczek, P., Verschoor, A., Blobel, G., Frank, J., 1997. Alignment of conduits for the nascent polypeptide chain in the Ribosome-Sec61 complex. Science 278, 2123-2126.

Braig, K., Otwinowski, Z., Hegde, R., Boisvert, D.C., Joachimiak, A., Horwich, A.L., Sigler, P.B., 1994. The crystal structure of the bacterial chaperonin GroEL at 2.8Å. Nature 371, 578-586.

Braig, K., Adams, P.D., Brunger, A.T., 1995. Conformational variability in the refined structure of the chaperonin GroEL at 2.8 Å resolution. Nat. Struct. Biol. 2, 1083-1094.

Chiu, W., Baker, M.L., Jiang, W., Dougherty, M., Schmid, M.F., 2005. Electron cryomicroscopy of biological machines at subnanometer resolution. Structure 13, 363-372.

Erickson, H.P., Klug, A. 1970. The Fourier transform of an electron micrograph: Effects of defocussing and aberrations, and implications for the use of underfocus contrast enhancement. Ber. Bunsenges. Phys. Chem. 74, 1129–1137.

Fernández, J.J., Li, S., Crowther, R.A., 2006. CTF determination and correction in electron cryotomography. Ultramicroscopy 106, 587-596.

Frank, J., Shimkin, B., Dowse, H., 1981. SPIDER-a modular software system for electron image processing. Ultramicroscopy 6, 343–358.

Frank, J., Penczek, P., 1995. On the correction of the contrast function in biological electron microscopy. Optik 98, 125–129.

Frank, J., Radermacher, M., Penczek, P., Zhu, J., Li, Y., Ladjadj, M., Leith, A., 1996. SPIDER and WEB: Processing and Visualization of Images in 3D Electron Microscopy and Related Fields. J. Structural Biol. 116, 190-199.

Frank, J., 1996. Three-Dimensional Electron Microscopy of Macromolecular Assemblies. Academic Press, San Diego.

Gonzalez, R., Woods, R., Eddins, S., 2003 *Digital Image Processing Using Matlab.* Prentice Hall

Grigorieff, N., 2007. FREALIGN: High-resolution refinement of single particle structures. J. Struct. Biol. 157, 117-125.

Hanszen, K.J., 1971. The optical transfer theory of the electron microscope: fundamental principles and applications. Adv. Opt. Elec. Microsc. (R. Barer & V.

E. Cosslett, eds.) 4, 1-84.

Hartl, F.U., 1996. Molecular chaperones in cellular protein folding. Nature 381, 571–579.

Huang, Z., Baldwin, P.R., Penczek, P.A., 2003. Automated determination of parameters describing power spectra of micrograph images in electron microscopy. J. Struct. Biol. 144, 79-94.

Jiang, W., Chiu, W., 2001. Web-based Simulation for Contrast Transfer Function and Envelope Functions. Microsc. Microanal. 7, 329-334.

Jiang, L., Schaffitzel, C., Bingel-Erlenmeyer, R., Ban, N., Korber, P., Koning, R.I., de Geus, D.C., Plaisier, J.R., Abrahams, J.P., 2008 Recycling of Aborted Ribosomal 50S Subunit-Nascent Chain-tRNA Complexes by the Heat Shock Protein Hsp15. J Mol Biol. doi:10.1016/j.jmb.2008.10.079

Liang, Y., Ke, E.Y., Zhou, Z.H., 2002. IMIRS: a high-resolution 3D reconstruction package integrated with a relational image database. J. Struct. Biol. 137, 292–304.

Ludtke, S.J., Baldwin, P.R., Chiu, W., 1999. EMAN: Semiautomated Software for High-Resolution Single-Particle Reconstructions. J. Struct. Biol. 128, 82–97.

Ludtke, S.J., Jakana, J., Song, J.-L., Chuang, D., Chiu, W., 2001. A 11.5 Å single particle reconstruction of GroEL using EMAN. J. Mol. Biol. 314, 253–262.

Ludtke, S.J., Chen, D.H., Song, J.L., Chuang, D.T., Chiu, W., 2004. Seeing GroEL at 6 Å resolution by single particle electron cryomicroscopy. Structure 12, 1129–1136.

Ludtke, S.J., Baker, M.L., Chen, D.H., Song, J.L., Chuang, D.T., Chiu, W., 2008. De novo backbone trace of GroEL from single particle electron cryomicroscopy. Structure 16(3), 441-8.

Mallick, S.P., Carragher, B., Potter, C.S., and Kriegman, D.J., 2005. ACE: automated CTF estimation. Ultramicroscopy 104, 8-29.

Marabini, R., Masegosa, I.M., San Martín, M.C., Marco, S., Fernández, J.J., de la Fraga, L.G., Vaquerizo, C., Carazo, J.M., 1996. Xmipp: An image processing package for electron microscopy. J. Struct. Biol. 116, 237–240.

Medipix: a photon counting pixel detector, http://medipix.web.cern.ch/MEDIPIX/

Penczek, P.A., Zhu, J., Schröder, R., Frank, J., 1997. Three Dimensional Reconstruction with Contrast Transfer Compensation from Defocus Series. Scanning Microscopy 11, 147-154.

Pettersen, E.F., Goddard, T.D., Huang, C.C., Couch, G.S., Greenblatt, D.M., Meng, E.C., Ferrin, T.E., 2004. UCSF Chimera - A Visualization System for Exploratory

Research and Analysis. J. Comput. Chem. 25, 1605-1612.

Plaisier, J.R., Koning, R.I., Koerten, H.K., van Roon, A.M., Thomassen, E.A.J., Kuil, M.E., Hendrix, J., Broennimann, C., Pannu, N.S., Abrahams, J.P., 2003. Area detectors in structural biology. Nuclear Instruments and Methods in Physics Research. Section A 509, 274-282.

Plaisier J.R., Jiang L., Abrahams J.P., 2007. Cyclops: New modular software suite for cryo-EM. J. Struct. Biol. 157, 19-27.

Ramachandran, G.N. & Srinivasan, R., 1970. Fourier Methods in Crystallography, pp. 60-71. New York: Wiley.

Sander, B., Golas, M.M., Stark, H., 2003. Automatic CTF correction for single particles based upon multivariate statistical analysis of individual power spectra. J. Struct. Biol. 142, 392-401.

Schiske, P., 1973. Image processing using additional statistical information about the object, in: P. Hawkes (Ed.), Image Processing and Computer-aided Design in Electron Optics, Academic Press, London, 82–90.

Sorzano, C.O.S., Marabini, R., Velázquez-Muriel, J., Bilbao-Castro, J.R., Scheres, S.H.W., Carazo, J.M., Pascual-Montano, A., 2004a. XMIPP: a new generation of an open-source image processing package for electron microscopy. J. Struct. Biol. 148, 194-204.

Sorzano, C.O.S., Marabini, R., Herman, G.T., Censor, Y., Carazo, J.M., 2004b. Transfer function restoration in 3D electron microscopy via iterative data refinement. Phys. Med. Biol. 49, 509–522.

Stagg, S.M., Lander, G.C., Quispe, J., Voss, N.R., Cheng, A., Bradlow, H., Bradlow, S., Carragher, B., Potter, C.S., 2008. A test-bed for optimizing high-resolution single particle reconstructions. J. Struct. Biol. 163, 29-39.

Thon, F., 1966. Zur defokussierungsabhängigkeit des phasenkontrastes bei der elektronen-mikroskopischen abbildung. Z. Naturforsch 21a, 476–478.

Thon, F., 1971. Phase contrast electron microscopy. Electron Microscopy in Materials Science. (Ed. U. Valdre) Academic Press, N. Y., 570-625.

van Heel, M., 1979. IMAGIC and its results. Ultramicroscopy 4, 117.

van Heel, M. Harauz, G., 1986. Resolution Criteria for 3-Dimensional Reconstruction. Optik 73, 119-122.

van Heel, M., Harauz, G., Orlova, E.V., Schmidt, R., Schatz, M., 1996. A new generation of the IMAGIC image processing system. J. Struct. Biol. 116, 17–24.

van Heel, M., Gowen, B., Matadeen, R., Orlova, E.V., Finn, R., Pape, T., Cohen, D., Stark, H., Schmidt, R., Schatz, M., Patwardhan, A., 2000. Single-particle electron cryo-microscopy: towards atomic resolution. Q Rev Biophys 33, 307-69.

van Heel, M., Schatz, M., 2005. Fourier Shell Correlation Threshold Criteria. J. Struct. Biol. 151, 250-262.

Velázquez-Muriel, J.A., Sorzano, C.O.S., Fernández, J.J., Carazo, J.M., 2003. A method for estimating the CTF in electron microscopy based on ARMA models and parameter adjusting. Ultramicroscopy 96, 17–35.

Wan, Y., Chiu, W., Zhou, Z.H., 2004. Full contrast transfer function correction in 3D cryo-EM reconstruction. International Conference on Communications, Circuits and Systems, (ICCCAS 2004), June 2004.

Zhou, Z.H., Hardt, S., Wang, B., Sherman, M.B., Jakana, J., Chiu, W., 1996. CTF determination of images of ice-embedded single particles using a graphics interface. J. Struct. Biol. 116, 216–222.

Zhou, Z.H., 2008. Towards atomic resolution structural determination by single particle cryo-electron microscopy. Curr. Opin. Struc. Biol. 18, 218-228.

Zhu, J., Penczek, P.A., Schröder, R., Frank, J., 1997. Three-dimensional reconstruction with contrast transfer function correction from energy-filtered cryoelectron micrographs: procedure and application to the 70S *Escherichia coli* ribosome. J. Struct. Biol. 118, 197–219.

Zubelli, J.P., Marabini, R., Sorzano, C.O.S., Herman, G.T., 2003. Three-dimensional reconstruction by Chahine's method from electron microscopic projections corrupted by instrumental aberrations. Inverse Probl. 19, 933–949.

Chapter 4

Reconstruction of the complexes of the ribosomal large subunit 50S with Hsp15 and t-RNA reveals the rescue mechanism of the stalled 50S

Published as: Jiang, L., Schaffitzel, C., Bingel-Erlenmeyer, R., Ban, N., Korber, P., Koning, R.I., de Geus, D.C., Plaisier, J.R., Abrahams, J.P., 2009. Recycling of aborted ribosomal 50S subunit-nascent chain-tRNA complexes by the heat shock protein Hsp15. J. Mol. Biol. 386, 1357-1367

Abstract

When heat shock prematurely dissociates a translating bacterial ribosome, its 50S subunit is prevented from reinitiating protein synthesis by tRNA covalently linked to the unfinished protein chain that remains threaded through the exit tunnel. Hsp15, a highly upregulated bacterial heat shock protein, reactivates such dead-end complexes. Here, we show with cryo-electron microscopy reconstructions and functional assays that Hsp15 translocates the tRNA moiety from the A site to the P site of stalled 50S subunits. By stabilizing the tRNA in the P site, Hsp15 indirectly frees up the A site, allowing a release factor to land there and cleave off the tRNA. Such a release factor must be stop codon independent, suggesting a possible role for a poorly characterized class of putative release factors that are upregulated by cellular stress, lack a codon recognition domain and are conserved in eukaryotes.

4.1 Introduction

Heat shock upregulates many proteins that function as chaperones or as proteases. It also increases the transcription of the small heat shock protein Hsp15, which is an RNA/DNA binding protein. It targets aborted ribosomal subunits rather than misfolded proteins (Korber *et al.*, 1999). Its ~50-fold transcriptional increase is even higher than the upshift in expression of such well-characterized heat shock proteins such as GroEL/ES, DnaK and ClpA, indicating the high relevance of Hsp15 for adapting to thermal stress (Richmond *et al.*, 1999).

Translating ribosomes can dissociate prematurely upon heat shock, resulting in 50S subunits that carry tRNA covalently attached to the nascent chain (nc-tRNA) of an incomplete protein that is threaded through the 50S exit tunnel (see also fig. 1). These 50S•nc-tRNA subunits cannot reinitiate protein synthesis, unless the tRNA and nascent chain are removed. Accumulation these blocked 50S•nc-tRNA would therefore constitute a problem for the cell. Korber *et al.* (2000) demonstrated that Hsp15 specifically binds with high affinity (K_d <5 nM) to such blocked 50S•nc-tRNA ribosomal subunits. The affinity of Hsp15 for 50S•nc-tRNA complexes is significantly higher than for empty, functional 50S subunits. However, it remained unclear how Hsp15 discriminates between active and aberrantly terminated 50S subunits and how it contributes to recycling blocked, non-functional 50S•nc-tRNA complexes.

To answer these questions, we determined the structure of the complex of the 50S•nc-tRNA subunit both in the absence and presence of Hsp15 by cryo-EM and single particle analysis to resolutions of 14 and 10 Å, respectively. The resolution was sufficiently high to fit atomic models of the individual components (50S, tRNA and Hsp15) into the EM density maps. We confirmed our results with puromycin nascent chain release assays.

We identified the binding site of Hsp15 on the large ribosomal subunit and its contacts with the P-site tRNA. The conserved αL RNA-binding domain of Hsp15 contacts helix H84 of 23S rRNA which is positioned close to the 30S/50S interface, and it lines the cleft above the P-site. The D/T loops of the P-site tRNA within the 50S•nc-tRNA•Hsp15 complex bind the positively charged C-terminal α-helix of

Hsp15. Based on these findings we suggest a mechanism for the recycling of aborted 50S subunits during heat shock.

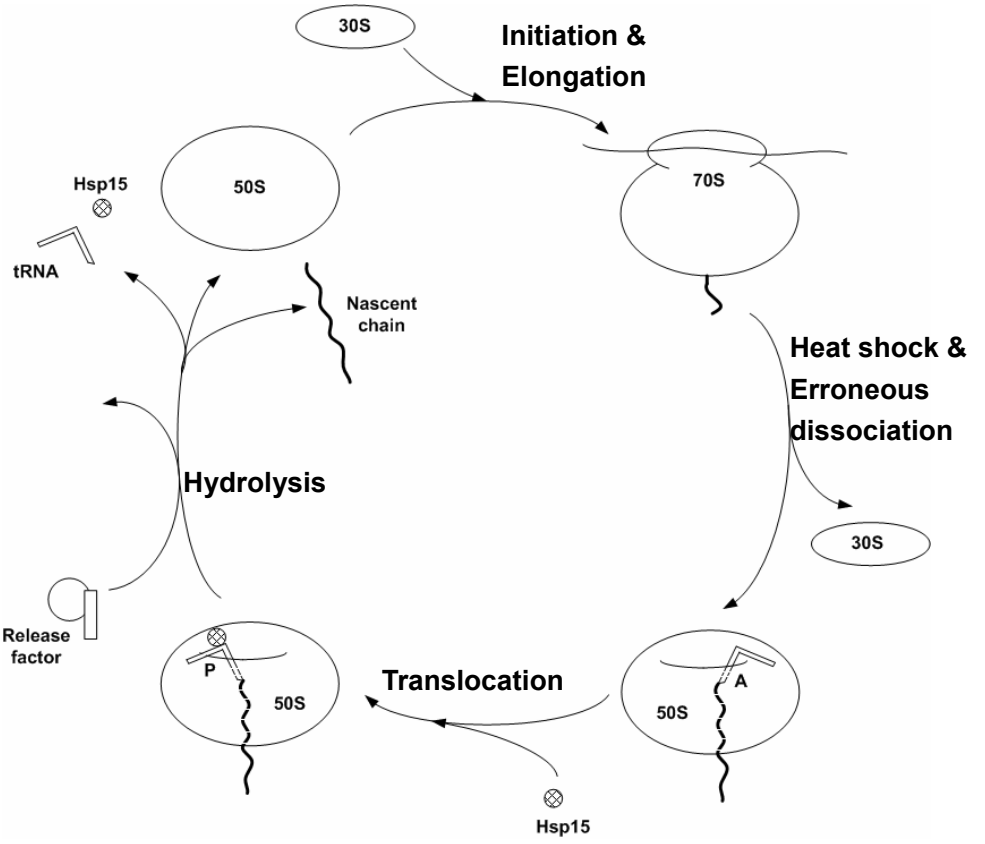

Figure 1. ***Rescue cycle of the stalled ribosomal 50S subunit****. Heat shock can erroneously dissociate a translating ribosome into a 30S subunit and a blocked 50S subunit carrying a tRNA linked to the unfinished nascent chain (upper left). Here we show that in these stalled 50S•nc-tRNA complexes, the tRNA is located at the A-site (bottom left) and that the small heat shock protein Hsp15 translocates the tRNA to the P-site (bottom right), where it can be liberated by a release factor (top right).*

4.2 Results

4.2.1 Generation of stable 50S•nc-tRNA complexes

Stable, homogenous 70S•nc-tRNA complexes were generated by *in vitro* transcription and *in vitro* translation using the plasmid pUC19Strep3FtsQSecM with an N-terminal triple Strep-tag for affinity purification (Schaffitzel & Ban, 2007). To span the ribosomal exit tunnel, the FtsQ sequence and the 17 amino acids-long SecM translational arrest motif were C-terminally fused to the affinity tag. The SecM peptide interacts tightly with the ribosomal tunnel (Nakatogawa & Ito, 2002) and thereby significantly stabilizes the 70S•nc-tRNA complexes, without the need of using chloramphenicol antibiotic. After *in vitro* translation, the translating ribosomes were loaded onto a sucrose gradient with low concentration of magnesium ions causing dissociation of the 70S•nc-tRNA complexes into 50S•nc-tRNA and 30S (Figure 2A) complexes. The 50S•nc-tRNA complexes were further purified and separated from empty 50S using a Strep-Tactin sepharose column and finally pelleted by ultracentrifugation. The complex with Hsp15 was reconstituted by adding a 20–fold molar excess of Hsp15.

Binding assays confirmed that Hsp15 neither binds 70S ribosomes nor empty 50S subunits under the assay conditions (Figure 2B). However, lower affinity binding to the empty 50S subunit was observed, when the sucrose cushion was omitted from the sedimentation assay (not shown). This is in agreement with the previously described non-specific nucleic acid binding activity of Hsp15 (Korber *et al*., 1999; 2000). Hsp15 only bound with high affinity to 50S subunits containing nc-tRNA at a 1:10 molar ratio (Figure 2B).

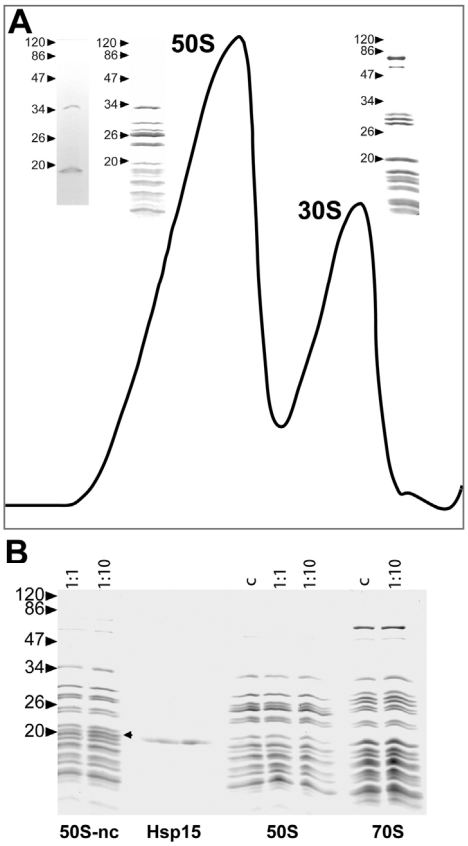

Figure 2. ***(A)*** *Preparation of 50S•nascent chain-tRNA complexes (50S-nc/50S•nc-tRNA). Sucrose gradient profile of an in vitro translation reaction in the presence of 0.3 mM $Mg(OAc)_2$. The two peaks (50S and 30S) are analyzed on a Coomassie-stained SDS gel. The presence of the nascent chain in the 50S is shown by Western blotting (left side) using Streptactin-alkaline phosphatase conjugate. The upper band at ~34 kDa corresponds to nc-tRNA, the lower band to the nascent peptide alone.* ***(B)*** *Binding assay of Hsp15. Binding of purified Hsp15 to 50S-nc, to 50S and to 70S was analyzed by ribosomal pelleting through a sucrose cushion. As a control (indicated with c), 50S and 70S was loaded alone. Hsp15 did not migrate through the sucrose cushion (not shown). Hsp15 was added in a 1:1 and 1:10 molar ratio. Hsp15 was found only in the pellet of 50S-nc as indicated with an arrow. As a positive control, 100 ng Hsp15 was loaded onto the SDS gel.*

4.2.2 Structure of the 50S•nc-tRNA Complex

In order to identify the position of Hsp15 in the ribosomal complex, we first determined the structure of the 50S subunit containing nc-tRNA in the absence of Hsp15. In two separate reconstructions, we used as starting reference models (i) the cryo-EM reconstruction of the empty 50S subunit (see supplement) and (ii) the model of the 50S-nascent chain tRNA complex that did contain Hsp15 (see below). The two reconstructions converged to a similar structure of about 14 Å resolution (50% FSC criterion). The L7/L12 stalk of the 50S subunit is not fully visible in this reconstruction. This region is responsible for binding translation factors in the actively translating ribosome and is known to be flexible and conformationally heterogeneous in isolated large ribosomal subunits (Helgstrand *et al.*, 2007). More importantly, the structure revealed clear additional density located at the A-site (Figure 3A). This density most likely corresponds to poorly ordered tRNA which is covalently attached to the nascent polypeptide extending through the ribosomal exit tunnel.

4.2.3 Structure of the 50S•nc-tRNA•Hsp15 Complex

The reconstruction of the 50S•nc-tRNA•Hsp15 complex yielded a resolution of 10 Å based on the Fourier shell correlation (Figure S2). Clear additional density which could accommodate tRNA is visible in the P-site (Figure 3B). Based on supervised classification, which was performed to sort out and remove any empty 50S particles, we concluded that the P-site was virtually fully occupied with tRNA. This confirmed our biochemical characterization of the purity of the sample (see above). The extra density in the P-site matched the atomic model of $tRNA^{Phe}$ at contouring levels suggested by other parts of the structure, indicating that the tRNA is well ordered in the 50S•nc-tRNA•Hsp15 complex. Its anticodon stem was rotated about 20^{o} about its acceptor stem towards ribosomal protein L1, compared to its location in the crystal structure of the *T. thermophilus* 70S ribosome complexed with mRNA and two tRNAs (Korostelev *et al*., 2006) (Figure 4). Since the angle between the aminoacy acceptor stem and the anticodon stem can vary in tRNAs (Moras *et al*., 1980), we refined the angle between the these stems. This resulted in a small increase ($\sim 15^{o}$), compared to the crystal structure of $tRNA^{Phe}$, thus somewhat opening up the canonical L-shaped conformation of the tRNA.

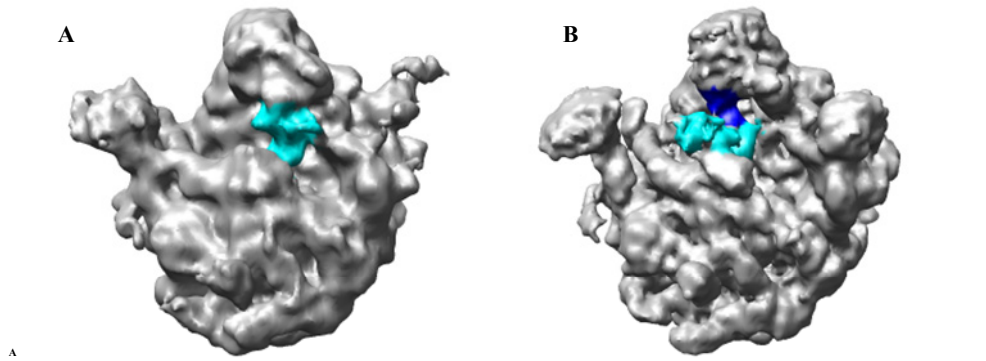

Figure 3 *Reconstructions of: (A) the 50S•nc-tRNA complex (the density of tRNA is in cyan, 14 Å resolution) and (B) the 50S•nc-tRNA•Hsp15 complex (the density of tRNA is in cyan and of Hsp15 in blue, 10 Å resolution).*

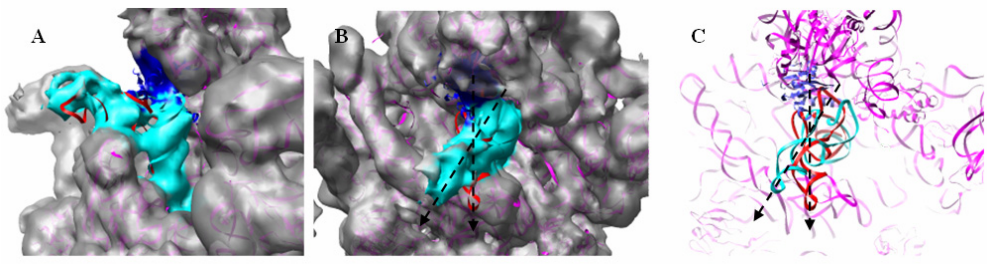

Figure 4 *Side (A) and top (B) views of the 50S subunit and tRNA of crystal structure of the T. thermophilus 70S•tRNA complex was docked into the density of the 50S•nc-tRNA•Hsp15 complex. The density corresponding to 50S is depicted in grey, tRNA density in cyan and Hsp15 density in blue. (C) as (B), without showing the density. The high-resolution structure of the 50S T. thermophilus subunit and its cognate tRNA (Korostelev et al., 2006) are shown as a purple and red ribbons, respectively. The position of the blue density indicates a 20^{o} rotation of the tRNA in the 50S•nc-tRNA•Hsp15 complex about its aminoacyl acceptor stem compared to the position of the tRNA in the 70S crystal structure. The main axes of the tRNAs are indicated by arrows.*

The location of Hsp15 was not immediately obvious. In view of the small size of Hsp15, this is not surprising: the diameter of its globular domain not much more than 15 Å (Staker *et al*., 2000). In order to locate any additional density in our reconstruction of the 50S•nc-tRNA•Hsp15 complex, we fitted the high-resolution crystal structure of the *E. coli* 50S subunit (Schuwirth *et al*., 2005) into our density using multi-rigid body fitting for the ribosomal RNA and proteins. Proteins L1, L11, L7 and L12 could not be fitted well into our density map. Most of these proteins are known to be flexible and therefore were not included in the final model. We identified well-ordered extra density close to the P-site nc-tRNA. This extra density was located between the bottom-left of the central protuberance of 50S and the elbow region of the tRNA. No known part of the 50S subunit could explain this extra density, and the tRNA could not be docked into it without gross distortions and vacating other density. At increased contour levels, corresponding to highly ordered parts of the structure, a tube-like feature in this extra density was visible. Assuming that this feature corresponded to the α-helix of Hsp15, we docked monomeric Hsp15 into the extra density and subsequently refined its position using our program LOCALFIT. The resulting atomic model is shown in Figure 5.

Hsp15 is known to have an αL RNA binding motif which it shares with ribosomal protein S4 and threonyl-tRNA synthetase, amongst others (Staker *et al*., 2000). Our docking result was confirmed by the observation that the αL RNA binding domains of Hsp15 and of S4 both interacted in the same fashion with their cognate RNA double helical targets, helix H84 of 23S rRNA and a fragment of 16S rRNA, respectively (Figure 6).

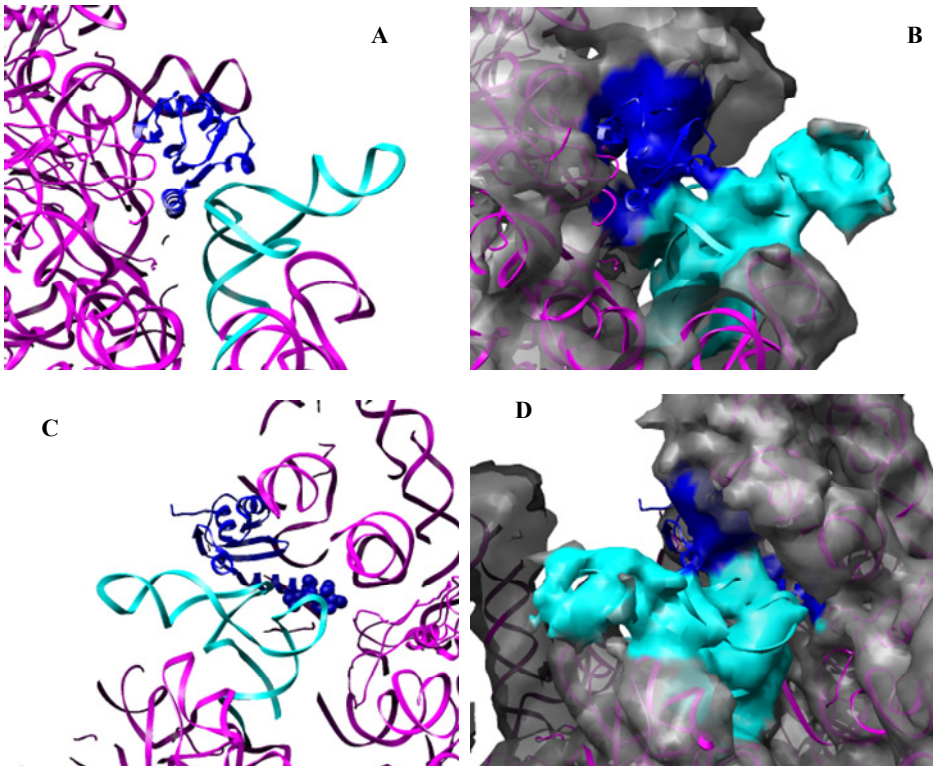

Figure 5 *Hsp15 attaches the H84 Helix of 23S rRNA and interacts with the D/T loops of the tRNA. (A) View from the left, with respect to the standard orientation of the 50S subunit (see Figure 2). The 50S subunit is depicted in magenta and the tRNA in cyan. (B) as (A), including the 50S•nc-tRNA complex density; density covering Hsp15 in blue, density covering tRNA in cyan, density covering 50S in grey. (C) The interaction of the tail of Hsp15 and tRNA, right side view, the C-terminal, positively charged α-helix of Hsp15 is show in as spheres. (D) as (C), showing density contoured at a level predicted by the molecular weight of the 50S•nc-tRNA•Hsp15 complex.*

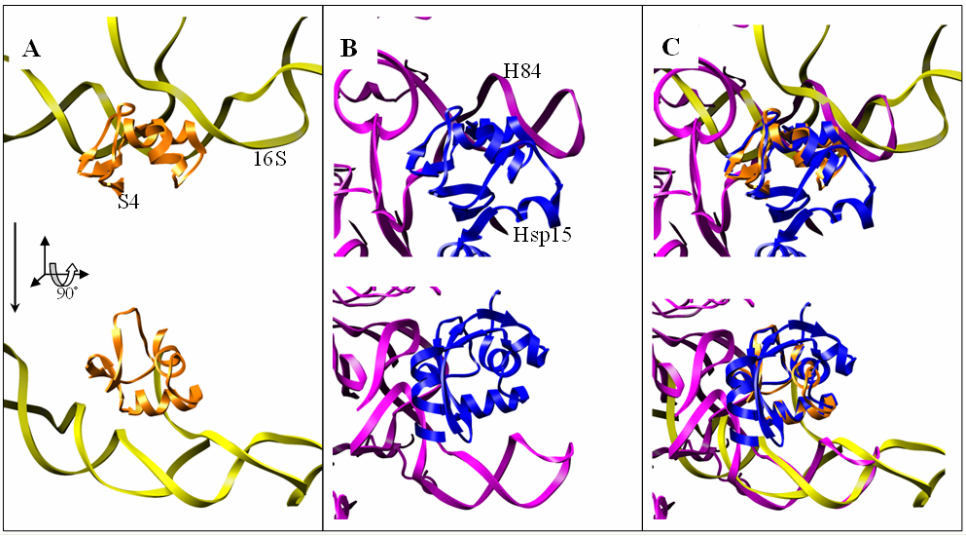

Figure 6 *Comparison of the RNA binding mode of S4 and Hsp15. (A) Top view and side view (below) of S4 interacting through its αL binding motif with its cognate 16S RNA fragment. (B) Top and side views of Hsp15 interacting through its αL binding motif with helix84 of 23S rRNA. (C) Superimposition of (A) and (B). The RNA binding motifs of Hsp15 (blue) and S4 (orange) were superimposed; the fragment of 16S RNA that is recognized by S4 is shown in yellow and fits well with 23S RNA, indicating Hsp15 and S4 bind in a similar fashion to dsRNA.*

The long C-terminal α-helix opposite the RNA-binding motif of Hsp15 and the ultimate 23 C-terminal residues (which are disordered in the crystal structure) carry a substantial number of positive charges. This C-terminal α-helix contacted the D/T loops of the nc-tRNA and, although the disordered the C-terminus could not be visualized, we observed there to be sufficient space for its positive charges to interact with the nc-tRNA and/or proximal regions of 23S rRNA.

4.2.4 Functional assay of Hsp15-induced tRNA translocation

The P site-specific antibiotic puromycin is a functional equivalent of a stop codon-independent release factor. Mimicking the 3′ end of aminoacyl tRNA at the A

site, it binds at the A site and cleaves off P-site tRNA from the nascent chain. It is used in functional assays to distinguish P-site tRNA from Asite tRNA and establish A-site occupancy. It was established that puromycin abolishes binding of Hsp15 to 50S•nc-tRNA complexes in cell extracts (Korber et al., 2000). Presumably, puromycin released the tRNA from the 50S subunit and the resulting empty 50S subunits would no longer have a high affinity for Hsp15. This observation already indicated that the tRNA must reside in the P site in the 50S•nc-tRNA•Hsp15 complex in cell extracts. Here, we show that no additional factor was involved: also, in highly purified 50S•nc-tRNA•Hsp15 samples, puromycin was able to cleave off the nascent chain (Fig. 7).

N-acetylated Phe-tRNAPhe is an nc-tRNA homolog that can freely diffuse into and out of the P site of 50S subunits, where it can react with A site-bound puromycin. This reaction proceeds optimally at 100 mM Mg^{2+} in isolated 50S subunits but is slower at lower Mg^{2+} concentrations (Wohlgemuth et al., 2006). However, for the 50S•nc-tRNA•Hsp15 complex, we found the opposite effect: raising the Mg^{2+} concentration reduced the puromycin reactivity.

The cryo-EM structure provided a straightforward explanation for this observation. At 100 mM Mg^{2+}, Hsp15 dissociates more easily from 50S•nc-tRNA complexes (Korber et al., 2000). If Hsp15 is essential for stabilizing the tRNA moiety in the P site, as suggested by the structures, then its dissociation from the 50S•nctRNA•Hsp15 complex should result in a relocation of the tRNA to the A site, where it cannot be cleaved by puromycin.

(A)

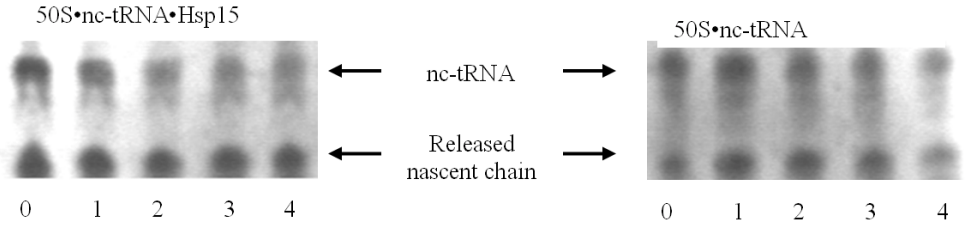

(B)

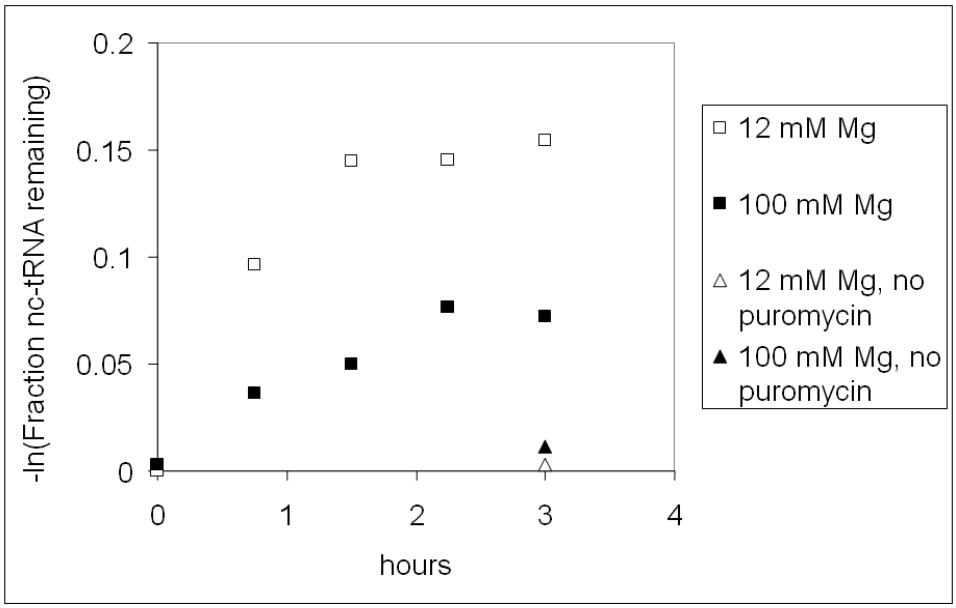

Figure 7. *(A) Puromycin reaction of 50S•nc-tRNA•Hsp15 at 37 °C in 12 mM (left) and 100 mM Mg^{2+} (right). Controls without puromycin do not show any cleavage of the ester bond between tRNA and nascent chain, even after 3 h of incubation. At the outset of the reaction, there is already a substantial amount of released nascent chain present (lower band). (B) The negative natural logarithm of the remaining nc-tRNA was plotted against the incubation time. In a first-order reaction, this is expected to be a straight line, which we indeed observed for 2–3 h after initiating the reaction. The data shown in (A) are plotted. The puromycin-induced cleavage of nc-tRNA was determined by measuring the increase of the intensity of the band corresponding to the released nascent chain as a fraction of the total intensity corresponding to the nascent chain (whether bound to tRNA or not). The higher reactivity at 12 mM Mg^{2+} can be explained by the fixation of tRNA at the P site by Hsp15 at this Mg concentration. The experiments were performed in duplicate.*

4.3 Discussion

Translational reactivation of a heat shock-aborted 50S•nc-tRNA complex requires removal of the nc-tRNA by severing of the aminoacyl ester bond between these moieties. In the cell, this hydrolysis requires the tRNA to be located in the P site and a release factor to bind at the vacant A site. In the absence of Hsp15, the tRNA moiety of nc-tRNA, although being somewhat disordered, was clearly located in the A site (Fig. 3a). The A-site location of the tRNA moiety was further corroborated by a puromycin assay (Fig. 7). At first sight, this is a surprising result, as in the complete 70S ribosome, peptidyl-tRNA has a preference for the P site. However, in the 70S complex, peptidyl-tRNA is stabilized at the P site by extensive contacts with the mRNA, 16S RNA and protein residues of the 30S subunit (e.g., Ref. Noller *et al.*, 2005), and these interactions are obviously absent in the 50S•nc-tRNA complex. On the other hand, the A-site location of the tRNA is stabilized by additional interactions with residues of the 50S subunit that lie outside the peptidyl transfer center (e.g., helix 38 of the 'A-site finger') (Stark et al., 1997). Apparently, in the absence of the 30S subunit, these interactions are strong enough to direct the tRNA moiety in the 50S·nc-tRNA complex to the A site. Our observation explains why the 50S•nc-tRNA complex cannot be recycled: a tRNA moiety in the A site prevents release factors from binding and severing the aminoacyl ester bond between the tRNA and the nascent chain.

Hsp15 located the tRNA in the P site by bridging it to helix 84 of the central protuberance of the 50S subunit, the αL RNA binding motif of Hsp15 bound to helix 84, while its positively charged C-terminal tail bound to the D/T loops of the nc-tRNA. Locked in the P site, the CCA end of the nc-tRNA is optimally positioned in the peptidyl transferase center for hydrolytic attack of its aminoacyl ester bond by a release factor. The translocation of the tRNA to the P site in the Hsp15-containing complex is in full agreement with the puromycin assay (Fig. 7) and with puromycin sensitivity of dissociated translating ribosomes in cell lysates (Korber et al., 2000). Translocation of the nc-tRNA from the A site to the P site would allow a release factor to bind in the A site. In the 70S ribosome, this translocation requires energy: EF-G hydrolyzes GTP in the process. Our results indicate that in the absence of interactions with the 30S subunit, the binding energy of the Hsp15 to the 50S·nc-tRNA complex is sufficient to induce translocation.

Our data explain why Hsp15 has a reduced affinity for translationally active 50S subunits: its binding energy is reduced because the interaction between the C-terminus of Hsp15 and the P-site tRNA is missing. Furthermore, our data also indicate why Hsp15 does not have a marked affinity for translating 70S ribosomes: the presence of the 30S subunit partially blocks access of Hsp15 to its binding site on the 50S subunit and the conformation of the tRNA interacting simultaneously with the peptidyl transferase center on the 50S subunit and the decoding center on 30S subunit would not allow it to rotate into the position necessary for Hsp15 binding as observed in the EM reconstruction of the 50S•nc-tRNA•Hsp15 complex.

Which release factor cleaves the aminoacylester bond between tRNA and nascent chain in the 50S•nc-tRNA•Hsp15 complex? All well-characterized release factors interact with translating ribosomes and mimic a tRNA molecule. They all have a stop-codon recognizing domain at one end and a GGQ peptidyl hydrolase domain at the other end, which interacts with the peptidyl transferase center of the ribosome (Baranov *et al.*, 2006; Petry *et al.*, 2005; Klaholz *et al.*, 2003; Rawat *et al*., 2003). In the blocked 50S•nc-tRNA•Hsp15 complex there is no need for a stop-codon recognizing domain. The putative 15 kD, 140 aminoacid protein with unassigned function encoded by the *yaeJ* gene in *E. coli* is a likely candidate for this role. In *E. coli yaeJ* is transcribed immediately ahead of *cutF/nplE*, a factor involved in the extracytoplasmic stress response; both apparently belong to the same stress-induced operon (Connolly *et al*., 1997). YaeJ contains the conserved GGQ peptidyl hydrolase domain, but lacks a stop-codon recognizing domain. Nevertheless, due to the presence of the GGQ motif, YaeJ is placed in the same cluster of orthologous groups as the release factors RF1 and RF2 (Baranov *et al*., 2006). Thus, YaeJ could bind to the A site of the 50S•nc-tRNA•Hsp15 complex and hydrolyze the peptidyl-tRNA ester bond without needing a stop codon recognizing domain.

Residues 10 to 112 of YaeJ have a 29% identity and 55% homology with the small human protein ICT1, a 23.6 kD protein with unknown function that becomes more highly expressed upon neoplastic transformation of colon epithelial cells (Van Belzen *et al.*, 1998). On the basis of its GGQ domain, ICT1 is classified as a putative release factor, even though, like Yae1, it lacks an anticodon recognizing domain. If Yea1 and ICT1 have homologous functions in recycling prematurely dissociated (mitochondrial) ribosomes, Hsp15 might also have a eukaryotic homologue.

In summary, we propose that Hsp15 rescues heat-induced abortive 50S subunits carrying a peptidyl tRNA by fixing the tRNA moiety to the P-site (Figure 1). This allows a (specialized) release factor to bind at the A-site and cleave the aminoacylester bond between tRNA and nascent chain, which is optimally positioned for this hydrophilic attack in the peptidyl transferase centre. The cleavage allows tRNA and nascent chain to diffuse away and the 50S particle to become translationally active again.

4.4 Materials and Methods

4.4.1 Preparation of 50S•nc-tRNA complexes

The plasmid pUC19Strep3FtsQSecM was transcribed *in vitro* and translated in a membrane-free *E. coli* cell extract as previously described (Schaffitzel & Ban, 2007). The translation mix was loaded directly onto a 38 ml sucrose gradient (10 – 50 % sucrose in 50 mM Hepes-KOH, 100 mM KOAc, 0.3 mM $Mg(OAc)_2$, pH 7.5) and centrifuged for 15 hours at 23000 rpm, 4°C in a SW32 Ti rotor (Beckman Coulter). The 50S fraction was loaded onto a 300 µl Strep-Tactin sepharose column (IBA, Göttingen Germany) equilibrated with buffer 1 (20 mM Hepes-KOH, 150 mM NH4Cl, 1 mM $Mg(OAc)_2$, 4 mM β-mercaptoethanol, pH 7.5) at 4°C, eluted with 2.5 mM desthiobiotin in buffer 2 (20 mM Hepes-KOH, 150 mM NH4Cl, 12 mM $Mg(OAc)_2$, 4 mM β-mercaptoethanol, pH 7.5) and pelleted by ultracentrifugation (3 h, 55000 rpm, 4°C, TLA-55 rotor (Beckman)). The 50S•nc-tRNA (50S-nc) pellet was dissolved in buffer 2 by gentle shaking on ice.

4.4.2 Purification of Hsp15

The plasmid pTHZ25 (Korber *et al*., 1999) was transformed in *E. coli* BL21(DE3) and the cells were cultured as described. Cells were ruptured by two passages through an EmulsiFlex-C5 homogenizer (Avestin) at 15000 psi and the lysate cleared by ultracentrifugation (1h, 18000 rpm, 4ºC, Ti70 rotor (Beckman)). The supernatant was loaded onto a Q sepharose FF column (GE Healthcare) and a phenyl-sepharose column (GE Healthcare) as described (Korber *et al*., 1999). The purified protein was dialyzed against 30 mM Hepes-KOH, 1 mM EDTA pH 7.0, concentrated with a Centriplus concentrator (MWCO 3 kDa, Amicon), flash-frozen and stored at -80 ºC.

4.4.3 Binding assays of Hsp15

15 µg 50S-nc, 50S and 70S were incubated in a 1:1 and 1:10 molar ratio with purified Hsp15 in buffer 3 (20 mM Hepes-KOH, 100 mM NH4Cl, 25 mM $Mg(OAc)_2$, pH 7.5)

on ice for 30 min. The mix was centrifuged 5 min at 14000 rpm in a table top centrifuge at 4°C and then loaded onto a 1.5 ml sucrose cushion (30% w/v sucrose in buffer 3). The ribosomes and ribosomal subunits were pelleted by ultracentrifugation (5 h, 55000 rpm, 4°C, TLA-55 rotor (Beckman)). The ribosomal pellet was quantified and loaded onto a 16% SDS gel.

4.4.4 Puromycin assay

50S•nc-tRNA •Hsp15 complex (60 nM) in buffer 2 (or buffer 2 with increased Mg^{2+} concentration to 100 mM to favor Hsp15 dissociation) was incubated with 2 mM puromycin for 3 h at 37 °C. Samples at 45-min intervals were withdrawn, mixed with an equal volume of loading buffer and separated on low-pH SDS-based Tris–acetate gel to minimize hydrolysis of the ester bond linking tRNA to the nascent chain. Immunodetection of the nascent chain was carried out on PVDF membrane using a Streptag monoclonal antibody conjugated to horseradish peroxidase (IBA). Detection was performed by electrochemiluminescence, and spots on the X-ray films were quantified densitometrically.

4.4.5 Specimen preparation and cryo-electron microscopy

For grid preparation, a 20-fold molar excess of Hsp15 was added to 150 nM 50S•nc-tRNA complexes. Glow-discharged carbon-coated lacey Formvar grids (300 mesh, Ted Pella) were loaded with 3 µl sample (approximately 150 nM of ribosomal complex). Grids were blotted and plunged into liquid ethane using a fully automated home-built environmental chamber and vitrification device operating at 100% humidity and 25ºC. Micrographs were recorded on film at a magnification of x50.000 under low-dose conditions($<10e^-/Å^2$) with a FEI Tecnai F20 electron microscope operated at 200 kV using a defocus range of 1.5 to 4.8 µm taking focal pair images. Images were recorded on Kodak SO-163 film and developed for 12 minutes in full strength KODAK D19b developer. Micrographs were scanned with a scan step of 4000 dpi on a Nikon super coolscan 9000 scanner, corresponding to a pixel size of 1.27 Å on the object scale.

4.4.6 Image Processing and 3D Reconstruction

Single particles were selected from the EM micrographs using Cyclops (Plaisier *et al.*, 2007). We also used Cyclops to create the particle sets and manage Cryo-EM micrographs. We used the unique features of Cyclops to generate masks for removing the carbon layer, large ice regions, over-crowed regions and aggregates. In order to speed up the processing, we rescaled the original photos to 1/4 size by averaging 2*2 boxes, which decreased the resolution to 2.54 Å/pixel. See Figure S1 for an example of some selected particles. We used focal pair images for reconstructing the 50S•nc-tRNA•Hsp15 and 50S•nc-tRNA complexes. Each defocus pair of micrographs was aligned by refining shift, rotation and scaling parameters, prior to selecting the particles. Using Cyclops, we selected particles in the far-from-focus micrographs and mapped the coordinates to the corresponding close-to-focus micrographs. Obvious noise and ice images were filtered from the model-based auto-selected images using Cyclops. Before reconstruction, we merged the large defocus and close-to-focus images.

The particle projections were limited to 128 * 128 pixels, covering 325 * 325 $Å^2$. Except for the reconstruction of the free 50S subunit, the defocus was corrected with the CTFIT program of EMAN (Ludtke *et al*., 1999). For free 50S subunit, no CTF correction was applied, all the images were low-pass filtered at the first zero crossing of the CTF, and no starting model was used. The first 3D model of 50S was reconstructed with the startAny program of EMAN (Ludtke *et al*., 1999) from a set of class averages, using cross common lines.

The reconstruction of the complex converged only slowly, because of the low signal-to-noise ratio resulting from the low-dose conditions. In order to speed up convergence, we used our cryo-EM structure of the 50S subunit with a resolution of 22 Å as a starting model for the reconstruction of the two 50S-nascent chain-tRNA complexes. Statistics of the reconstructions are given in Table **I**. We examined the uniformity of the ribosomal complexes present in the sample by re-analyzing the data using supervised classification. As starting models, we used empty 50S and 50S•nc-tRNA. The vast majority (>80%) of ribosomal complexes correlated best with the 50S•nc-tRNA starting model, indicating the sample was essentially uniform.

Table I. Statistics of the three-dimensional reconstructions

	50S	50S•nc-tRNA	50S•nc-tRNA•Hsp15
Numbers of particles picked	8,681	10,731 (defocus pairs)	33,922 (defocus pairs)
Particles used in the final 3D reconstruction	92%	84%	85%
Resolution(0.5 FSC[a])	22 Å	14 Å	10 Å
Numbers of micrographs	37	42	112
Defocus range(-μm)	2.5-3.5	1.5-4.1	0.6-3.5

[a]FSC: Fourier shell correlation.

4.4.7 Fitting X-Ray structures into the EM density maps / generation of an atomic model

We used the Colores subroutine of SITUS (Wriggers *et al*, 1999) to fit the high resolution model of the 50S subunit of the 70S *E. coli* ribosome (Schuwirth *et al*., 2005) into our EM density. Subsequently, we segmented the 50S model and fitted the segments in the density map using multi-rigid body refinement. For this purpose we used our program LOCALFIT, which is a 6D searching tool in Fourier space within which the translation and rotation ranges can be limited to ensure that the relative topology of the fragments is maintained. We started with a few segments, checking intermediate results, and ultimately fitted 57 separate rigid fragments: 23S RNA was segmented into 29 fragments (based on the secondary structure), 5S RNA was segmented into 2 fragments and every ribosomal protein was treated as a single rigid body.

Difference maps were generated by subtracting the fitted density of 50S subunit form the EM maps. To fit tRNA and Hsp15 in the difference map, we first placed the tRNA and Hsp15 manually and then improved them respectively as rigid bodies with

LOCALFIT. We use the atomic model of $tRNA^{Phe}$, as there is no structure known of $tRNA^{Gly}$, the tRNA present in the 50S complex. The fit of the tRNA could be slightly improved by segmenting it into two fragments. Different types of tRNA can have different angles between the anticodon and D arm and the arm containing the acceptor stem and TΨC stem (Moras *et al*., 1980).

Accession codes

The three-dimensional EM maps of the 50S•nc-tRNA•Hsp15 and 50S•nc-tRNA complexes were deposited in the European Bioinformatics Institute Macromolecular Structure Database with accession codes EMD-1456 and EMD-1455, respectively. The fitted atomic structures of 50S•nc-tRNA•Hsp15 were deposited in the Research Collaboratory for Structural Bioinformatics Protein Data Bank with IDs 3BBX(50S), 3BBV(P-site tRNA) and 3BBU(Hsp15).

Acknowledgements

This work was in part supported by Cyttron (www.cyttron.org) and by the Swiss National Science Foundation (SNSF) and the National Center of Excellence in Research (NCCR) Structural Biology program of the SNSF to NB. We would like to thank Sascha Gutmann for Hsp15 purification, Ronald Limpens for doing part of the image acquisition and Daniel Boehringer for critically reading the manuscript.

Supplement

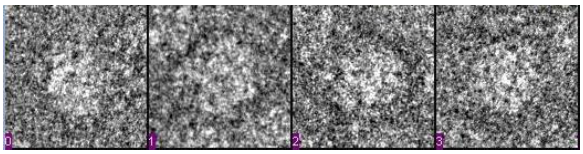

Figure S1

Particles of the 50S•tRNA•Hsp15 complex selected from the Cryo-EM micrographs. size 120*120 pixels, 2.54Å/pixel, defocus -2.5µm

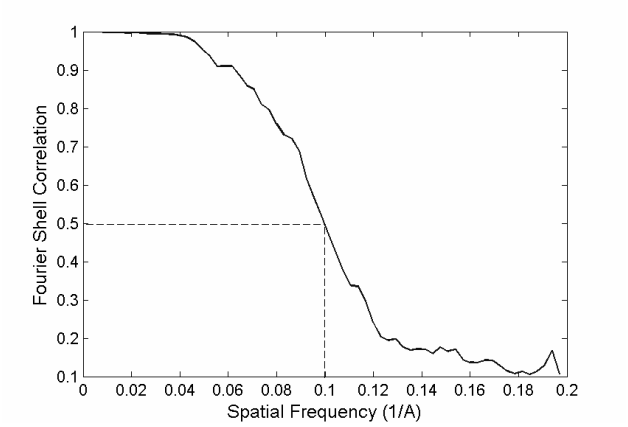

Figure S2

Fourier shell correlation of the even/odd test of the last iterative refinement reconstruction of the complex of 50S.tRNA.Hsp15.

50S Ribosomal Complex

The reconstruction of the free 50S ribosomal large subunit had a resolution of 22 Å, based on the 50% FSC criterion. The resolution is relatively low because only 8681 particles from 37 micrographs were used and because we did not collect defocus pairs. It conforms to the known global shape of the 50S particle (Matadeen *et al.*, 1999).

References

Baranov PV, Vestergaar B, Hamelryk T, Gesteland RF, Nyborg J, Atkins JF (2006). Diverse bacterial genomes encode an operon of two genes, one of which is an unusual class-I release factor that potentially recognizes atypical mRNA signals other than normal stop codons. *Biology Direct* 1, 28.

Brehmer D, Gassler C, Rist W, Mayer MP, Bukau B (2004). Influence of GrpE on DnaK-substrate interactions. *J. Biol. Chem.* 279, 27957-27964.M

Connolly L, Penas AD, Alba BM, Gross CA (1997). The response to exoplasmatic stress in *Escherichia coli* is controlled by partially over-lapping pathways. *Genes Dev.* 11, 2012-2021.

El-Samad H, Kurata H, Doyle JC, Gross CA, Khammash M (2005). Surviving heat shock: control strategies for robustness and performance. *Proc Natl Acad Sci USA* 102, 2736–2741.

Helgstrand M, Mandava CS, Mulder FAA, Liljas A, Sanyal S, Akke M (2007). The ribosomal stalk binds to translation factors IF2, EF-Tu, EF-G and RF3 via a conserved region of the L12 C-terminal domain. *J. Mol. Biol.* 365, 468-479.

Klaholz BP, Pape T, Zavialov AV, Myasnikov AG, Orlova EV, Vestergaard B, Ehrenberg M, van Heel M (2003). Structure of the Escherichia coli ribosomal termination complex with release factor 2. *Nature* 421, 90-94.

Korber P, Zander T, Herschlag D, Bardwell JCA (1999). A new heat shock protein that binds nucleic acids. *J. Biol. Chem.* 274, 249-256.

Korber P, Stahl JM, Nierhaus KH, Bardwell JCA (2000). Hsp 15: a ribosome-associated heat shock protein. *EMBO J.* 19, 741-748.

Korostelev A, Trakhanov S, Laurberg M, Noller HF (2006). Crystal structure of a 70S ribosome-tRNA complex reveals functional interactions and rearrangements. *Cell* 136, 1065-1077.

Ludtke SJ, Baldwin PR, Chiu W (1999). EMAN: Semiautomated software for high-resolution single-particle reconstructions. *J. Struct. Biol.* 128, 82-97.

Maier T, Ferbitz L, Deuerling E, Ban N (2005). A cradle for new proteins: trigger factor at the ribosome. *Curr. Op. Struct. Biol.* 15, 204-212.

Matadeen R, Patwardhan A, Gowen B, Orlova EV, Pape T, Cuff M, Mueller F, Brimacombe R, van Heel M (1999). The Escherichia coli large ribosomal subunit

at 7.5 angstrom resolution. *Structure* 7, 1575-1583.

Moras D, Comarmond MB, Fischer J, Weiss R, Thierry JC, Ebel JP, Giegé R (1980). Crystal structure of yeast tRNAAsp. *Nature* 288, 669-674.

Nakatogawa H & Ito K (2002). The ribosomal exit tunnel functions as a discriminating gate. *Cell* 108, 629-636.

Noller HF, Hoang L, Fredrick K (2005). The 30S ribosomal P site: a function of 16S rRNA. *FEBS Lett.* 579, 855–858.

Petry S, Brodersen DE, Murphy FV, Dunham CM, Selmer M, Tarry MJ, Kelley AC, Ramakrishnan V (2005). Crystal structures of the ribosome in complex with release factors RF1 and RF2 bound to a cognate stop codon. *Cell* 123, 1255-1266.

Pettersen EF, Goddard TD, Huang CC, Couch GS, Greenblatt DM, Meng EC, Ferrin TE (2004). UCSF Chimera - A Visualization System for Exploratory Research and Analysis. *J. Comput. Chem.* 25(13), 1605-1612.

Plaisier JR, Jiang L, Abrahams JP (2007). Cyclops: New modular software suite for cryo-EM. *J. Struct. Biol.* 157, 19-27.

Rawat UBS, Zavialov AV, Sengupta J, Valle M, Grassucci RA, Linde J, Vestergaard B, Ehrenberg M, Frank J (2003). A cryo-electron microscopic study of ribosome-bound termination factor RF2. *Nature* 421, 87-90.

Richmond CS, Glasner JD, Mau R, Jin H, Blattner FR (1999). Genome-wide expression profiling in Escherichia coli K-12. *Nucleic Acids Res.*, 27, 3821-3835.

Schaffitzel C & Ban N (2007). Generation of ribosome nascent chain complexes for structural and functional studies. *J. Struct. Biol.* 158, 463-471.

Schlünzen F, Zarivach R, Harms J, Bashan A, Tocilj A, Albrecht R, Yonath A, Franceschi F (2001). Structural basis for the interaction of antibiotics with the peptidyl transferase centre in eubacteria. *Nature* 413, 814-821.

Schmitt E, Mechulam Y, Fromant M, Plateau P, Blanquet S (1997). Crystal structure at 1.2 Å resolution and active site mapping of Escherichia coli peptidyl-tRNA hydrolase. *EMBO J.* 16, 4760–4769.

Schuwirth BS, Borovinskaya MA, Hau CW, Zhang W, Vila-Sanjurjo A, Holton JM, Cate JHD (2005). Structures of the bacterial ribosome at 3.5 angstrom resolution. *Science* 310, 827-834.

Staker BL, Korber P, Bardwell JCA, Saper MA (2000). Structure of Hsp15 reveals a novel RNA-binding motif. *EMBO J.* 19, 749-757.

Stark H, Orlova EV, Rinke-Appel J, Junke N, Mueller F, Rodnina M (1997).

Arrangement of tRNAs in pre- and posttranslocational ribosomes revealed by electron cryomicroscopy. *Cell* 88, 19–28.

van Belzen N, Dinjens WNM, Eussen BHJ, Bosman FT (1998). Expression of differentiation-related genes in colorectal cancer: possible implications for prognosis. *Histology and Histopathology* 13, 1233-1242.

Wilson KS, Ito K, Noller HF, Nakamura Y (2000). Functional sites of interaction between release factor RF1 and the ribosome. *Nature Struct. Biol.* 7, 866-870.

Wohlgemuth I, Beringer M, Rodnina MV (2006). Rapid peptide bond formation on isolated 50S ribosomal subunits. *EMBO Rep.* 7, 699–703.

Wriggers W, Milligan RA, McCammon JA (1999). Situs: A Package for Docking Crystal Structures into Low-Resolution Maps from Electron Microscopy. *J. Struct. Biol.* 133, 185-195.

Chapter 5

Unit-cell determination from randomly oriented electron diffraction patterns

Published as: Jiang, L., Georgieva, D., Zandbergen, H.W., Abrahams, J.P., 2009. Unit-cell determination from randomly oriented electron diffraction patterns. Acta Cryst. D. 65, 625-632.

Abstract

Unit-cell determination is the first step towards the structure solution of an unknown crystal form. Standard procedures for unit cell determination cannot cope with collections that consist of single diffraction patterns of multiple crystals, each with an unknown orientation. However, for beam sensitive nano-crystals, such is often the only data that can be obtained. An algorithm for unit cell determination that uses randomly oriented electron diffraction patterns with unknown angular relationship is presented here. The algorithm determined unit cells of mineral, pharmaceutical and protein nano-crystals in orthorhombic high and low symmetry space groups, allowing (well oriented) patterns to be indexed.

5.1 Introduction

Elastic diffraction provides the information for atomic structure determination. However, the majority of electrons or X-rays impinging on a sample scatter inelastically, and these inelastically scattered quanta induce radiation damage. Relative to the total elastic diffraction, high energy (300 keV) electrons deposit approximately 1000 times less energy in thin biological samples than X-rays and hence induce less radiation damage after normalising for the elastically diffracted quanta. In theory, electrons should therefore be more suited for structure determination if radiation damage is the limiting factor (Henderson, 1995). However, practical problems in data collection and data processing prevent the use of electrons for 3D crystallographic structure determination of organic molecules like proteins and pharmaceuticals. Here we address one of these practical problems: determining an unknown unit cell from random diffraction patterns.

In electron crystallography the unit cell is determined from electron diffraction tilt series. For this purpose 3D diffraction data are collected by tilting a crystal about a selected crystallographic axis and recording a set of oriented diffraction patterns (a tilt series) at various – preferably main – crystallographic zones. Vainshtein (Vainshtein, 1964) proposed a simple 2D lattice reconstruction methods based on tilt series, where the d* values for the non-tilt axis were plotted against the tilt angle.

Recently, a method of cell parameter determination based on a tomography tilt series of diffraction patterns was presented (Kolb *et al.,* 2008).

A different algorithm is implemented in the programme TRICE (Zou *et al.*, 2004), which determines the unit cell in two steps. First, the position and the intensities of each diffraction reflection in the individual electron diffraction patterns from the tilt series are determined and refined. For the purpose any three reflections that do not lie in the same line are selected and are assigned a 2D index, assuming a primitive cell. Then, the positions of diffraction spots and the angles between the diffraction patterns are used to identify the shortest 3D vectors, defining the unit cell parameters and the crystal orientation. The angle θ between two electron diffraction patterns of a single crystal, oriented with a double-tilt holder at the angles (α_1, β_1) and (α_2, β_2), is given by:

$\theta = \cos^{-1} (\cos \alpha_1 \cos \beta_1 \cos \alpha_2 \cos \beta_2 + \cos \alpha_1 \sin \beta_1 \cos \alpha_2 \sin \beta_2 + \sin \alpha_1 \sin \alpha_2)$.

The concept of the Niggli cell and the cell reduction technique are well established algorithms in electron crystallography. A crystal lattice can be characterized by the choice of "reduced" cell. There are 44 primitive reduced (Niggli) cells corresponding to 14 Bravais lattices. The determination of the unit cell is done by first determining the reduced direct primitive cell and then transforming it to a conventional cell. The recognition and interpretation of the reduced form are often difficult and aggravated by errors in the cell parameters or rounding errors in calculations. Thus, procedures aimed at reducing these errors need to be performed. An approach suggested by Clegg *et al*., 1981 to minimize the errors, implies the generation of a list of lattice vectors sorted on length, together with angles between pairs of them. Besides the conventional algorithms, Grosse-Kunstleve and co-workers (Grosse-Kunstleve *et. al.*, 2004) implemented two numerically stable algorithms to generate the reduced cell.

However, all these methods require the collection of at least two diffraction patterns of one single crystal, each collected at precisely known angles. This is not always possible. For instance, in the case of 3D organic crystals of proteins and pharmaceuticals, the high beam sensitivity of the materials often does not allow collecting a tilts series from a single nano-crystal. So far this limits the application of electron diffraction for studying beam-sensitive molecules.

Here, we present an algorithm for unit cell determination from randomly oriented electron diffraction patterns of different, but similar crystals. These diffraction patterns may be noisy, their centre may be poorly defined and their low resolution reflections (which are of prime importance for cell determination) may be obscured by a beam stop or be outshone by the central beam. To deal with these problems, we first calculate the autocorrelation pattern of the diffractograms. Because of the low curvature of the Ewald sphere, the spots of the diffractogram overlap with all spots of the autocorrelation pattern (but not *vice versa*, see also fig. 1). Furthermore, autocorrelation patterns have an inversion centre, whereas the beam centre of a diffractogram may be unknown. Identifying the peak positions in the autocorrelation pattern is similar to the approach taken by the indexing program Refix (Kabsch, 1993), which calculates the low resolution spacings between observed spots.

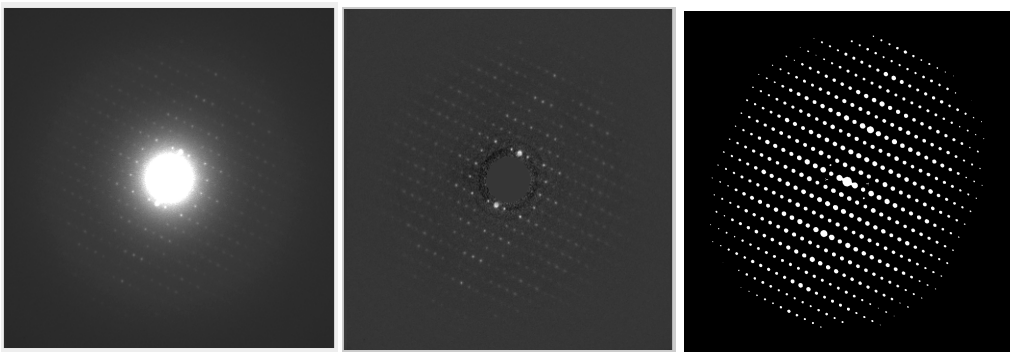

(A) (B) (C)

Figure 1 *(A) Electron diffraction pattern of lysozyme (electron energy 300 keV). (B) Diffraction pattern after removing the central beam and subtracting the radial background (C) Auto-correlation pattern of B. The diffractogram in Figure 1(A) shows a regular, point symmetrical pattern. The flatness of the Ewald sphere (the wavelength of 300 keV electrons is approximately 0.019 Å) causes this regularity.*

The low resolution peaks in the autocorrelation pattern form a 2D lattice (fig. 1), which is defined by a pair of independent vectors. From this vector pair we construct a facet, which is characterised by three numbers: the lengths of both basis vectors and the angle between them. A facet is a rotation invariant feature of a 2D lattice. Each planar intersection of a 3D lattice along a principal zone also generates a 2D lattice and hence defines a corresponding facet. Our algorithm is based on matching the observed crystal facets to model facets extracted from a simulated 3D lattice. Briefly, our procedure involves the following steps (see also fig. 2):

1. for each observed electron diffraction pattern we determine its crystal facet by:

    a. removing the central beam and overall background of the image;

    b. calculating the autocorrelation pattern of each corrected diffraction pattern;

    c. identifying the principal facet of the autocorrelation pattern and adding it to *list1*;

2. for each potential unit cell we determine its fit to the experimental data by:

    a. calculating all unique low resolution model facets that can be extracted from the corresponding simulated 3D lattice and storing these in *list2*;

    b. for each crystal facet of *list1*, selecting the best matching model facet from *list2*, calculating a residual and accumulating the residuals;

3. finally, we select the potential unit cell with the lowest accumulated residual.

The algorithm was tested with electron diffraction data from random orientations of protein (lysozyme), organic (potassium penicillin G and sodium oxacillin) and inorganic (mayenite) nano-crystals.

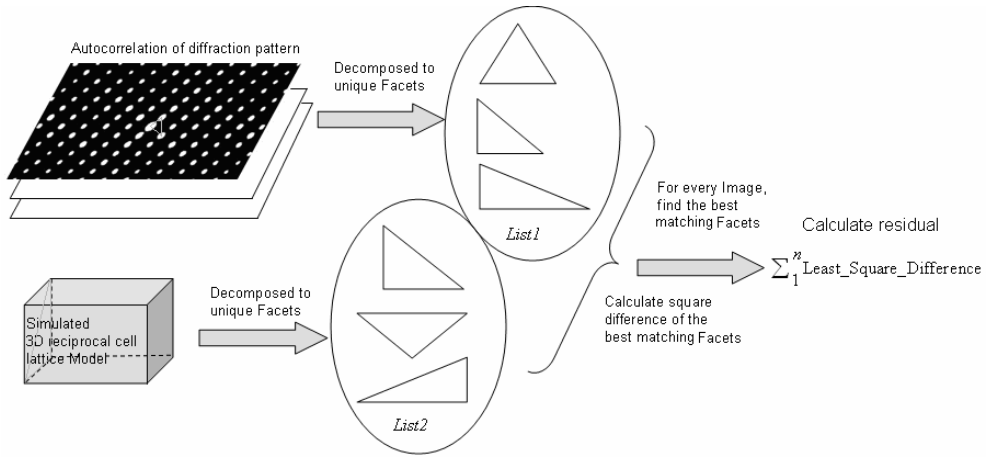
Autocorrelation of diffraction pattern
Decomposed to unique Facets
List1
For every Image, find the best matching Facets
Calculate residual
$\sum_1^n$ Least_Square_Difference
Calculate square difference of the best matching Facets
Simulated 3D reciprocal cell lattice Model
Decomposed to unique Facets
List2

Figure 2 *For a given unit cell, a 3D reflection lattice can be calculated. For each characteristic facet from the experimental diffraction pattern, the corresponding facet in the 3D reflection lattice which fits best is identified. The squared distance differences between calculated and experimentally found facets are accumulated in a penalty function.*

5.2 Methods

5.2.1 Data collection

Potassium penicillin G and sodium oxacillin were available as white crystalline powders. To obtain thin crystals suitable for EM studies, the powder was crushed in a mortar. A small amount of the sample was placed on a 300-mesh holey carbon electron-microscopy grid. Crystals suitable for electron diffraction studies (in terms of size, thickness and crystallinity) were selected. Diffraction experiments were performed at cryogenic conditions to increase the stability of the sample in the beam. Diffraction patterns were collected from randomly oriented crystals with a CM30T LaB6 microscope operating at 300keV in microdiffraction mode. A condenser aperture (C2) of 30μm and spot size 8 were used (the diameter of the beam on the crystal was approximatelly 1 μm). The data were recorded at a camera length of 420mm on DITABIS image plates and digitalized at a resolution of 0.025 millimetres per pixel with the DITABIS Micron Imaging plate read-out system.

5.2.2 Data pre-processing and determining the crystal facets

First, the digitized diffraction patterns were processed. The approximate centre of the diffraction patterns was found, the central beam or backstop shadow was removed, the resolution-dependent background was subtracted, the autocorrelation patterns were determined and the beam centre was refined. Peak positions were automatically extracted from the autocorrelation patterns, using the automated particle picking tool of the Cyclops software suite (Plaisier et al., 2007). At low resolution, the peak positions of the diffractogram coincide with those of the autocorrelation pattern (see fig. 1). From these peak positions, we calculated a low resolution facet for each diffraction pattern and stored these in *list1*.

In the absence of a beam stop, the centre of a diffraction pattern was found by a search for the most intense connected spot, using an adaptation of a standard peak search. When a beam stop occluded the direct beam, the centre was located by cross-correlating the autocorrelation pattern of the diffractogram with the diffractogram

itself, and by making use of the point symmetry of the low resolution reflections (the point symmetry is caused by the low curvature of the Ewald sphere).

The crystal facet describing the lattice of the autocorrelation pattern was determined by locating the two peaks close to the centre, ensuring that the angle they defined together with the centre was between $\pi/2$ and $\pi/3$. These two peaks can be located interactively or automatically in our algorithm. Visual inspection ensured that the facet indeed correlated to the 2D lattice of the autocorrelation pattern, and that it did not correspond to low resolution noise peaks.

5.2.3 Simulating a 3D reflection lattice and extracting low resolution model facets

Six cell parameters (axes a, b, c and angles α, β and γ) define a primitive cell. Using these 6 parameters, a systematic set of possible unit cells can be simulated in a grid search of axes and angles. Good guesses for the dimensions of the parameters and the step size can be made on the basis of the observed spacings and angles in the experimentally determined crystal facets, but we also allow the user to select the search range and step size.

From a set of cell parameters, a reciprocal cell matrix **C** can be constructed. The crystal orientation can be defined by a rotation matrix **R** and from these matrices **R** and **C**, a matrix **M** = **CR** is constructed. The position of any reflection point p of the 3D reflection lattice in Fourier space for a given unit cell and crystal orientation can be calculated using the equation:

$$p = h\mathbf{M} \qquad (1)$$

Here h = (h, k, l) is an index vector containing the integral indices of p. **M** is defined by the unit cell parameters and the crystal orientation. The indices that satisfy 'p' for a chosen resolution range can be found by imposing the boundary conditions:

$$1/d_{min} \geqslant |p| \geqslant 1/d_{max} \qquad (2)$$

Where d_{min} is the lower boundary of the resolution range and d_{max} the upper boundary resolution. Given these equations and boundary conditions, we implemented an algorithm to quickly generate all possible positions of reflection spots in 3D Fourier space. From this collection of simulated 3D spot positions, we generated a list of all unique model facets, *i.e.* model facets differing from all other by less than a specified tolerance.

5.2.4 Calculating residuals

In the ideal case, all facets from the experimental data exactly match the facets of one specific model unit cell. In practice, however, limited accuracy of determining centroids of autocorrelation peaks, small variations in unit cell parameters of different crystals and the uncertainty of the crystal orientation prevent such ideal fits. Therefore, function approximation needs to be performed, in which a function is selected that matches a target function as closely as possible.

The "squared difference function" is used to calculate the least square error of fitting two facets. If we assume that p_0 and p_1 define the 2D vector pair of the observed facet and q_0 and q_1 define the simulated facet, then the square error is defined as:

$$r = | p_0 - q_0\mathbf{R}|^2 + | p_1 - q_1\mathbf{R}|^2 \qquad (3)$$

Where **R** is the rotation matrix that minimises ‘r’. This function can be solved analytically for **R**, thus speeding up its computation. In order to improve accuracy, but at the expense of computational speed, multiple vectors of the autocorrelation image can also be matched.

However, it is not sufficient to accumulate the residual defined in (3) for all observed facets. We need to take into account that by choosing an arbitrarily large unit cell (resulting in a very dense modelled reciprocal lattice) this residual can be decreased at will. We tested several weighting schemes and found that the one which most consistently produces good unit cells is:

$$r = | p_0 - q_0\mathbf{R}|^2 * |h_{q0}|^2 + | p_1 - q_1\mathbf{R}|^2 * |h_{q1}|^2 \quad (4)$$

Where the weighting factors h_{q0} and h_{q1} are the integral indices vectors (h, k, l) of q_0 and q_1 of simulated facet. For instance, the indices of q_0 and q_1 of a facet might be {[0, 1, 1], [1, 0, 0]}, in which case $|h_{q0}|^2$ would be 2 and $|h_{q1}|^2$ would be 1. If a simulated dense lattice is N times oversampling the observed lattice, the r value in (3) is statistically $1/N^2$ smaller, whereas the length of the indices vectors of fitted facet is N times bigger, so the weighting factor of the square of indices length in (4) corrects the over-fitting problem of oversampling.

5.3 Results

5.3.1 Unit cell determination of mayenite from electron diffraction data

The algorithm was tested on randomly oriented electron diffraction data from mayenite ($Ca_{12}Al_{14}O_{33}$), a cubic inorganic mineral (fig. 3). Our algorithm suggested a cell parameter of 11.9 Å, which is in line with a reported value from literature of 11.98 Å (Boysen *et al.,* 2007). We could index the diffraction patterns of certain zones satisfactory (fig.3), with RMSD's between observed and predicted spot positions of about 0.5%. We considered data from 8 diffractograms in this analysis. In order to test the accuracy of our method and the potential for false minima, we performed a fine grid search (fig. 3B). Here we found a broader second minimum around 17 Å. This is within a few percent a factor √2 times larger than the known unit cell of about 12 Å, and hence represents an oversampling of exactly the same lattice.

(A)

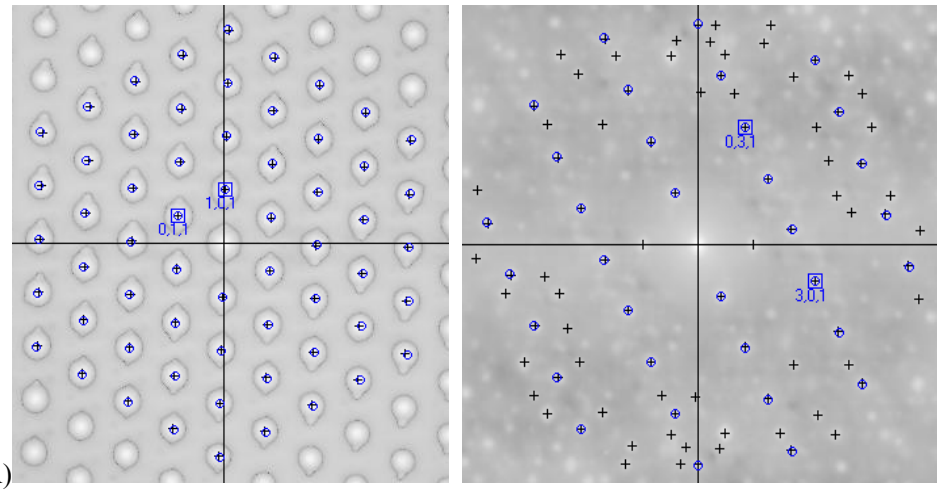

(B)

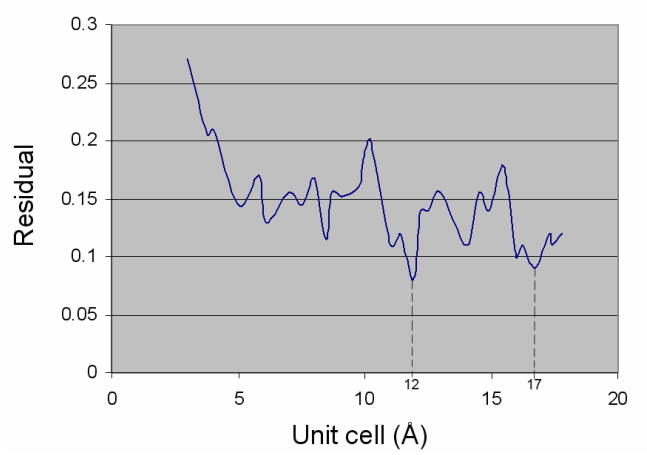

Figure 3 *(A) Examples of autocorrelation patterns from experimental electron diffractograms of mayenite. Crosses indicate the centroids of the peaks of the autocorrelation image used for the calculation and circles indicate the peak positions of the simulated diffraction pattern. The extra peaks in the second autocorrelation pattern were caused by low intensity extra lattices in the original diffractogram (not shown). (B) Fine grid search of the unit cell (based on 8 images). The 'Residual' value on the horizontal axis is defined as the square root of the average weighted residual in equation (4).*

5.3.2 Unit cell determination of potassium penicillin G and sodium oxacillin from electron diffraction data

Table 1 *Unit cell parameters of potassium penicillin G determined by single crystal X-ray diffraction and electron diffraction of single nano-crystals from a powder sample using our algorithm.*

Sample	Method	a (Å)	b (Å)	c (Å)	(α, β, γ)
Potassium penicillin G	X-ray diffraction (literature)	6.342	9.303	30.015	3x90°
Potassium penicillin G	Electron diffraction	6.4	9.3	31	3x90°
Sodium oxacillin	X-ray diffraction (literature)	7.342	10.303	26.7	3x90°
Sodium oxacillin	Electron diffraction	7.3	10.1	27	3x90°

Electron diffraction data of potassium penicillin G ($C_{16}H_{17}KN_2O_4S$) and sodium oxacillin ($C_{19}H_{18}N_3NaO_5S.H_2O$) were analysed using our new algorithm. The unit cell parameters that our algorithm suggested are given in table 1, together with X-ray diffraction data taken from literature (Dexter *et al*., 1978; Gibon *et al*., 1988 On the basis of these unit cells, we could index two main zones (001) and (011) in the case of potassium penicillin G using the program PhIDO (Phase identification and indexing from ED patterns, 2001)(see fig. 4).We considered data from 13 diffractograms for potassium penicillin G and 11 for sodium oxacillin in the analysis.

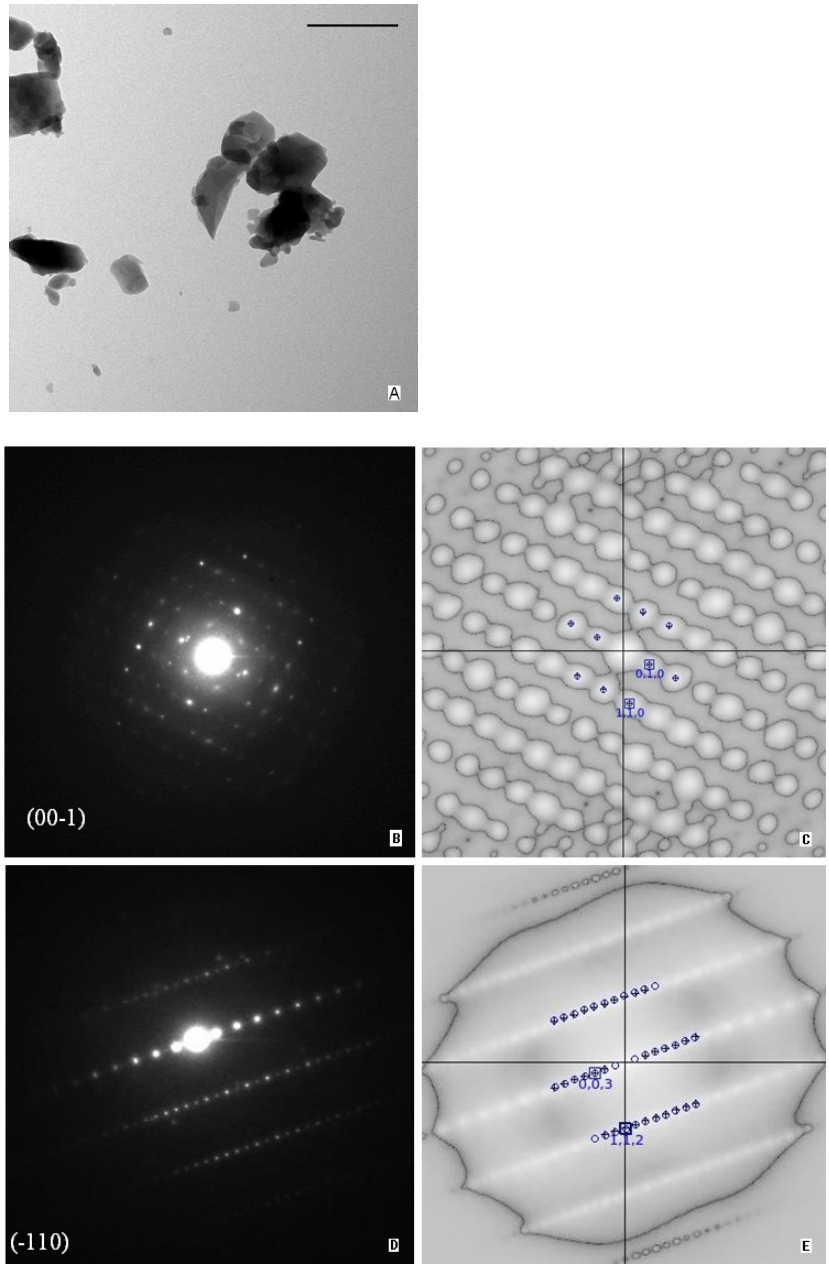

Figure 4 *(A) Crystals of potassium penicillin G (scale bar: 2 µm). (B-E) Electron diffraction patterns and corresponding autocorrelation patterns of potassium penicillin G from two main crystallographic zones. Crosses indicate the centroids of peaks in the*

autocorrelation image, circles indicate predicted the peak positions. The root mean square deviation (RMSD) of the experimental and simulated patterns for the different zones (diffraction patterns) is between 0.6% and 1.7%.

5.3.3 Unit cell determination of orthogonal lysozyme

In the case of orthogonal nano-crystals of hen egg lysozyme, our algorithm did not produce a unit cell that is known from literature (Saijo *et al.,* 2005; Biswal *et al*., 2000)(see fig. 1 for an example of a diffractogram and corresponding autocorrelation pattern, see table 2 for reported unit cells and the unit cell determined by our algorithm). For this calculation we used 19 different crystals. The crystals adopt preferred orientations on the EM grid and hence we also collected diffractograms at various random tilt angles to also get more samplings of spacings that preferred to point in the direction normal to the EM grid. Overweighting crystals with such rare orientations made the cell determination more robust, but in general very similar answers were obtained if we did not include this weighting. We do not exclude the possibility that the nano-crystals of lysozyme correspond to a new polymorph, but it may also be that the algorithm for some reason produces large error up to around 4% for large unit cells. Table 2 gives an overview of unit cells of some known polymorphs of lysozyme, together with the unit cell produced by our new algorithm

Table 2 *Representative unit cell parameters of orthorhombic hen egg lysozyme determined by single X-ray diffraction (first 3 entries) and electron diffraction of single nano-crystals from a powder sample using the new algorithm*

Method	**a (Å)**	**b (Å)**	**c (Å)**	**(α , β , γ)**
X-ray diffraction 1 (1wtm)	**30.43**	**56.44**	**73.73**	**3x90°**
X-ray diffraction 2 (1jj1)	**30.56**	**58.99**	**68.26**	**3x90°**
X-ray diffraction 3 (1f10)	**30.58**	**55.86**	**68.58**	**3x90°**
Electron diffraction	**31.5**	**52.5**	**89**	**3x90°**

5.4 Discussion and conclusions

Our new algorithm for unit cell determination is independent of knowledge about the angular relationship between experimentally determined diffraction patterns. It does assume that all diffraction patterns share a similar 3D lattice. Because it can deal with a limited number of outliers, it is fairly robust. Because our algorithm uses autocorrelation patterns rather than the original data, precise knowledge of the position of the beam center is not required, as autocorrelation patterns are always cantered by definition. Using autocorrelation patterns for unit cell determination would fail at higher diffraction angles, but since the wavelength of the electrons used (approximately 0.013Å) was 2 to 3 orders of magnitude smaller than the highest resolutions we used for our analyses (between 1 and 4Å), this did not impose any serious problems in practice.

For the small molecule crystals, which belonged to orthorhombic or cubic space groups and hence had 3 or less degrees of freedom in their unit cell parameters, the algorithm performed well, reproducing literature values within a few percent. We do not expect a higher level of accuracy, as the method is based on the low resolution spacings. In a subsequent indexing and unit cell refinement step, which will use the original diffraction pattern, we assume that these small errors can be reduced.

Somewhat surprising was the unit cell we found for orthorhombic lysozyme, which had a significantly shorter *b* axis and a significantly longer *c* axis than unit cells reported in literature. The unit cell volume of largest known orthorhombic polymorph of hen egg lysozyme was about 13% smaller than that of our nano-crystals (table 2). Unfortunately, our nano-crystals could not be grown to a larger size. Hence we could not corroborate the new unit cell by X-ray analysis and in the absence of independent proof, we cannot exclude the possibility that our algorithm failed to identify the correct unit cell of nano-crystalline lysozyme. It may be that the combination of randomly oriented diffraction patterns, a relatively large unit cell and a potentially anisotropic rocking curve frustrates our algorithm, and we are further investigating potential improvements. However, using the large unit cell, we were able to index well aligned diffraction patterns using the program ELD (Zou *et al*, 1993), yet we failed to index these patterns if we used the unit cells of known orthorhombic polymorphs of hen egg

lysozyme (fig. 5). Furthermore, all the known unit cells of lysozyme gave considerably worse residuals as defined by lemma (4), and therefore were not supported by our experimental data. In this light, we propose that the nano-crystals are a new polymorph of lysozyme, and that it was induced by the heterogeneous nucleation on human hair as described in Georgieva *et al.,* 2007.

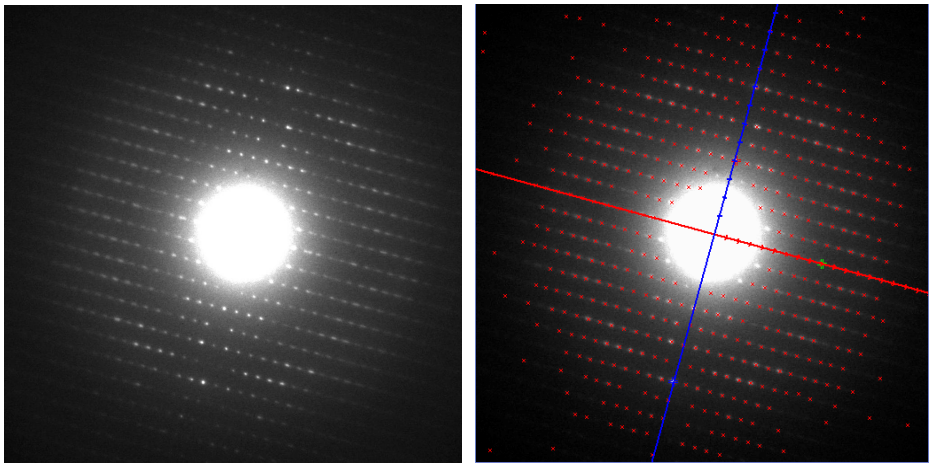

(a) (b)

Figure 5 *(a) Diffraction pattern from a lysozyme nano-crystal; (b) lattice indexing performed with ELD, using the cell parameters for lysozyme obtained by the algorithm described here. The directions of the shortest reciprocal spacings, given in blue and red and corresponding to the (100) and (011) axes, respectively, are indicated.*

How many diffractograms are needed to estimate the unit cell? There is not a straightforward answer to this question, but in general it is better to include as much data in the analysis as possible. If the crystals have a favoured orientation on the grid (as the lysozyme crystals did), then it is important to collect tilted data, as otherwise the possibility exists that one of the spacings is not observed. However, there are also other issues that influence the robustness of our algorithm, for instance the symmetry of the unit cell (higher symmetry gives better results) or peculiarities of a specific

combination of unit cell parameters – if, for instance, in an orthorhombic unit cell, the (100) and (021) directions have similar lengths, indexing may become confused.

With our new algorithm we have made progress in enabling structure determination by electron diffraction of beam sensitive 3D nano-crystals. Subsequent steps involve testing our algorithm on lower symmetry space groups (monoclinic and triclinic), refining the unit cell dimensions, indexing the electron diffraction patterns, integrating the diffraction intensities, merging the data and phasing. However, these subsequent steps crucially depend on knowledge of the unit cell and in many cases we can use algorithms and programs developed for X-ray crystallography.

Acknowledgements

The authors would like to thank Dr. Ulrike Zeise and Tom de Kruijff for technical support, Dr. S. Nikoloupulos and Prof. C. Giacovazzo for providing the pharmaceutical powders for the electron diffraction experiments, M.W.A.Kok for making the figure 3(B), Prof. X. Zou and Eleni Sarakinou for help with the programme PhIDO and Dr. Rag de Graaff, Vikas Kumar and Qiang Xu for the fruitful discussions.

References

Biswal, B.K., Sukumar, N. and Vijayan, M. (2000). *Acta Cryst*. **D**56, 1110-1119.

Boysen, H., Lerch, M., Stys, A. and Senyshyn, A. (2007). *Acta Cryst*. **B**63, 675-682.

Clegg W. (1981). *Acta Cryst*. **A**37, 913-915.

Dexter D.D. and van der Veen J.M. (1978). *J.Chem.Soc.Perkin Trans.* **1**. 185.

Georgieva, D.G., Kuil, M.E., Oosterkamp, T.H., Zandbergen, H.W. and Abrahams, J.P. (2007). *Acta Cryst*. **D**63, 564-570.

Gibon, V., Norberg, B., Evrard, G. and Durant, F. (1988). *Acta Cryst*. **C**44, 652-654.

Grosse-Kunstleve R.W., Sauter N.K. and Adams P.D. (2004). *Acta Cryst*. **A**60, 1-6.

Henderson R. (1995). *Q. Rev. Biophys*. **28**, 171-93.

Kabsch, W. (1993). *J. Appl. Cryst*. **26**, 795-800.

Kolb U., Gorelik T. and Otten M.T. (2008). *Ultramicroscopy,* **108**, 763-772.

Plaisier, J. R., Jiang, L. and Abrahams, J. P. (2007). *Journ. Struct. Biol.* **157**, 19-27.

PhIDO - Phase identificarion and indexing from ED patterns, Calidris, Solentuna, Sweden, 2001 www.calidris.em.com.

Saijo, S., Yamada, Y., Sato, T., Tanaka, N., Matsui, T., Sazaki, G., Nakajima, K. and Matsuura, Y. (2005). *Acta Cryst*. **D**61, 207-217.

Vainshtein B.K. (1964). *Structure Analysis by Electron Diffraction*, Oxford, Pergamon

Zou X. D., Hovmöller A. and Hovmöller S. (2004). *Ultramicroscopy,* **98**, 187-193.

Zou, X.D., Sukharev, Y. and Hovmöller, S (1993) *Ultramicroscopy,* **49**, 147-158.

Chapter 6

User manual of EDiff: A unit-cell determination and indexing software

EDiff® is a scientific software package to determine the unit cell of nano-crystals from the randomly oriented electron diffraction data. EDiff is used to index the reflections in the electron diffraction images, and is the first step in reconstructing the 3D atomic structure of organic and inorganic molecules and proteins.

EDiff includes the data pre-processing program AMP*, which cleans up diffraction patterns and calculates their autocorrelation patterns, which serve as input for EDiff.

EDiff: Copyright 2007-2008. BFSC, Leiden Univ., the Netherlands.

---

* A paper about the pre-processing program AMP was accepted and will be published in the proceeding of the 2009 IEEE International Conference on Image and Signal Processing (CISP'09): Jiang, L., Georgieva, D., IJspeert, K., Abrahams, J.P., 2009. An Intelligent Peak Search Program for Digital Electron Diffraction Images of 3D Nano-crystals.

6.1. The Electron-Diffraction-Software (EDiff) Package for Windows® Users

The package includes the following executable files:

- EDiff.exe;
- Patternson_dir_gui.exe;
- FirstInstall.bat
- MCRInstaller.msi and other supporting archives.

6.2. Configuring and running EDiff on Windows Platforms

1 Open/Unpack the package in a new directory.

2 Run FirstInstall.bat *once* on the machine where you want to use the software. MATLAB Component Runtime (MCR) Libraries will install automatically, 300M space on the C: disk is needed. Note: if installation fails, double click the file MCRInstaller.msi to install it.

3 Run Patternson_dir_gui.exe to start working with electron diffraction (EM) images. The fist time this program is started, it will unpack the supporting archives, taking several minutes. This software will generate four output files for each EM image: <image-name>.atc.plt, <image-name>.atc.jpg, <image-name>.ctr.pks, and <image-name>.ctr.png. Put these outputs in a separate directory for the next step.

4 Run EDiff.exe to determine the Unit-Cell parameters and index individual EM image.

6.3. AMP: Pre-processing diffraction data

The pre-processing program AMP (Autocorrelation Mapping Program) – with the executable file name Patternson_dir_gui.exe – has a Graphical User Interface (GUI).

This program is used to remove the background and for picking reflection spots from diffraction images. A snapshot of the user interface is shown in figure 1.

This program creates an autocorrelation pattern of the electron diffraction pattern which fills up gaps or absences in the data, enhances the signal to noise ratio, and centers the diffraction pattern. The autocorrelation map and peak coordinates serve as input files for EDiff, the main program that determines the unit cell of a crystal. The autocorrelation patterns are essential for finding the unit cell, but cannot be used for further steps in the structure determination.

6.3.1 Preparing the Input Data for the Pre-processing Program AMP

AMP expects electron diffraction images of about 1024 by 1024 pixels (though they needn't to be exactly this size). Furthermore, diffracted intensity should be positive ('white' on most display programs; if the spots are black on a white background, you have to invert the image). The beam center of the diffraction pattern should be more or less in the centered. Make sure that all the images that you want to process are in the same directory. It is good practice to store all the data of one EM session in a single directory, ensuring that all diffraction patterns were collected with the same voltage, camera length and digitization parameters. If these microscopy parameters are changed during a session, then separate the data set into different directories for proper processing.

6.3.2 Working with the Pre-processing Program AMP

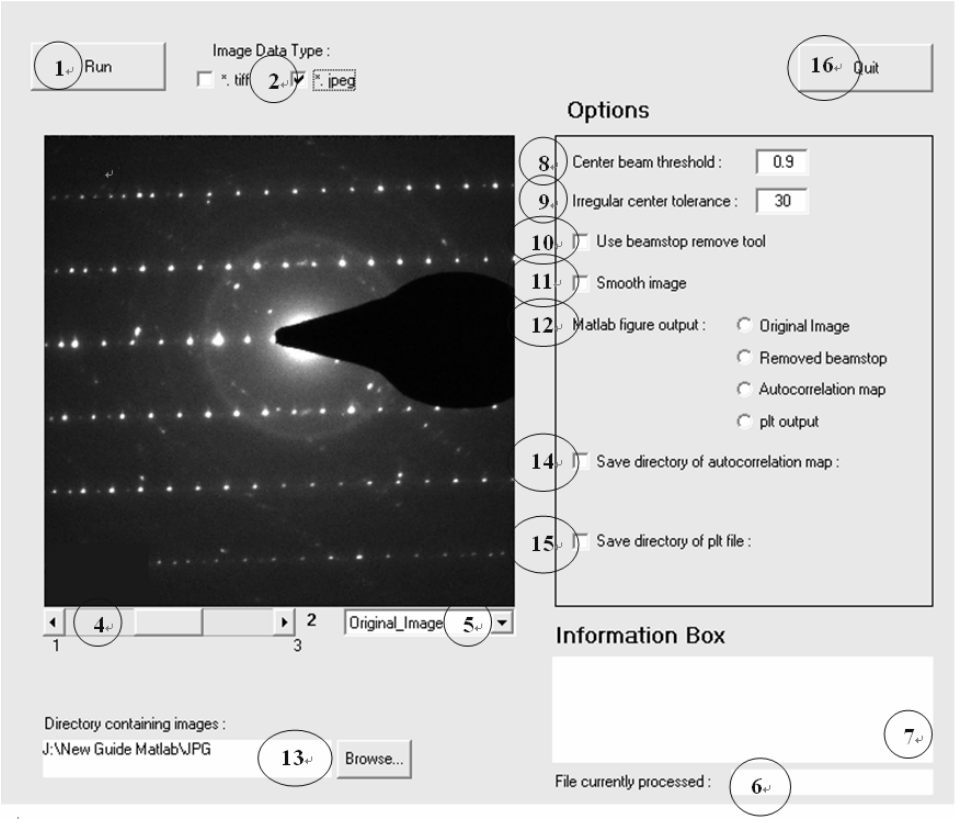

Figure 1 *Graphical User Interface of pre-processing program AMP V1.2 with all options highlighted.*

1. Run button to start the program with the desired settings
2. Selection of images types that will be processed
3. Image window
4. Slider to select current image in directory
5. Change to original pattern / Autocorrelation pattern / png-output pattern
6. Progress tracker
7. Information box containing error messages and help files
8. Parameter input, allowing the user to change area of the center beam that needs to be removed

9. Allows the user to make the program more or less flexible in finding the center of the diffraction pattern automatically. The number indicates the allowed error that is based on the difference in length between two different, independent calculations of the beam center. Setting it to a higher value allows the program to accept more elliptic or irregular shapes of the central beam, whereas setting it to 0 automatically redirects the user to a window for interactively setting the center.
10. Instead of setting the value to 0 one can also chose to use the beam stop removal tool for any given shape of beam stop. This comes in handy when the user suspects that the center is found far from its actual position.
11. Allows the user to smooth the image. This option is only advised when salt and pepper noise is present, because this type of noise is not removed well with the standard background removal tools. The user is notified that using this option might result in a minor loss of data.
12. Allows the user to decide which intermediate output images are shown while running the program. This output consumes large amounts of memory, so when you process more than ten images, you would better not choose this option.
13. Selects the directory that contains the original images (*.jpeg, *.tiff)
14. &15. Selects the directory that will be used to store the plt-files and autocorrelation images.
16. Quits the program

The program processes all images in one directory. One can chose to work with *.jpeg, *.tiff or both file types simultaneously. The program takes about 2 minutes to process a single image. In the current version, *we strongly advise against dragging or changing any windows that are related to the GUI during image processing,* or you might crash the program. Currently, AMP is a single thread program, which means that it can't handle more than one job at a time. Furthermore, there is a limited amount of virtual memory available, which allows a maximum of ~50 figure windows to be open simultaneously. *If you have a lot of images in one directory, make sure you have disabled the option of 'figure output'*.

To work efficiently, it is advised to work with electron diffraction data sets that all have been recorded in the same session. For a quick test, do not save any autocorrelation maps or plt-files just yet, because this option extends the running time by roughly one

minute. Removing the background can still go wrong, so a user should only enable the option ‘Removed beamstop’ to see the results of one single image. If one is satisfied, the user can proceed by enabling the ‘autocorrelation map’ and ‘show plt output’. When this output is reasonable as well, the user can disable all ‘figure outputs’ and process all images of the data set in a single run.

6.3.3 Output Data of the Pre-processing Program AMP

This program calculates autocorrelation images and extracts peak positions from diffraction patterns and their corresponding autocorrelation images. Four output files of each EM image are generated:

- <image-name>.atc.plt: the peaks positions of autocorrelation map;
- <image-name>.atc.jpg: the autocorrelation map
- <image-name>.ctr.pks: the peak positions of centered background-removed diffraction image,
- <image-name>.ctr.png: the centered background-removed diffraction image.

It is good practice to save these output files in another directory to avoid mixing with the original diffraction data.

6.4. EDiff: Finding Units Cells

EDiff.exe is the main program of the electron-diffraction (EDiff) software package. It finds and optimizes unit cell parameters and fits and indexes diffraction patterns. The input data for EDiff are *not* the original electron diffraction images, but the pre-processed output data from AMP (see above). Please read the part of manual on the pre-processing program AMP for more details. All the input data should be in one directory, typically 4 files for each electron diffraction image: <image-name>.atc.plt, <image-name>.atc.jpg, <image-name>.ctr.pks, <image-name>.ctr.png. All the data in one directory are assumed to be generated from one EM session, that is, with the same voltage, camera length of microscopy and digitization parameter. If not, the data have to be separated into different directories.

For unit-cell determination only, <image-name>.atc.plt and <image-name>.atc.jpg files are required. For indexing, <image-name>.ctr.pks and <image-name>.ctr.png files are required (please see the part of Indexing an Electron Diffraction Image with Known Unit-cell Parameters).

Click the 'SetDataDir' button to set the directory with the data that need to be processed. The selected directory will be shown in a line above the button.

Some definitions of electron diffraction images that are used in this document:

- A reflection is a spot corresponding to a vector from beam- or image center to this spot.
- Two reflection spots together with the beam- or image center point form a triangle; we call this a 'facet'.
- The facet defined by the two shortest vectors (corresponding to two reflection spots closest to the center) is called a 'main facet'.

In short, every reflection pair defines a facet. The main facet defines the smallest repeating unit of the 2D lattice defined by the low resolution spacings (but not any higher-order Laue zone (HOLZ) that may be visible at high resolution).

EDiff.exe also has a Graphical User Interface (GUI); a snapshot is shown in figure 2.

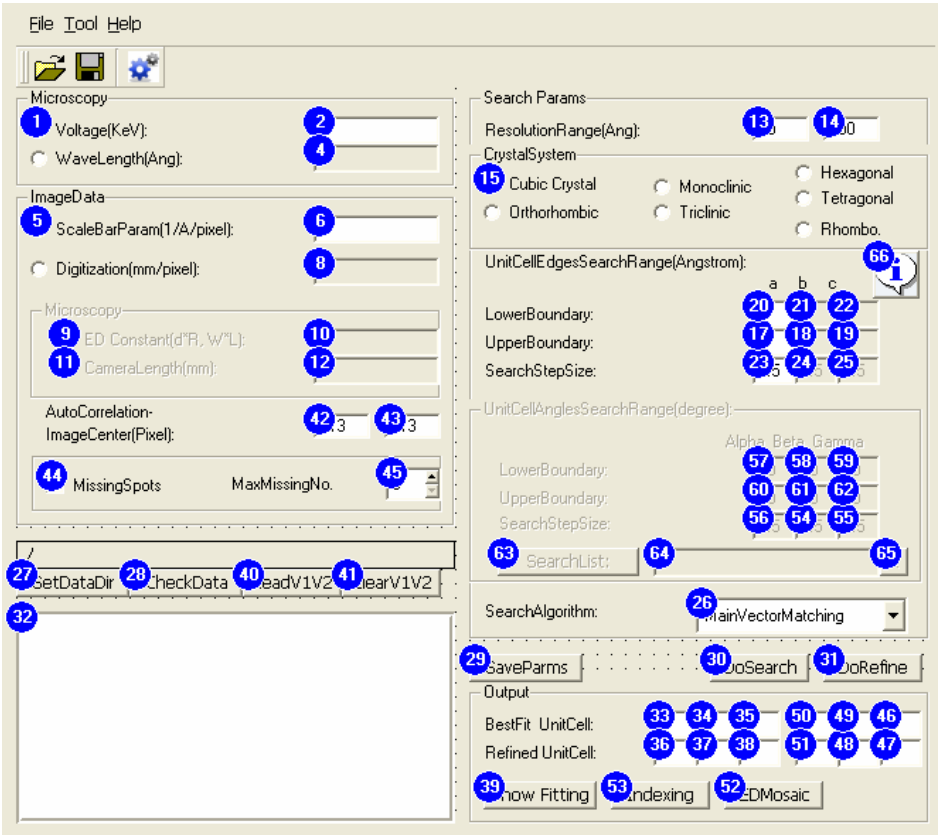

Figure 2 *Main graphical user interface of the program EDiff V1.0 with all options highlighted.*

1. Voltage (in KeV) of the electron microscope. The wave length (4) will be automatically calculated from the voltage (2). Alternatively, the user can enter the wave length and ignore the voltage. In the final calculation, the wave length is used rather than the voltage.

5. ScaleBarParam, the Scale Bar Parameter, defines the scale of the diffraction pattern in A^{-1} per pixel.

8. Alternatively, the 'Digitization' parameter can be entered, defining the step size in millimeter per pixel when scanning films, or the resolution of the CCD digital camera. In this case, the user also needs to set the 'ED Constant' parameter (9) (or the 'CameraLength' and 'WaveLength' parameters (11 and 4), from which the 'ED Constant' is calculated). The ScaleBarParam (5) is calculated from the 'ED Constant' (9) and the

"Digitization' parameter.

42. & 43. Image center of the autocorrelation image in pixels; this is also the center of centered, background-corrected electron diffraction pattern. For files generated by the pre-processing program AMP, these two values are always 513, corresponding to the center of a 1024 by 1024 size image.

44. MissingSpots indicates how many spots are allowed to be absent between the spots of main vector and the center. This parameter is used in MainVectorMatching and FullVectorMatching methods, which allow the user to include extra information on the symmetry of the crystal. If this parameter is not selected (MaxMissingNo. is zero), only 'prime' index reflections will be considered in the unit-cell searching. 'Prime' means no common factor for the (h,k.l) index, e.g. index (5,4,3) is prime, but (6,4,2) isn't, because the h, k and l have 2 as a common divisor. If you don't have information about known missing reflections, just leave it unchecked.

27. SetDataDir: set the input data directory, which is the output directory of the pre-processing program AMP (see 6.3).

28. CheckData allows some types of verification. It allows checking whether the peak positions of the auto-correlation images and peak positions of the background-removed diffraction pattern coincide. This helps the user to select the proper 'ResolutionRange' for the unit-cell parameter search. Setting 'CheckData' allows checking the main vectors for the 'MainVectorMatching' and 'Brightest Spots Matching' methods. The option saves the main vectors to a 'V1V2' file.

40. ReadV1V2: reads the main vectors 'V1V2' (the main facet) from a file.

41. ClearV1V2: clears the main vectors and unique facets from memory. If the user wants to re-select the main vectors or redo the unit-cell parameters search, it's better to erase the old settings (or to restart the EDiff program altogether).

32 Information Panel: some status information and results of the EDiff program will show up here.

13. & 14. ResolutionRange(Å): The resolution range, in Angstrom, is used for finding the unit-cell parameters and for indexing. Only peak positions within the specified resolution range will be used for the calculation. When the user starts 'CheckData', only reflections/spots within the resolution range will show up. If a very large resolution range is selected, a large number of spots is used in the calculation and this may cost too much computing time. If the resolution range is too narrow, the absence of essential of information may prevent finding the right answer. In practice, a resolution range that is a

bit wider than that defined by the main facet is fine. As a rule of thumb, a reasonable resolution range is from half of the estimated smallest unit-cell dimension to double of the largest unit-cell dimension. For example, if the smallest unit-cell dimension is expected to be around 30 Ångstrom and the largest dimension is around 80 Ångstrom, it is reasonable to set the resolution range between 15 and 160 Ångstrom.

15. CrystalSystem; all seven different crystal systems are supported in the unit-cell parameters determination. If we know the crystal system beforehand, we can apply its constraints in the exhaustive search of edges and angles, sometimes dramatically speeding up the calculations and improving their precision. If we don't know the crystal system, we have to use the most time consuming option – Triclinic.

66. Parameter Suggestion gives the user a suggestion for filling in the 'UnitCellSearchRange' based on an analysis of the main vectors generated in 'CheckData' step. This option requires first running 'CheckData' and saving the main vectors (V1V2).

17. – 19. UpperBoundary, largest unit cell edge in Ångstrom for a unit-cell parameter search.

20. – 22. LowerBoundary, smallest unit cell edge in Ångstrom for a unit-cell parameter search.

23. – 25. SearchStepSize, step size in Ångstrom for unit cell parameter search. Usual values are about 0.5 or 1 Ångstrom.

60. – 62. UpperBoundary, upper boundary in degrees for unit cell parameters search.

57. – 59. LowerBoundary, Lower Boundary in degrees for unit cell parameters search.

54. – 56. SearchStepSize, Step Size in degrees for unit cell angle search. Initially set this to about 1 degree.

63. SearchList, the user can define a list of angles to be checked, instead of performing exhaustive angle searching. The angle list should be saved as a text file, with each line a tri-angle group (alpha beta and gamma, in degrees and separated by blank space).

64. The file of the angle search list

65. Remove the angle search list

26. SearchAlgorithm: there are three unit-cell parameters search algorithms that can be selected:

- Unique Facet Matching: the friendliest algorithm, you don't even need to run 'CheckData' (except perhaps for setting the proper 'ResolutionRange') and it gives quick results.
- Main Vector Matching: requires running 'CheckData' to select / verify and save the facets of each diffraction image that are to be used in the calculation. This option is

useful for very noisy and/or marginal data

- Full Vector Matching: does not require running 'CheckData' as it uses all vectors within the resolution range. It can be rather slow, but it is useful for refinement and comparison.
- Brightest Spots Matching: a variation of 'Main Vector Matching', especially useful for thin nano-crystals with a large unit-cells.

For more details, please see the chapter on '**Unit-cell Parameters Determination'**.

29. SaveParms, save all the parameters in a file, so that the parameters can be loaded next time by select 'File-Open' menu.
30. DoSearch to start unit-cell parameter determination. The result will show on the console window and the 'BestFit UnitCell' column.
31. DoRefine, refine the unit-cell parameters refinement edge parameters: steepest descend refinement (with decreasing step size) starting from the 'BestFit UnitCell' and reporting the result in 'Refined UnitCell'.
33. BestFit UnitCell reports the best fitting unit cell parameters found by 'DoSearch' procedure.
36. Refined UnitCell reports the refined unit cell parameters generated by 'DoRefine' procedure.
39. Show Fitting: fit each auto-correlation image with the 'Refined UnitCell' model (if there is no refined unit cell, it uses the 'BestFit UnitCell' instead). Used for indexing an auto-correlation pattern and verifying the search result of the unit-cell parameters.
53. Indexing: index the centered background-removed diffraction image.
52. EDMosaic: simulating a diffraction pattern for testing.

By selecting the 'Tool'-'Config' menu, a window opens that allows detailed configuration of some global parameters, see Figure 3. The default parameters are empirical settings, they work well with most of the data used for testing. Don't change them, unless you do really know the meaning of each parameter (and know what you're doing)!

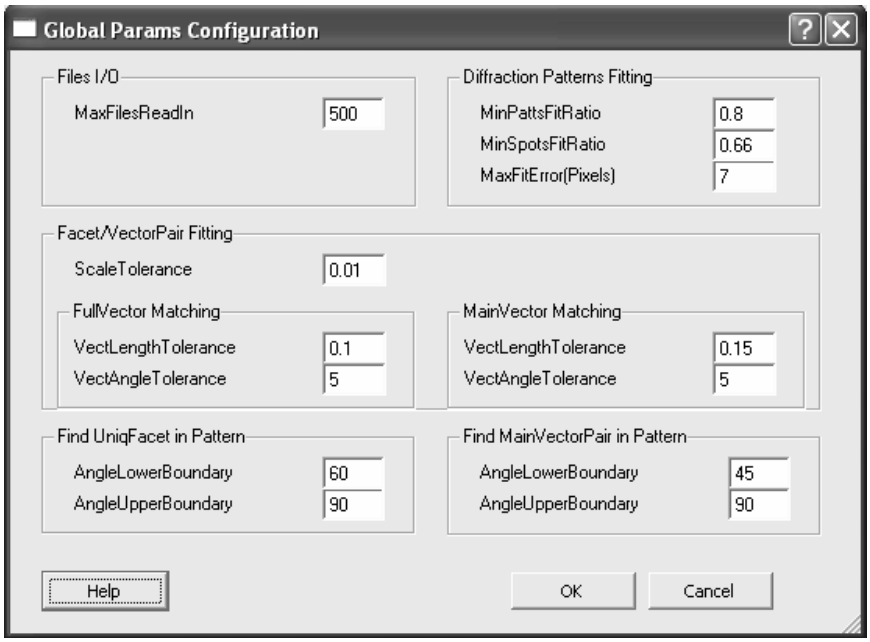

Figure 3 *More detail global technique parameters configuration of EDiff V1.0*

If you're really interested – a brief description of each variable is:

MaxFilesReadIn: Maximum number of *.plt data files that are read in memory.

MinPattFitRatio (for all patterns): Minimal fraction of properly fitting diffraction patterns. If this is high, many patterns must be explained well by the proposed unit cell. Unit cells that fail to reach this threshold are discarded. Normal values are 0.5 (50%), 0.66, 0.8

MinSpotsFitRatio (For one pattern): minimum spots fit ratio to detect correct fitting (if larger, mean fit), typical: 0.5 (50%), 0.66

MaxFitError (For one spot): max distance error in pixels, the distance between fitted and real spots should be smaller, typical value: 7 (pixels)

ScaleTolerance: max value of scale tolerance (0.01 is 1%), typical: 0.01, 0.03, 0.05

VectLengthTolerance: Vector Length Tolerance (0.1 is 10%), for fitFacet()[4] of FullVector & MainVector matching method

[4] 'fitFacet' is a function to calculate the fitting residue of two facets, which is used to judge the similarity of two facets.

VectAngleTolerance: Vector Angle Tolerance (in degrees), for fitFacet() of FullVector&MainVector Matching Method

AngleLowerBoundary: Angular Lower Boundary (in degrees), for UniqFacet in lattice.Lattice2MainFacet_BEval()[5]

AngleUpperBoundary: Angular Upper Boundary (in degrees), for UniqFacet in lattice.Lattice2MainFacet_BEval().

AngleLowerBoundary: Angular Lower Boundary, for MainVectorPair in lattice.Lattice2FacetTri_BEval()[6]

AngleUpperBoundary: Angular Upper Boundary, for MainVectorPair in lattice.Lattice2FacetTri_BEval()

6.5 Checking the Data

After having run AMP to prepare the data for EDiff, the data can be 'checked' by entering the data directory in EDiff (SetDataDir, button 27) and clicking the 'CheckData' button (28). This opens the window shown in Figure 4.

The purpose of checking the data is to allow the user to verify that the peak positions of the auto-correlation images and peaks positions of the background-removed diffraction patterns coincide. It also automatically finds the main facet (also called main vectors, V1V2) for each autocorrelation image. Here, the peaks of the spots within the resolution range are visualized as crosses; the points of simulated lattice generated from this main facet are indicated by small circles. Normally, if the crosses

[5] Lattice2MainFacet_BEval is a function to generate main facets from electron diffraction images for the Unique Facet Matching algorithm calculation. The angle of the facet is limited in between 'AngleLowerBoundary' and 'AngleUpperBoundary' of 'Find UniqFacet in Pattern'.

[6] Lattice2FacetTri_BEval is a function to generate main facets from electron diffraction images for the Main Vector Matching algorithm calculation. The angle of the facet is limited in between 'AngleLowerBoundary' and 'AngleUpperBoundary' of 'Find MainVectorPair in Pattern'.

overlap the circles very well, then that means the diffraction image is a well oriented pattern and the main facet was correctly found by the program.

Sometimes, the program can't find the correct main facet, in which case the user has to set it manually by first choosing 'ResetV1' or 'ResetV2' and then double clicking the correct peak/cross in the image. The selected V1 or V2 will be automatically switched if the length of V1 is larger than V2. There are lots of tricks for making your life easier: <double click left mouse button> will capture a cross near the place you clicked. <double click middle mouse button> will locate the exact place that you clicked; by pressing <Ctrl> at the same time, it will try to find a intensity peak near the place you clicked. There are more complicated options for advanced users: if you press the key <Shift>, <Alt> or <Ctrl> when you do <double click left mouse button> or <double click middle mouse button> on the peaks of the image, the 1/2, 1/3 or 1/4 position is located relative to the cross that you selected or the point that you clicked. You even can combine use the <Shift> and <Alt> key, which will locate 1/6 position. When the peaks are not correctly generated by the pre-processing program AMP, these operations are very useful to help you to manually reset the correct V1 and V2, provided you know what you're doing (which requires understanding reciprocal space).

The user can run CheckData to find the proper 'ResolutionRange' for the unit-cell parameter search. A very large resolution range is fine from a theoretical perspective, but may include too many spots in the calculation and therefore cost too much computing time. A resolution range that is too narrow may lose essential information. When adjusting the resolution range, don't forget to press 'enter' after having filled in the numbers. Let the resolution range (shown as two black circles in the image window) just cover all the main vectors (or make it just a little larger). A reasonable resolution range extends from half of the estimated smallest unit-cell dimension to double the largest unit-cell dimension, e.g. if the smallest unit-cell dimension is around 30 Å and the largest dimension is around 80 Å, a reasonable resolution range extends from 15 to 160 Å.

The main vectors generated in 'CheckData' will be used in the MainVectorMatching algorithm and in the 'Brightest Spots Matching' method. In order to validate the main facets/vectors selected here, the user has to save the main vectors by clicking the 'Save

V1V2' button or 'Save As' a 'V1V2' file. For the UniqFacetMatching method, the program will generate the main facets automatically when the unit-cell parameter search is started. Running 'CheckData' is not required for the UniqFacetMatching and FullVectorMatching algorithms.

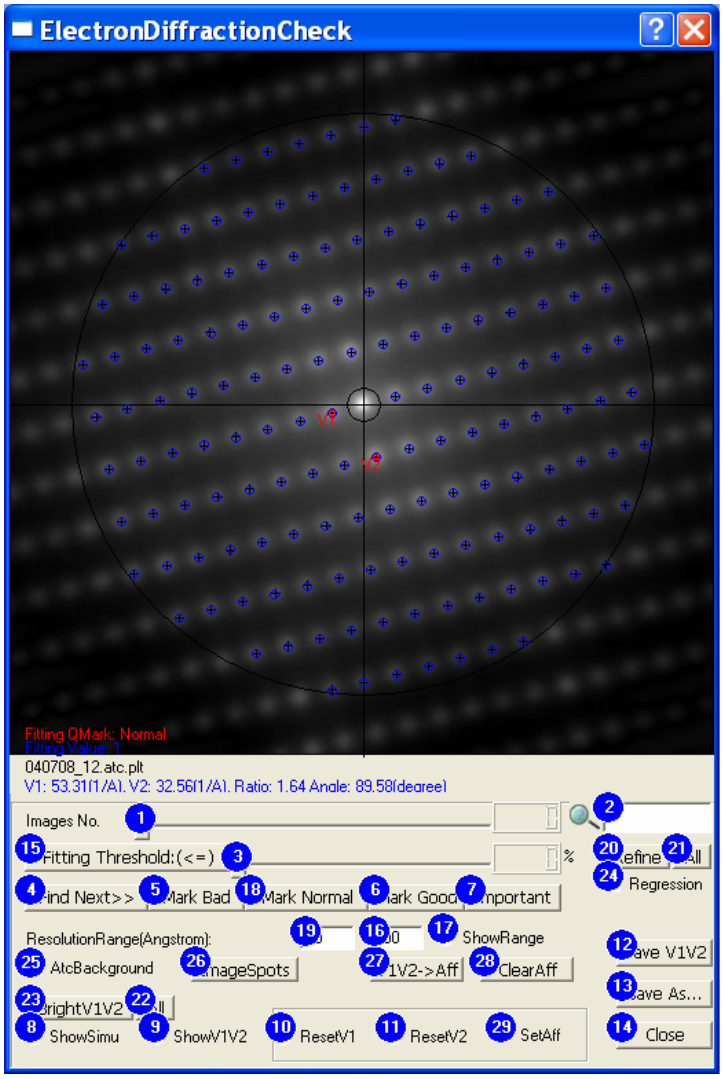

Figure 4 *Check-data window in EDiff V1.0, all options highlighted.*

1. Slide bar to select an image for checking, the sequence number will show on the right.

When the bar is active, the left and right arrow keys can also be used to slide the bar.

2. Search box, used for locating a file by typing in the filename and pressing ‘enter. If more files match the name, pressing enter switches between them.
3. Slide bar to set the fitting threshold (show on the right), which is used in the ‘Find Next’ function.
4. ‘Find Next >>’: click this button to find the next pattern that has a fitting value larger (or smaller) than the Fitting Threshold. ‘Fitting value’ is a measure of how well the simulated lattice fits with the experimental autocorrelation pattern.
5. – 7. Mark the quality of the image as Bad, Normal, Good or Important. This is used to weigh the images, as sometimes certain orientations are rare, but give vital information on one of the cell parameters. Only in such cases and provided the image is nice, it should be marked as ‘Important’.
16. ResolutionRange: allows entering the resolution range manually. Don’t forget to press <Enter> to validate it. If the values of resolution range are changed here, they will also be changed in the main window of EDiff.
17. ShowRange: shows the resolution range as two black circles in the pattern.
25. AtcBackground: shows the autocorrelation image or background-removed diffraction pattern as background. By default, the autocorrelation pattern is shown.
26. ImageSpots, show the peaks of the background-removed diffraction pattern as dark blue crosses, or show the peaks of autocorrelation pattern as black crosses, or show both.
27. V1V2->Aff, add V1 and V2 to An affiliate spots list[7].
28. ClearAff, delete all the spots in the affiliate spots list.
29. SetAff: if this button is checked, ‘V1V2->Aff” and ‘ClearAff” operations will only apply to the current image. When clicking in the image with this button selected, a new affiliate spot will be added to the affiliate spots list.
23. BrightV1V2: find the brightest two spots in the diffraction pattern and select these as the main facet.
22. All: do the ‘BrightV1V2’ search for all the images, not only for the current one.

[7] An ‘affiliate spots list’ is a list of reflections that is used for checking a simulated 2D lattice. Every diffraction simulation of a potential unit cell *must* contain the main facet (V1 & V2 spots) *and* all the affiliate spots in the same time; otherwise, it’s *not* a correct simulation.

8. ShowSimu, show the simulated lattice as small blue circles by tiling the main facet.
9. ShowV1V2, show in red labels ‘V1’ and ‘V2’ in the image.
10. ResetV1, reset the main vector V1 spot in the image. V1 or V2 will be automatically switched if the length of V1 is larger than V2
11. ResetV2, reset the main vector V2 spot in the image.
20. Refine, use all the spots on a single line (or a multi-regression method if option ‘regression’ (24) is selected) to recalculate the V1 and V2, the operation makes V1 and V2 fit the image better and their coordinates can now be non-integer pixel multiples.
21. All, ‘Refine’ all the images, not only current one.
24. Use the multi-regression method to for ‘Refine’ and refine ‘All’.
12. & 13. Save V1V2: In order to validate the main facets/vectors selected here, the user has to save the main vectors by clicking the ‘Save V1V2’ button or ‘Save As’ a ‘V1V2’ file.
14. Close this window

20, 21 & 24 are optional tools, while 22, 23, 27-29 are only used in the ‘Brightest Spots Matching’ method.

6.6 Unit-cell Determination

One of the main functions of EDiff is to determine the unit cell of nano-crystals from the randomly oriented electron diffraction data. Our algorithm is based on matching the observed crystal facets to model facets extracted from a simulated 3D lattice (or a detailed description of the algorithm, see chapter 5).

EDiff has several variations of the general algorithm for identifying unit cell parameters, which are discussed below.

6.6.1 Algorithm 1: Unique Facet Matching

This algorithm is the most straightforward one. It is a good idea to try this method first, especially for first-time users. Below, we walk you through the procedure.

Main steps:

1. Set the basic microscope and diffraction parameters in the graphic interface (figure 2). Choose a data directory with ‘SetDataDir’. If you know the crystal system or want to test out whether your assumption of the crystal system is reasonable, select it, otherwise select ‘Triclinic’. Set the search range of edges and angles. Set the ‘SearchAlgorithm’ to ‘UniqFacetMatching’.
2. Find the proper ‘ResolutionRange’: click ‘CheckData’ and adjust the resolution range to cover all the main vectors in different images. Close the window of ‘CheckData’. ‘Save V1V2’ is NOT necessary.
3. Click the ‘DoSearch’ button to perform unit-cell parameters search. The console window running in the background will indicate progress.
4. The best fitting unit-cell parameters will be displayed in the ‘BestFit UnitCell’ column and the best five results will be shown in the console window. Use ‘Show Fitting’ to check whether the result is reasonable or not.

This algorithm is the most automated one. After the user has clicked the ‘DoSearch’ button, the program first generates a main facet for each autocorrelation pattern and accumulates all the facets in List1, then analyses List1 to remove any congruent facets, shrinking List1 to contain only unique facets. The matching procedure is described in fig. 5.

6.6.2 Algorithm 2: Main Vector Matching

This algorithm requires more user interaction compared to the Unique Facet Matching algorithm. The most important difference is that the main facets (V1 & V2) have to be examined (and possibly reset) by the user using the ‘CheckData’ tool. The main facets in List1 are checked by hand and a quality remark (Bad, Normal, Good, or Important) can be given to each individual image. Congruent facets extracted from different diffraction pattern are not removed from List1. When the experimental data are very noisy and lots of mis-tilted diffractions were collected, this solution is more reliable in the hands of an experienced user. The user is encouraged to run ‘CheckData’ and try this method for more accurate results.

Main steps:

1. Set the basic microscope and diffraction parameters in the graphic interface (figure 2). Choose a data directory with 'SetDataDir'. If you know the crystal system or want to test out whether your assumption of the crystal system is reasonable, select it, otherwise select 'Triclinic'. Set the search range of edges and angles. Set the 'SearchAlgorithm' to 'MainVectorMatching'.
2. Find the proper 'ResolutionRange': click 'CheckData' and adjust the resolution range to cover all the main vectors in different images.
3. In the window of 'CheckData', verify that the V1 and V2 spots (auto-selected by the program) are the closest two spots near the center. If there are any other spots closer to the center, reset the V1 or V2 to these spots. Normally a correct choice for V1 & V2 result in a high 'fitting value' between the image peaks and a lattice using V1&V2 as a basis. Please read the section 6.5 on **Checking the Data** for more details.
4. 'Save V1V2' or 'Save As' a V1&V2 file before closing the window of 'CheckData'.
5. Click the 'DoSearch' button to perform unit-cell parameters search. The console window running in the background will indicate progress.
6. The best fitting unit-cell parameters will be displayed in the 'BestFit UnitCell' column and the best five results will be shown in the console window. Use 'Show Fitting' to check whether the result is reasonable or not.

When the user clicks the 'DoSearch' button, the program will use the main facets saved in the 'CheckData' step in List1. For the Main Vector Matching algorithm, this List1 is filled interactively using the 'CheckData' tool. In testing out potential unit cells, unit-cells are skipped if none of its facets can be matched to the measured patterns marked as 'Important'.

6.6.3 Algorithm 3: Full Vector Matching

To the user, the Full Vector Matching algorithm appears very similar to the Unique Facet Matching algorithm, but its inner workings are different. Normally, it's rather slow and we advise you to only use it for comparison and verification. On the other hand, as it uses more data, it can be more accurate.

Main steps:

1. Set the basic microscope and diffraction parameters in the graphic interface (figure 2).

Choose a data directory with ‘SetDataDir’. If you know the crystal system or want to test out whether your assumption of the crystal system is reasonable, select it, otherwise select ‘Triclinic’. Set the search range of edges and angles. Set the ‘SearchAlgorithm’ to ‘FullVectorMatching’.

2. Find the proper ‘ResolutionRange’: click ‘CheckData’ and adjust the resolution range to cover all the main vectors in different images. It is important to set the resolution range as narrow as possible, as this solution is very time consuming since it uses *all* the vectors in the resolution range in its calculations. Close the window of ‘CheckData’. ‘Save V1V2’ is NOT necessary.
3. Click the ‘DoSearch’ button to perform unit-cell parameters search. The console window running in the background will indicate progress.
4. The best fitting unit-cell parameters will be displayed in the ‘BestFit UnitCell’ column and the best five results will be shown in the console window. Use ‘Show Fitting’ to check whether the result is reasonable.

When the user clicks the ‘DoSearch’ button, the program will use all the possible vectors pairs (not only the main facet) in each autocorrelation image for its calculations. For matching an observed vector pair (a facet in List1) to a simulated facet in List2, a 2D lattice is generated from the simulated facet and compared with the observed diffraction pattern to get a fitting value. The fitting value is used as the accumulated residual, which is different from the residual of two fitted facets in the other solutions. By using all the vector pairs and simulating 2D diffraction patterns, this algorithm requires heavy computing and is therefore slow.

6.6.4 Algorithm 4: Brightest Spots Matching (especially suited for large unit cells)

The ‘Brightest Spots Matching’ algorithm is a variation of the ‘Main Vector Matching’ algorithm. It’s the most accurate algorithm and is especially useful for thin nano-crystals with large unit-cell. However, it does require some expertise and you need to know what you’re doing. Try it out if you have plate-like nano-crystals that lie in preferred orientations on the grid. If this is the case, the information of the unit cell dimension in the direction of the beam is not (well) determined. If this is the case,

make sure to tilt the samples away from the main zones before diffracting them by as high an angle as the microscope allows. Moreover, if the unit-cell is large, the reflection spots will often be elongated in the direction normal to the plane of the crystal due to the wide 'spike function' (or 'rocking curve' in X-ray terms) in this particular direction. This can be caused by the limited number of unit cells in this direction. As a result of this elongation, the positions of the reflections present on the diffraction patterns may not represent the centroid of the reflection. As this is an implicit assumption of the algoritms discussed previously, they may not be reliable any more for thin, plate-like nano-crystals with a large unit-cell. This may be compounded by missing information on the unit cell dimension normal to the plane (a few ultra-high tilted diffraction images may still have some useful information, but may have a very poor quality due to the high tilt).

This algorithm abandons the idea of using the main facets, and instead uses the two brightest spots in the diffraction image (*not* the autocorrelation image). The brightest spots are most likely to have their centroids closest to the Ewald sphere and can be further from the center, thus containing higher index information, also in the direction normal to the plane of the crystal.

The main practical difference from the users perspective is that the two brightest spots are set as the new main facet (V1 & V2) in 'CheckData' tool. *It is strongly advised to set the original main facet (old V1 & V2) as affiliate spots.* Buttons 22, 23, 27-29 of the 'CheckData' window (see figure 4) allow these actions. Button 27 'V1V2->Aff' must be used to add V1 and V2 to the affiliate spots list. Button 23 'BrightV1V2' will find the brightest two spots in the diffraction image and reset V1&V2 to them. The user can switch the background from the autocorrelation pattern to centered diffraction pattern for verification (by turning off the radio button 25 'AtcBackground').
This solution proved also valid and reliable in various test cases in which the experimental data were very noisy and lots of miss-tilted diffractions were collected. We encourage all experienced users to try this method at least once!

Main steps:

1. Set the basic microscope and diffraction parameters in the graphic interface (figure 2). Choose a data directory with 'SetDataDir'. If you know the crystal system or want to test

out whether your assumption of the crystal system is reasonable, select it, otherwise select 'Triclinic'. Set the search range of edges and angles. Set the 'SearchAlgorithm' to 'BrightestSpotsMatching'.

2. Click 'CheckData' and set a large resolution range to cover most of the brightest spots in different images.
3. In the window of 'CheckData', visually check the main facet V1&V2. Button 20 'Refine' (in figure 4) can be used to refine the position of V1&V2. Button 27 'V1V2->Aff' (in figure 4) is used to add V1&V2 to an affiliate spots list. Button 23 'BrightV1V2' will find the brightest two spots in the diffraction image and reset V1&V2 to them. The user can switch the background from the autocorrelation pattern to centered diffraction pattern for a better visualisation (by turning off the radio button 25 'AtcBackground'). Be careful of Button 22 and 29 as their operation will affect all the images, not just current one.
4. Find the proper 'ResolutionRange'. In the window of 'CheckData', adjust the resolution range to cover all the brightest spots and affiliate spots in all images that must be used in the calculation. 'Save V1V2' or 'Save As' a V1&V2 file, and then close the window of 'CheckData'.
5. Click the 'DoSearch' button to perform unit cell search. The console window running in the background will indicate progress.
6. The best fitting unit-cell parameters will be displayed in the 'BestFit UnitCell' column and the best five results will be shown in the console window. Use 'Show Fitting' to check whether the result is reasonable or not.

When the user clicks the 'DoSearch' button, the program will use both the V1&V2 *and* main facets (as affiliate spots) saved in 'CheckData' step. In the searching, every diffraction simulation of a potential unit-cell has to match the V1&V2 spots and all the affiliate spots at the same time. Because this method needs to check the additional affiliate spots, it's a bit slower than the normal 'Main Vector Matching' method.

6.7 Pattern Fitting of the Autocorrelation pattern: Verifying the Unit-cell Parameters

After unit cell parameters have been found, 'Show Fitting' (39, in figure 2) can open a pattern fitting window for verification. The 'Pattern Fitting' window will fit each

auto-correlation pattern with the 'Refined UnitCell' model (or, if this does not exist, with the 'BestFit UnitCell' instead). The 'Pattern Fitting' window will index the auto-correlation image. Therefore, the control panel (see fig. 5) has the same interface as the 'Indexing Refinement' window.
This 'Pattern Fitting' algorithm works as follows:

1. find the facet in a simulated 3D lattice that best fits the main facet of an autocorrelation pattern;
2. then cut through the 3D model lattice using the plane defined by the best fitting facet to generate a 2D diffraction simulation.

In figure 5, crosses mark the peaks of the spots of the autocorrelation image and blue circles mark the model lattice. If the unit-cell is correct, the crosses and the blue circles should overlap well. When almost of the images (>90%) fit well, the unit cell most probably is correct. The outliers might be caused by the inclusion of some deviant crystals in the data set, by poor crystals with streaked rocking curves, by unfortunate orientations or unexpected failures to index the pattern properly. Only an experienced eye can tell. However, don't be fooled into certainty when the information of one unit cell dimension is missing in the original data (some crystals have a preferred orientation, and if you haven't tilted the diffraction grid, you may not have sampled the reciprocal lattice well enough).

If you don't believe a certain indexing, click 'FitFacets' (17 in figure 5B) to go through all potential fittings in a spin-box (16 in figure 5B). The fitted facets are sorted and a smaller number should give a better fitting.
The buttons and options in 'RefineOrient' group box are not originally designed for this 'Pattern Fitting' window, but for refining the orientation of diffraction image in the 'Indexing Refinement' window. However, if you really want to, you can use this 'RefineOrient' operation to index the autocorrelation pattern for testing and comparing, even though some buttons to do with refining diffraction patterns may be not fully functional for refining autocorrelation images.

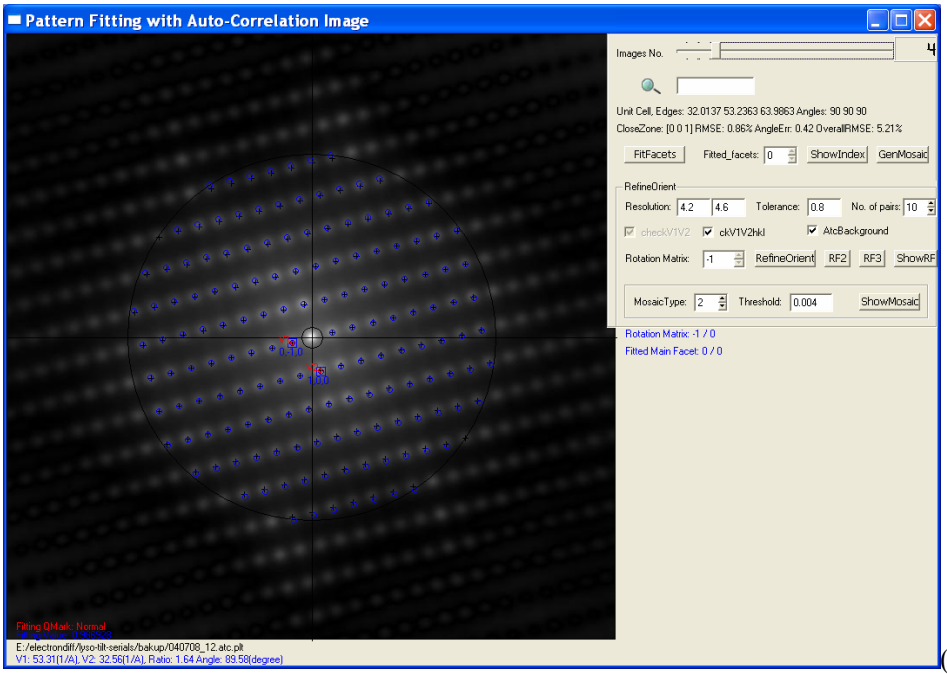

(A)

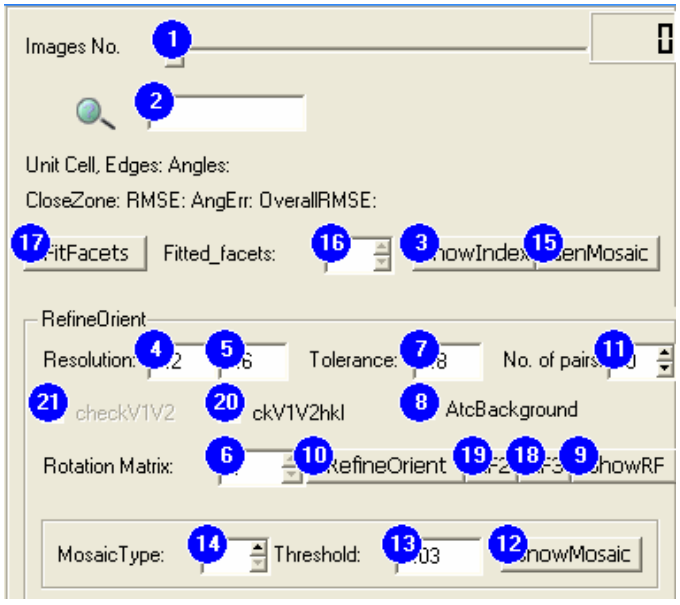

(B)

Figure 5 *(A) Pattern fitting of the main facet and the peaks of the autocorrelation image to unit-cell parameters. Crosses mark the peaks of the spots of the*

autocorrelation image, blue circles mark the best fitting diffraction simulation of a given unit-cell. (B) Control Panel of the 'Pattern Fitting' and 'Indexing Refinement' window in EDiff V1.0 – all options highlighted and described below.

1. Slide bar to select an image, its sequence number will be shown on the right. When the bar is active, the left and right arrow key can also be used for controlling the bar.
2. Search box, locate a file using its name and pressing enter, if more files match the name, press enter to switch between them.
16. Fitted_facets spinbox, select a specific facet if more than one facet was generated by 'FitFacets'.
17. FitFacets, find all the potential facets that fit V1 & V2.
3. ShowIndex, show/turn off the fitted pattern and its index.
15. GenMosaic, generate a diffraction pattern using the mosaic parameters described below
4. & 5. Resolution range from which select 'No. of pairs' facets (11) for refining the orientation using 'RefineOrient' (10): fitting and indexing the high resolution reflections in order to find a more accurate orientation of the diffraction image. Don't forget to press <enter> after having inserted a value. The resolution range will show up as blue circles. Be sure this resolution is within the global 'ResolutionRange' (show as black circles, set on EDiff main interface, figure 2).
7.Tolerance, maximum index error tolerance used for indexing high resolution reflections in 'RefineOrient'.
11. Maximum 'No. of pairs' facets for refining the orientation using 'RefineOrient'.
20.ckV1V2hkl, check the existence of V1 & V2 with their indices when indexing the high resolution reflections in 'RefineOrient'. Only useful when the 'MainVectorMatching' algorithm was selected (V1 & V2 must exist for this option to be meaningful).
21.checkV1V2, check the existence of the two reflections V1 & V2 and show their positions when indexing the high resolution reflections in 'RefineOrient'. Only useful when the 'MainVectorMatching' algorithm was selected (V1 & V2 must exist for this option to be meaningful).
8. AtcBackground, show the autocorrelation image or background-removed diffraction image as background. The default for 'Pattern Fitting' is to show the autocorrelation image; for 'Indexing Refinement' the default is to show the background-removed diffraction image.
6. Rotation matrix defining the potential orientations found by 'RefineOrient', 'RF2', or

'RF3'. The matrices are sorted by quality: the top matrices fit best.

10. RefineOrient, finds a more accurate orientation of a diffraction image using known and/or found unit cell parameters by selecting pairs of high resolution reflections, and fitting and indexing these pairs.

19. RF2 provides a different method for orientation refinement, sampling all different tilt orientations based on the orientation of V1 &V2 (and their indices) to find the best fitting.

18. RF3 provides yet another method for orientation refinement, sampling all different tilt orientations based on the orientation of V1 &V2 to find the best fitting. The spike function of the reflection is considered, that is, the elongation of the reflection is simulated. The 'MosaicType' must be 3 (side elongation, threshold default value 0.05).

9. ShowRF, show/turn off the simulated refined pattern and its indices; for indexing an autocorrelation image, 'ShowMosaic' may be a better choice.

12. ShowMosaic, show/turn off the simulated pattern with increased mosaicity, together with its indices.

13. Threshold for the simulation an increased mosaicity. For mosaic type 1 the default is 0.03, for mosaic type 2 it is 0.004, for mosaic type 3 the default is 0.05,

14. MosaicType encodes different models for simulating the mosaic spread of the diffraction pattern. It defines whether an off-Ewald sphere reflection should be shown on the simulated diffraction or not. 1: Angular mosaic, the angular error of a reflection. 2: Absolute distance, the reciprocal distance between a reflection and the Ewald sphere. 3: side elongation, simulate the spot elongation along the main direction of the unit cell that lies most closely to the direction of the electron beam and calculate the reciprocal distance to the Ewald sphere (useful for very thin, plate-like crystals that have characteristics of 2D crystals). .

6.8 Indexing an Electron Diffraction Image with Known Unit-cell Parameters

Once unit cell parameters have been inferred, clicking the 'Indexing' (53, in figure 2) button opens the 'Indexing Refinement' window (figure 6). This window is used for indexing centered, background-corrected diffraction images. The main difference between 'Indexing Refinement' (figure 6) and 'Pattern Fitting' (figure 5) is that in the

former a diffraction pattern is indexed and in the latter an autocorrelation image is indexed . The default background of ‘Indexing Refinement’ window is the diffraction image, while the default background for ‘Pattern Fitting’ is the autocorrelation image.

After having found unit cell parameters, the global ‘Resolution Range’ (set in the EDiff main window) can be increased for ‘Indexing Refinement’. The ‘Search Algorithm’ should be changed to ‘MainVectorMatching’, no matter what algorithm was used for getting the unit-cell parameters. It is necessary to run ‘Check Data’ in order to select a main facet on which the indexing refinement will be based.

When the window opens, a rough fitting is showing. It’s the same as in the ‘Pattern Fitting’ window: the program finds the best fitting facet in a simulated 3D unit-cell model for the main facet (V1 & V2), then cuts through the 3D model lattice along the plane defined by the selected facet in order to generate a simulated 2D diffraction pattern (show as small blue circles). If the diffraction image is taken right from the main zone, this provides an accurate indexing. However, in more usual cases, the experimental diffraction pattern is tilted away from the main zone. In order to find the exact orientation of an individual diffraction image (so as to index the reflections correctly), we need to select ‘Refine Orient’, which opens a new window (fig. 6).

The ‘RefineOrient’ is based on the index of the main facet (V1&V2). Hence the ‘MainVectorMatching’ or ‘BrightestSpots’ algorithms are strongly suggested for indexing refinement.

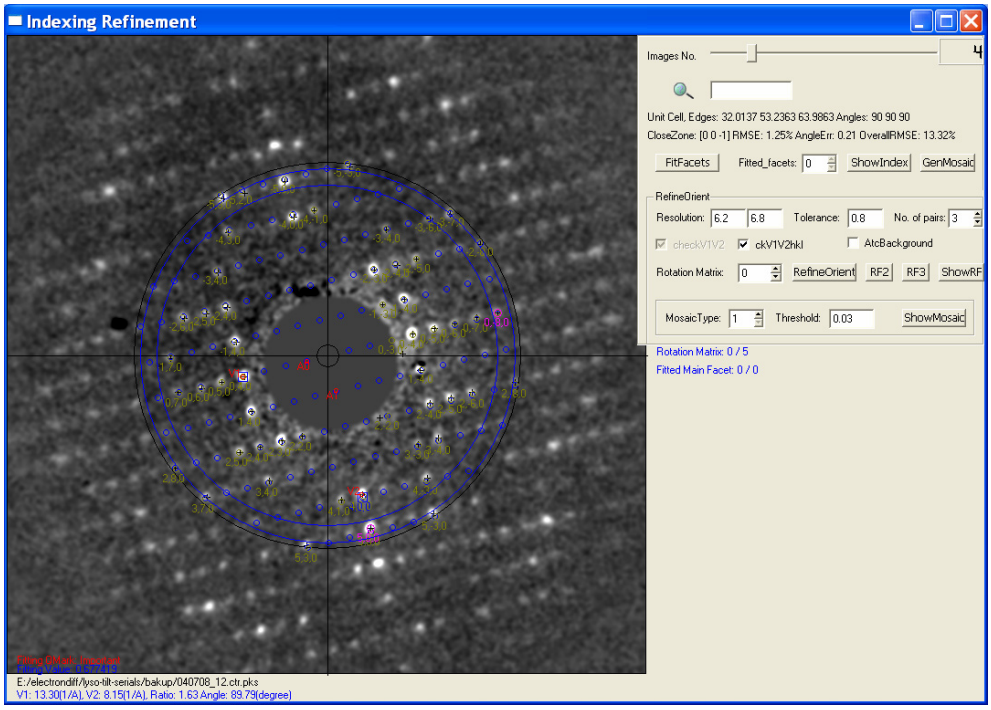

Figure 6 *Indexing of a background-corrected diffraction pattern using unit-cell parameters that were inferred in earlier steps. Crosses mark the peak positions of the reflections of the diffraction image; Small blue circles are the best fitted diffraction simulation of the selected unit cell. Here, the unit cell was determined using the 'Bright Spots Matching' algorithm; V1 & V2 are the two brightest spots of the diffraction pattern; A0 and A1 are the affiliate spots of the autocorrelation image. The control panel of this window shares its interface with the 'Pattern Fitting' window (fig. 5B)*

Steps of orientation refinement and indexing:

1. Visually check whether the main facet (V1 & V2) fits well and is reasonable indexed. If not, click 'FitFacets' (17 in figure 5B) to generate all possible solutions and pick a better fitting facet. The 'RefineOrient' procedure is based on this fitted facet. If this fitting is not correct, the orientation refinement and indexing will be meaningless.

2a. Select 'RefineOrient'. Select the 'Resolution' range from which 'No. of pairs' facets are used for the refinement (4, 5, 7, 11 in figure 5B need to be set). The 'RefineOrient' procedure will select pairs of high resolution reflections, fitting and indexing these high resolution facets to find a more accurate orientation of the diffraction pattern, using the known or inferred unit cell parameters. If

'ckV1V2hkl' (20 in figure 5B) is checked, the procedure will ensure that V1 & V2 *together* with their indices are present in the simulated pattern, when indexing the high resolution reflections. If you're uncertain of the correctness of the indices of V1 & V2, click the radio button 'checkV1V2' (21 in figure 5B) to ensure the existence of two reflections shown on the positions of V1 & V2, but *without* fixing their indices (so in this case, other orientations that change the indices of V1 & V2 are also allowed).

2b. Alternatively to 'RefineOrient', the algorithms 'RF2' and 'RF3' can be selected. Some parameters for 'RefineOrient' (4, 5, 7, 11, 20, 21 options in figure 5B) are not used by 'RF2' and 'RF3'. Other parameters: 'MosaicType' and the mosaic 'Threshold', are required.

Selecting the correct parameters for 'MosaicType' and mosaic 'Threshold' can be critical for the program to find the correct orientation. The program samples all different tilt orientations based on the orientation and indices of V1 &V2, and selects the best fit (between the simulated and the observed diffraction pattern). In 'RF2' the rocking curve (or spike function) of the reflections is not considered. In 'RF3' The difference between 'RF2' and 'RF3' is, spike function of a reflection is considered in 'RF3', an elongation in reciprocal space of a reflection is simulated. The most meaningful 'MosaicType' is 3 for 'RF3', although you could try selecting mosaic type 1 or 2: there is no error message. 'MosaicType' 3 indicates a lengthwise elongation of the diffraction spot in a principal direction of the lattice; its default threshold value is 0.05. See section 6.7 for an explanation of the various mosaic types.

For inorganic materials that have crisp diffraction patterns, 'RefineOrient' and 'RF2' will be fine for reasonable indexing. For the crystals with a large unit cell, e.g. the protein nano-crystals, the reflection spots can be elongated along the unit-cell edge direction normal to the plane of the crystal. In this case 'RF3' is a wise choice.

3. Potential orientations found by 'RefineOrient', 'RF2', or 'RF3' are stored in a list of rotation matrices, sorted according to their quality of fit. You can inspect all these orientations and check how well they match the diffraction pattern by selecting their sequence number in the 'Rotation Matrix' spin-box (6 in figure 5B). Most of the time, the orientation at the top of the list fits best. One way of picking the best indexing solution is:

- Clicking 'ShowMosaic' to show the indexed mosaic pattern (all the model reciprocal lattice spots that are close to the Ewald sphere);
- then go through all the possible orientations in the 'Rotation Matrix' spin box (starting from the most likely fitting sequence number zero) to find the best fit.

For certain unit cells in certain orientations, it may be that more than one orientations /

indexing solution fits well. This depends on the unit cell parameters and unfortunate combinations can exist in which it is not possible to distinguish on the basis of the positions of the diffraction spots alone. In this case you would also need to include intensity information and 3D merging of the diffraction data. This is beyond the current scope of EDiff. In these (rare) cases, you have to judge for yourself which is the most reasonable indexing.

6.9 Conclusion

The program EDiff will allow you to determine the unit cell of a crystal type, even if you can only collect single shots from randomly oriented crystals. It will index the diffraction images and allows considerable user interaction in determining, verifying and assessing the results. This is required as every crystal may have its own peculiarities and only by understanding the way in which the program its results can you truly appreciate the relevance of the suggested solution. Next steps include integration of the data (determining the intensities of the diffraction spots) and phasing. These are currently beyond the capacities of EDiff, and I am working towards these additional options.

Chapter 7 Conclusions and Perspectives

The research described in this thesis includes new methods for 3DEM single particle reconstruction: new software modules for particle picking and a more efficient CTF correction method. These new methods were used to solve an important biological question: how does the recovery system of heat-shock disrupted 50S ribosomal complexes work? Preliminary research on electron diffraction of nano-crystals allowed unit cell determination and resulted in the EDiff software suite.

Combined with image processing techniques, electron microscopy is powerful enough to investigate the atomic structure of bio-molecules. The potential of electron diffraction is still developing. 3DEM will allow investigations at near-atomic resolution and can become as powerful as the X-ray diffraction method in the foreseeable future. The method of 3DEM still has scope for further research and improvement. For instance for speeding up the Multi-Reference-Alignment process, which is the most time consuming step in the reconstruction. Software packages for iterative refinement and pushing the 3D models to atomic resolution are still in continuous development.

For electron diffraction of 3D protein nano-crystals, lots of work is still needed to determine atomic structures, such as intensity integration, recovering the phase and refinement. The work described in this thesis is only the first step in a series of many that may lead up to a general method for solving structures with diffraction data of 3D protein nano-crystals.

In X-ray crystallography, scientists invest major efforts into growing protein crystals, which in many cases do not grow beyond a size of several micrometers. Solving structures using such protein crystals requires the most advance and expensive third generation synchrotron beam lines. However electron crystallography can deal with even smaller crystals of nanometer size, which are beyond the reach for X-rays, but ideal for electron diffraction.

Electron crystallography has already been successful for a number of complicated inorganic compounds in material science. Organic and protein crystals are now also being studied by several research groups. There is no theoretical obstacle to solving atomic structures by using electron diffraction. But technical problems do exist, for example, protein crystals suffer from the serious and limiting factor of radiation damage. If these practical problems can be solved, electron diffraction on protein nano-crystals can be of immense importance in the foreseeable future and cryo-EM will be as important as synchrotrons for protein crystallography!

Summary

With the help of modern techniques of imaging processing and computing, image data obtained by electron cryo-microscopy of biomolecules can be reconstructed to three-dimensional biological models at sub-nanometer resolution. These models allow answering urgent problems in life science, for instance, the pathways directing the self-recovery system of cell, which certainly has great significance for all our lives. To determine these models, there are two main electron microscopic methods available, corresponding to its two main modes of operation: 3DEM single particle reconstruction and electron diffraction.

This thesis focuses on the research and methods of 3DEM (chapter 2 and 3) and electron diffraction, and its practical application in solving the structure of a 50S ribosomal complex, which clarifies the mechanism of cell recovery in heat shock stress (chapter 4). Preliminary research on a novel structure determination method by using nano-crystals resulted in a novel software suite – EDiff – which is a program for unit cell parameter determination and indexing (chapter 5 and 6).

The first chapter of this thesis introduces the background of some methods in structural biology, specifically emphasizing the relationship between 3D structures, electron microscopy and image processing techniques, comparing different atomic structure determination methods and summarizing the basics of 3DEM single particle reconstruction and electron crystallography.

In Chapter 2, new methods for automated particle picking and their software implementation are presented. Two new algorithms, automated carbon masking and quaternion based rotation space sampling, were designed and implemented. The algorithm of automated carbon masking can boost the particle selection process by automatically masking the carbon regions in micrographs. These regions should in general not be used for 3D structure determination, as the particles may be distorted by interactions with the carbon and also the carbon will increase the background signal. The algorithm of quaternion based rotation space sampling provides a common software library for sampling rotation space evenly. Currently, it is used in generating a

list of evenly distributed projections from a starting 3D model for the model-based particle picking method.

Chapter 3 presents a novel approximation method that corrects the amplitude modulation introduced by the contrast transfer function (CTF) by convoluting the images with a piecewise continuous function. As the resolution of 3DEM single particle analysis is being pushed down into sub-nanometer range, any new method that can increase the resolution of existing methods towards the atomic level is timely and important. Aberration correction of the CTF is important and different correction methods affect the resolution of the final model. The newly implemented method yielded higher resolution models with data sets from both highly symmetric (GroEL) and asymmetric structures (50S ribosomal complex). The tests also proved to be an efficient correction method that allowed quick convergence of the 3D reconstruction and had a high tolerance for noisy images.

In Chapter 4, with the single particle analysis of stalled 50S ribosome structures, I discovered the mechanism of how the heat shock protein (Hsp15) recovers the aborted ribosomal elongation cycle under cellular stress. When thermal stress dissociates the 50S and 30S particles of translating ribosomes, a 50S particle with a tRNA carrying a nascent chain can result. Because the nascent chain is threaded through the 50S particle, the tRNA does not readily dissociate, and hence the 50S particle is rendered useless. However, upon binding of the Hsp15 to such stalled 50S particles, the tRNA is translocated from A-site to P-site, and stabilized in a discrete conformation. The A-site is then freed up for a release factor to dissociate the tRNA, and the 50S subunit regains its translational activity. We determined the structure of the complex of the 50S ribosome, carrying Hsp15 and a nascent-chain tRNA to a resolution of 1.0 nm. This resolution approaches the highest resolutions obtained so far for asymmetric 3DEM single particle reconstruction.

Chapter 5 presents a novel algorithm for 3D unit-cell determination using randomly oriented electron diffraction patterns. Unit-cell determination is important because it is the first step towards the structure solution of an unknown crystal form. Most of the current unit-cell determination methods use tilt series, in which the angular relationship between the diffraction patterns is known. Our method uses single diffraction patterns

from multiple crystals, each with unknown orientation. The significance of our method is that for beam sensitive protein nano-crystals, more exposures in the same place burns the crystals. Thus single diffraction patterns from multiple crystals are the only data that we can get. The new algorithm searches the best matching unit cell parameters through checking all possible combinations of parameters. To accomplish the search task, two data sets are utilized. One data set contains the observed electron diffraction patterns; the other data set contains the simulated electron diffraction patterns from all potential unit cell models. A target function evaluates the similarity between these two data sets. The model with the smallest error is selected.

Chapter 6 gives a detailed tutorial of the EDiff software, which implements the new algorithms described in Chapter 5. This chapter is not only limited to teaching the use of EDiff, but also discusses new problems and solutions in unit cell determination. For instance, there is an assumption in our new algorithm that the diffraction data are "randomly" oriented. However, in real life, some types of crystals have an orientational preference (for instance because they are flat) limiting the relative orientation of incident beam to a conical region. This means that the collected data is not really randomly oriented. These data suffer from a missing cone problem similar to that in EM tomography. One parameter of the unit-cell may then be missed. An improved method which uses brightest spots in searching solves this "missing cone" problem.

Samenvatting

Titel: Beeldbewerking en Gegevensverwerking in relatie tot Structurele Biologie

Met behulp van moderne technieken van beeldbewerking en het verwerken van experimentele gegevens kunnen beelden, verkregen met cryo-EM, van bio-macromoleculen gereconstrueerd worden tot driedimensionale modellen van sub-nanometer resolutie. De twee belangrijkste methoden die nu in gebruik zijn, zijn "3DEM single particle reconstruction" en elektronendiffractie.

Dit proefschrift is gericht op onderzoek naar betere methoden van 3DEM (hoofdstukken 2-4) zowel als elektronendiffractie. (hoofstukken 5 & 6). In hoofdstuk 2 worden twee nieuwe algoritmen gepresenteerd: geautomatiseerde "carbon masking" en "rotational space sampling" gebaseerd op het gebruik van quaternionen.

Gebruik van deze methodieken bevordert het proces van deeltjes selectie door het automatisch maskeren van koolstof gebieden in de foto zowel als meer nauwkeurige plaatsbepaling bij gebruik van een beginmodel.

In hoofdstuk 3 wordt een nieuwe methode van benadering gepresenteerd waarmee de amplitude modulatie, die het gevolg is van de "contrast transfer functie" (CTF) van het gebruikte microscoop, gemodelleerd kan worden. Hierdoor kan de resolutie die verkregen kan worden met 3DEM worden verbeterd, tot in het subnanometer gebied. De nieuwe benadering bevordert tevens een spoedige convergentie van het iteratieve reconstructieproces, waarbij een hoge tolerantie voor beelden met veel ruis opvalt.

Een praktische toepassing, het bepalen van de structuur van een 50S ribosomaal complex wordt beschreven in hoofdstuk 4. De verkregen resultaten zijn verhelderend voor het begrip van het herstelmechanisme van cellen die te lijden hebben gehad van hitte shock. Wanneer ten gevolge van hitte shock dissociatie optreedt van de 50S en 30S deeltjes van transcriptieribosomen is het mogelijk dat een 50S deeltje ontstaat met een gedeeltelijk getranscribeerd tRNA. Wanneer Hsp15 bindt aan zo'n "stalled" 50S deeltje verhuist het tRNA van de A-site naar de P-site, en is daar stabiel in een gegeven conformatie. De A-site is dan vrij voor een "release factor" waardoor het tRNA kan

dissociëren en het 50S deeltje zijn activiteit herwint.

Verkennend onderzoek naar een structuurbepalingsmethode, gebaseerd op diffractie aan nano-kristallen, heeft een software pakket Ediff opgeleverd (hoofdstukken 5 en 6). Het programma is gericht op het bepalen van de eenheidscel parameters en de indexering van verkregen diffractogrammen. De methode maakt gebruik van losse diffractogrammen verkregen van meerdere kristallen, elk met een eigen, onbekende, oriëntatie.

Het belang van de methode is dat voor stralingsgevoelige nano-kristallen van bio-materialen, losse diffractogrammen van meerdere kristallen de enige diffractiegegevens zijn die verkregen kunnen worden. Meer dan één blootstelling op dezelfde plaats in het preparaat leidt tot overmatige kristal beschadiging.

Curriculum Vitae

Linhua Jiang was born on November 12, 1977 in Yongzhou, China. In 1995, he finished his studies in secondary school and started Computer Science education in Shanghai Jiaotong University, China. He also studied Economics as a minor subject at Jiaotong University. In 1999, he obtained a bachelor degree in Computer Science and a second bachelor degree in Economics.

After years of work experience as network engineer and software engineer, he decided to extend his expertise by studying abroad in an advanced master program of Artificial Intelligence at the Katholieke Universiteit Leuven in Belgium, 2003. In 2003 and 2004, the internship in the Multimedia Lab in IMEC (Interuniversity MicroElectronics Center), Belgium, fostered his interests in scientific research.

Shortly after he received a master degree *cum laude*, he joined the Cyttron research project as a Ph.D candidate in the department of Biophysical Structural Chemistry, Leiden University. He devoted himself to the research of new methods and their applications in solving the structures of macromolecules, which resulted in this thesis.

A Special Word of Thanks

To end my thesis, I would like to express my sincere gratitude to all the people who helped me and supported me during the last four years.

First, I would like to thank Prof. Dr. Jan Pieter Abrahams for his guidance, support and encouragement during my research period. I found great enlightenment from his remarks. Lots of original ideas resulted from the fruitful discussions with him. With his support, I had so many opportunities of advanced traineeship, e.g. in Houston USA, Madrid Spain and Antwerpen Belgium.

I would also like to thank my supervisor, Dr. Jasper R. Plaisier for his great help in starting my research of single particle reconstruction. I really appreciate the happy time that we work together and our journey to the USA for an international conference near Lake Tahoe.

Many thanks to my collaborators who helped me and contributed in the project of ribosomal reconstruction: Prof. Dr. Nenad Ban, Dr. Christiane Schaffitzel, Dr. Roman I. Koning, Dr. Rouven Bingel-Erlenmeyer, Dr. Philipp Korber, Daniël C. de Geus. And also in the project of electron crystallography: Prof. Dr. Henny W. Zandbergen, Dr. Stavros Nikolopoulus and Dr. Dilyana Georgieva. I am really impressed by Dilyana for working so hard and spending so much time in collecting perfect electron diffraction data and help me testing the EDiff software. We successfully collaborated in determining the unit cell of several types of nano-crystals. I also acknowledge the contributions of the master students Maurits W. A. Kok and K.I.M. IJspeert in this project.

I am very grateful for the help from other teachers and colleagues: Dr. RAG de Graaf, Dr. Maxim Kuil, Dr. Navraj S. Pannu, Prof. Dr. Mathieu Noteborn, Dr. Irakli Sikharulidze, Dr. Pavol Skubak, Dr. Zunfeng Liu, Dr. Pavol Skubak, Dr. Ellen Thomassen, Jan de Sonneville, Francoise Grenouilleau, and others. Particularly thanks to Dr. RAG de Graaf for translating the summary to Dutch (Samenvatting).

Special thanks to my wife, Hua Pan. She abandoned a nice job and easy life in Shanghai to accompany me. She always understands me and supports me, and has even helped me with producing drawings and documentation for my thesis. Without her, I would not have such a lovely son, Hauer Jiang, who was born in May 2008. She works so hard and is such a good, unselfish mother in our small home.

Last but not the least, I would like to acknowledge my families in China: my parents, parents-in-law, brother and sisters. Though they are far away, they always contact me and give me encouragement and confidence.

To those whom I forgot to mention, I apologize.